Petrographic, geochemical and geochronological characterisation of Batavia Knoll Dredge samples, Perth Abyssal Plain: implications for linkage with Gondwana

Madeline Elsa Kobler

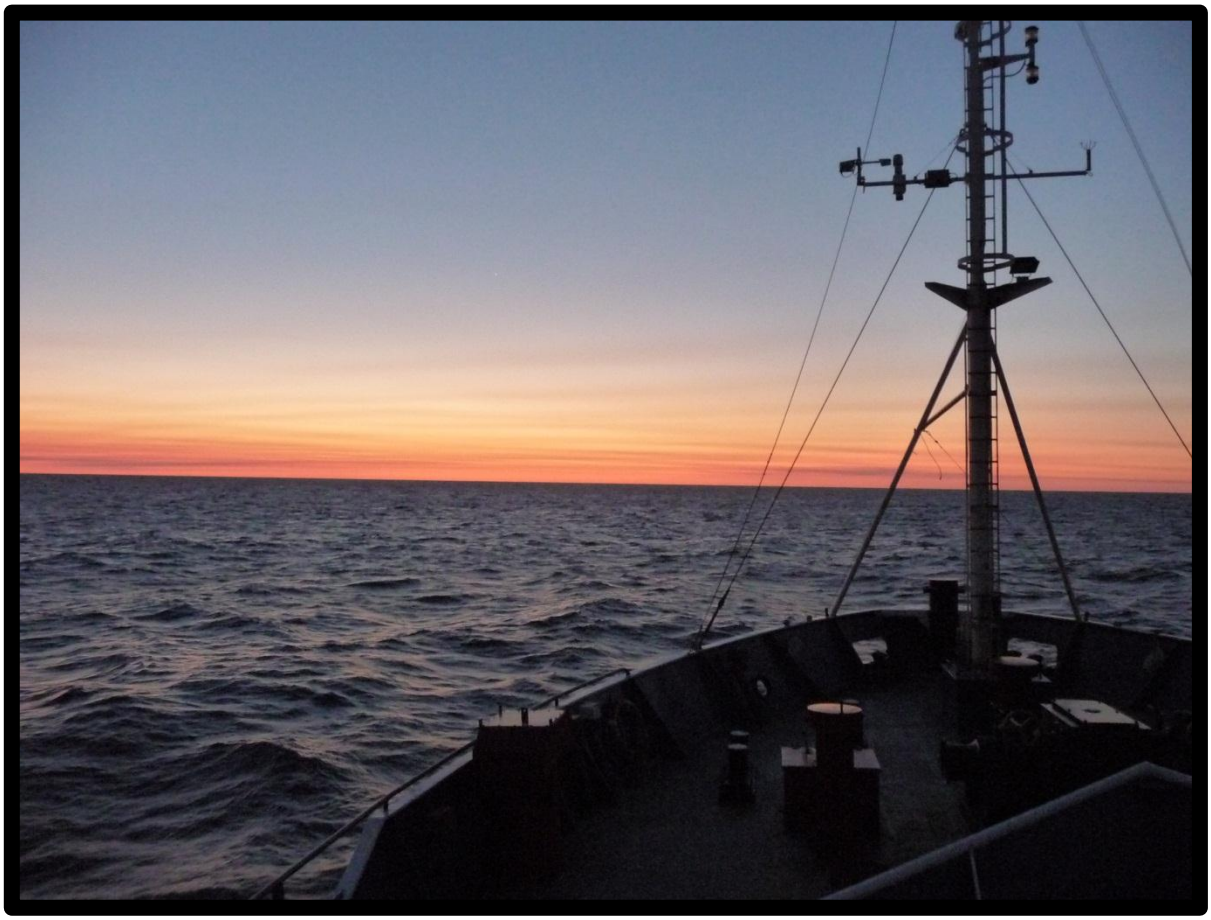

Presented to the Department of Earth and Planetary Sciences,
Faculty of Science
in Partial Fulfillment of the Requirements
for the Degree of

Honours, BSc
Macquarie University, Sydney
June, 2012

MACQUARIE UNIVERSITY

CCFS

STATEMENT OF ORIGINALITY

All the work submitted in this thesis is the original work of the author except where otherwise acknowledged. No part of this thesis has previously been submitted to any other university or institution.

_____ _____

Signed – *Madeline Elsa Kobler* ***Dated***

Acknowledgements

Writing these acknowledgements has made me realise how many people have made this last year enjoyable and possible. Thank you to each and every one of you!

I would firstly like to thank my supervisor Nathan Daczko for his endless patience, the ease with which he shared his vast knowledge and willingness to help at any and every stage. Most importantly I would like to thank him for showing incredible enthusiasm for my topic when it seemed no one else did. I would also like to thank him for attending field work, despite his ailments. Your time and chocolate over this last year is much appreciated.

Another big thank you to Robyn Gardner for her invaluable friendship over this last year. Spending 24/7 for 3 weeks on a boat together was great – and still being friends now is even better. Your help, continual motivation and coffee dates this last year is greatly appreciated.

To the many academics and lab staff who have given me guidance on the use of the machines, sharing an endless and priceless supply of knowledge and your continual willingness and ability to help with my many problems. Dick Flood, Norm Pearson, Elena Belousova, Kevin Grant, Will Powell, Steve Craven, Simon Turner, Rosanna Murphy, Peter Wieland, Rod Lawrence, Manal Bebbington and Nigel Wilson – thank you. Your help was both insightful and invaluable.

Thank you to everyone on the Southern Surveyor cruise (Jacqui Halpin, Tara Martin, Simon Williams and all the boys). Without all of you, three weeks would not have been quite so bearable or enjoyable.

A special thanks to all my non-geology friends for understanding my lack of presence over the last few months. To Thomas for being my rock, understanding my inability to think, eating endless amounts of "study" chocolate with me and for being my stress ball. Thank you for always being there. To Laura for taking me shopping and drinking copious amounts of tea with me. And to everyone else – thank you!

My geology friends. Ceinwen and Jaclyn – thank you for forcing me to study geology, for the Hello Pandas, sushi, dumplings, tea, baking and for being such great friends. To James, Rusty, Vicki and everyone else in the demountable, thank you for making this last year semi-sane. Sorry for my loud typing.

A special thanks to my family. Mum and Dad, your endless patience, continual support, questioning, help and attempts (and succeeding) to understand my work has been invaluable. To my brother for climbing a volcano and picking blueberries with me. To my Grandmama for proofreading, and to my Nana for support. Without all of your love this would have been incredibly hard.

To everyone mentioned here and those who were not mentioned – thank you!

Abstract

This study heralds the discovery of a submarine micro-continent called Batavia Knoll, confirming its previously unknown continental crust affinity. The Knoll is submerged under approximately 2km of water on the Perth Abyssal Plain, some 1600km west of the Western Australian coast. Detailed petrographic, geochemical and geochronological analysis of seven representative dredge samples from Batavia Knoll has enabled the characterisation of these rocks, and thus of the Knoll. It is comprised predominantly of granites, granite gneisses, intermediate gneisses, schists and sandstones. The majority of the analysed granitoids (n=6) record emplacement and orogenesis from the latest Neo-Proterozoic to Cambrian. These rocks subsequently enjoyed tectonothermal activity soon after emplacement, marked by zircon disturbance and metamorphic/deformation textures. Older basement rocks were not sampled, unless the zircon poor intermediate gneisses are significantly older than the granitoids. The dredged sandstone rocks were not examined in this study, but likely represent rift-related sedimentation during Gondwana dispersal at ca. 132 Ma. These sandstones will be examined at the University of Sydney. The presence of orogenic activity associated with Gondwana amalgamation between 600-500 Ma combined with current plate tectonic reconstructions allows for the correlation of Batavia Knoll with the Kuunga Orogeny.

Table of Contents

Chapter 6 – Mineral chemistry by electron microprobe

Digital Appendix :

List of Figures

List of Tables

Abbreviations

Ab	Albite
Alm	Almandine
An	Anorthite
ASI	Aluminium saturation index
BDL	Below Detection Limits
Bt	Biotite
Ca.	Circa
CHUR	Chondritic Unfractionated Reservoir
CL	Cathodoluminescence
Cpx	Clinopyroxene
CSIRO	Commonwealth Scientific and Industrial Research Organisation
disc.	Discordant
DM	Depleted Mantle
EMP	Electron microprobe
GAU	Geochemical Analysis Unit
GEMOC	Geochemical Evolution and Metallogeny of Continents
GLITTER	GEMOC Laser ICPMS Total Trace Element Reduction
Grs	Grossular
Grt	Garnet
Kfs	K-feldspar
LA-ICP-MS	Laser ablation microprobe-inductively coupled plasma mass spectrometry
LLD	Lower Limits of Detection
LOI	Loss on Ignition
MSWD	Mean Square Weighted Deviation
Myrm	Myrmekite
Opx	Orthopyroxene
Or	Orthoclase
ORG	Ocean Ridge Granite
Plag	Plagioclase
PPL	Plain Ploarised Light
Prp	Pyrope
Qtz	Quartz
rsd	Relative Standard Deviation
SEM	Scanning Electron Microscope
Sps	Spessartine
syn-COLG	Syn-collisional Granite
TAS	Total alkali vs. silica
THf DM	Hf Depleted Mantle Model Age
THf DMc	Crustal Hf Depleted Mantle Model Age
VAG	Volcanic Arc Granite
WPG	Within Plate Granite
XPL	Cross Polarised Light
XRF	X-ray fluorescence

Chapter 1 - Introduction and Regional Geology

1.1 Background and significance – the big picture

The final amalgamation of the southern supercontinent Gondwana occurred in the Ediacaran – Cambrian, involving the collision of India with the already combined Australia/Mawson block, and the collision of the Congo and Kalahari cratons (Fig. 1.1) (Collins & Pisarevsky, 2005). This collision is marked by a large orogenic zone: the Kuunga Orogeny (Fig. 1.2) (Meert *et al.,* 1995). This study uses the term 'Kuunga Orogeny' to define orogenesis related to the collision of the Australia/Mawson block with India, occurring between ca. 600-500 Ma (Collins & Pisarevsky, 2005). As such, the well exposed section of the orogeny marked by the collision of Congo and Kalahari cratons is not examined in detail here. Presently, the rocks affected by the Kuunga Orogeny (marked by the collision of Australia/Mawson block and India) are poorly exposed due to rock of this age being i) buried under the Mesozoic sedimentary rocks of the Perth Basin, Western Australia, ii) buried under ice in Antarctica, iii) covered by water in the Indian Ocean and iv) destroyed due to subduction of greater India due to the India-Asia collision. As such, geological understanding of the Kuunga Orogeny is restricted to studies from inliers on Western Australia (Northampton and Leeuwin complexes, Janssen *et al.,* 2003), thinned pieces of submerged continental crust (Naturaliste and Kerguelen Plateau, Halpin *et al.,* 2011; Nicolaysen *et al*., 2002; Weis *et al.,* 2001) and scarce exposures of rock on the east Antarctic coast (Denman Glacier and Prydz Bay, Boger *et al.,* 2008; Veevers, 2012).

Cretaceous rifting of Gondwana at ca. 132 Ma saw the separation of India from Australia and the formation of the Indian Ocean (Ingle *et al.,* 2002; Veevers, 2006). Complex continental rifting, seafloor spreading and plume related processes caused the fragmentation of thinned continental crust such as the Naturaliste, Wallaby and Zenith Plateaus off the coast of Western Australia (Fig. 1.3), and the Kergulen Plateau off the coast of east Antarctica (Halpin *et al.,* 2011; Nicolaysen *et al.,* 2002).

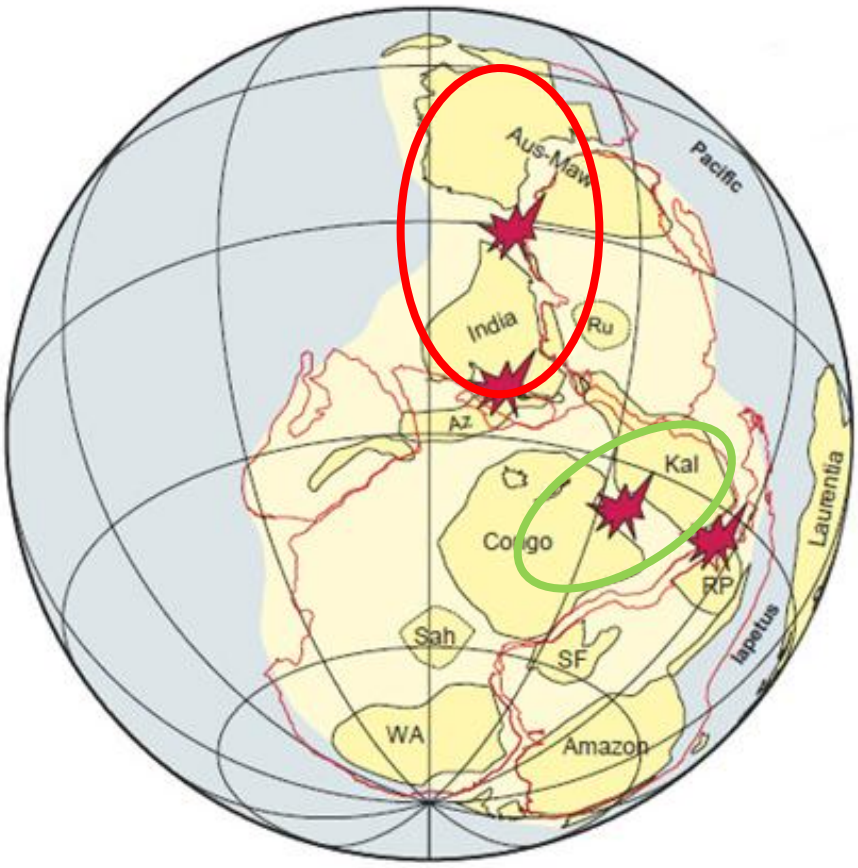

Fig. 1.1. Final Gondwana amalgamation at ca. 530 Ma: collision of Australia/Mawson craton with India (red oval), and the collision of Congo and Kalahari cratons (green oval). Red zones indicate areas of collision. Adapted from Collins & Pisarevsky, 2005, Fig, 6, pp.236. Amazon = Amazonia; Aus-Maw = Australia/Mawson Block; Az = Azania; Congo = Congo /Tanzania /Bangweulu Block; Kal = Kalahari Block; RP = Rio de la Plata; SF = Saˆo Francisco; WA = West Africa. Adola, Adamastor, Braziliano, Mozambique, Pacific = oceanic basins. Ru = Ruker Terrane.

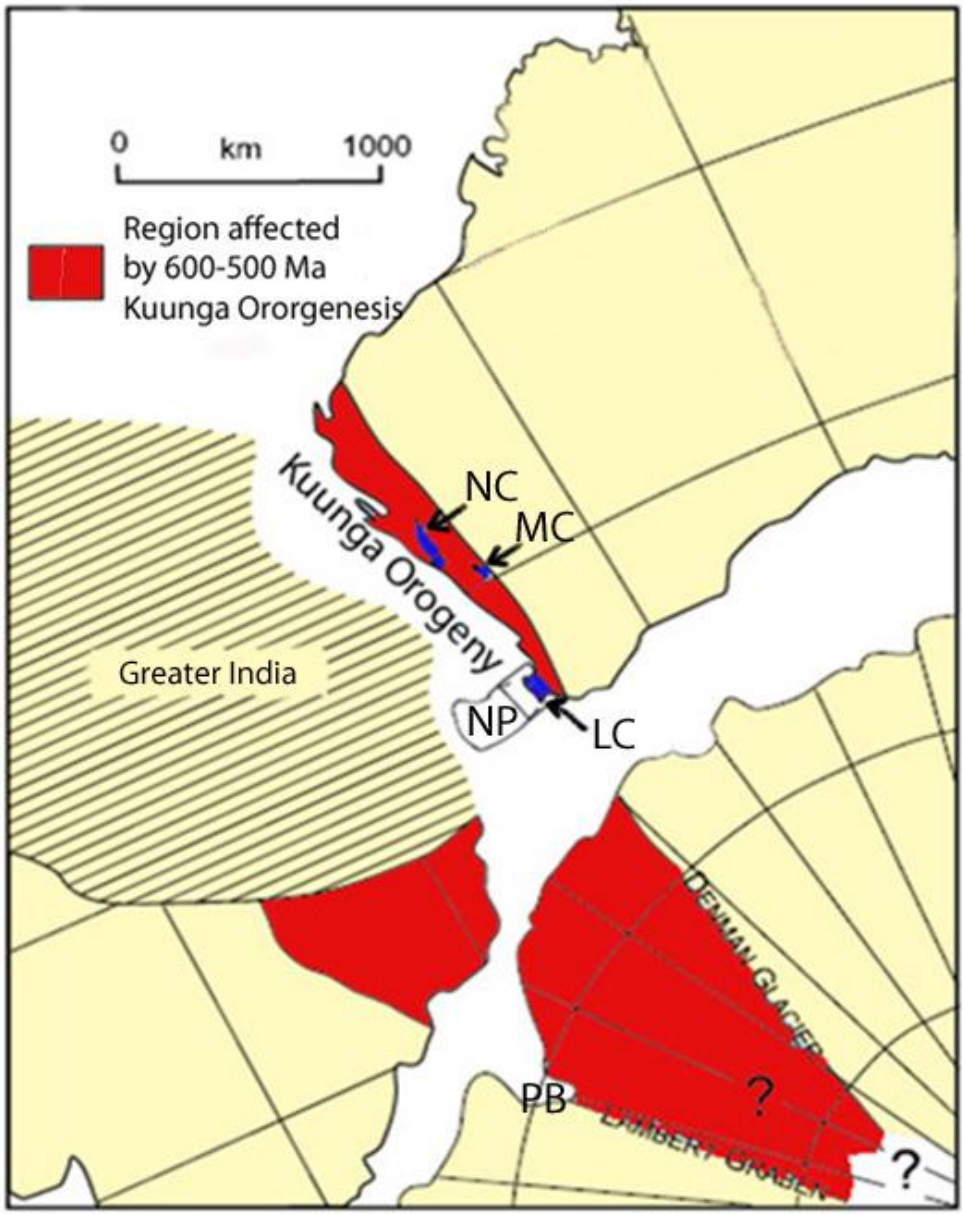

Fig. 1.2. Location of the Kuunga Orogeny in Gondwana at ca. 500 Ma (red zone). Adapted from Collins, 2003, Fig 1a, p.586. MC = Mullingarra Complex. NC = Northampton Complex. NP = Naturaliste Plateau. PB = Prydz Bay.

Two bathymetric highs, Batavia Knoll and Gulden Draak Knoll appear much like the micro-continents describe above. They are situated in the Indian Ocean, approximately 2km under sea level and some 1600km from the Western Australia coast (Fig. 1.3). The 2011 Southern Surveyor cruise SS2011_v06 confirmed a previously unknown crustal affinity of Batavia Knoll and Gulden Draak Knoll, heralding the discovery of two new submarine micro-continents. Current plate tectonic reconstructions of Gondwana place Batavia Knoll and Gulden Draak nestled just north and just south of the Naturaliste Plateau respectively (Fig. 1.4) (Gibbons *et al.*, 2006). This is consistent

with a continental crust affinity that places them within the Kuunga Orogeny (Meert *et al.,* 1995). The focus of this study is the submarine micro-continent Batavia Knoll, an important and rare piece in the Kuunga Orogeny puzzle.

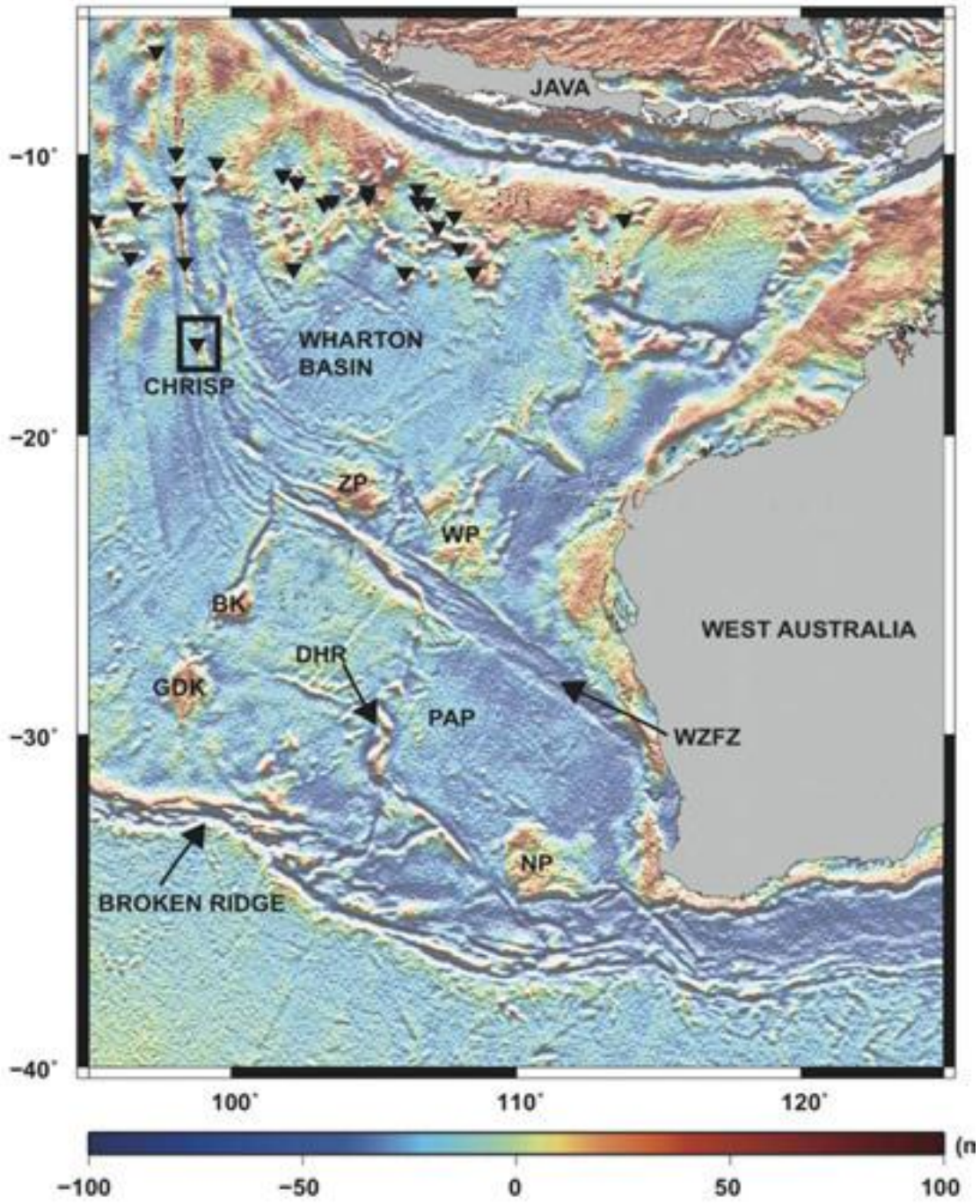

Fig. 1.3. Current location of Batavia Knoll, Gulden Draak and the Wallaby, Zenith and Naturaliste Plateaus. Adapted from Gibbons *et al.*, 2006, Fig 1a, p54. BK= Batavia Knoll. ZP = Zenith Plateau. WP = Wallaby Plateau. NP = Naturaliste Plateau. GDK = Gulden Draak. DHR = Dirck Hartog Ridge. PAP = Perth Abyssal Plain. WZFZ = Wallaby-Zenith Fault Zone.

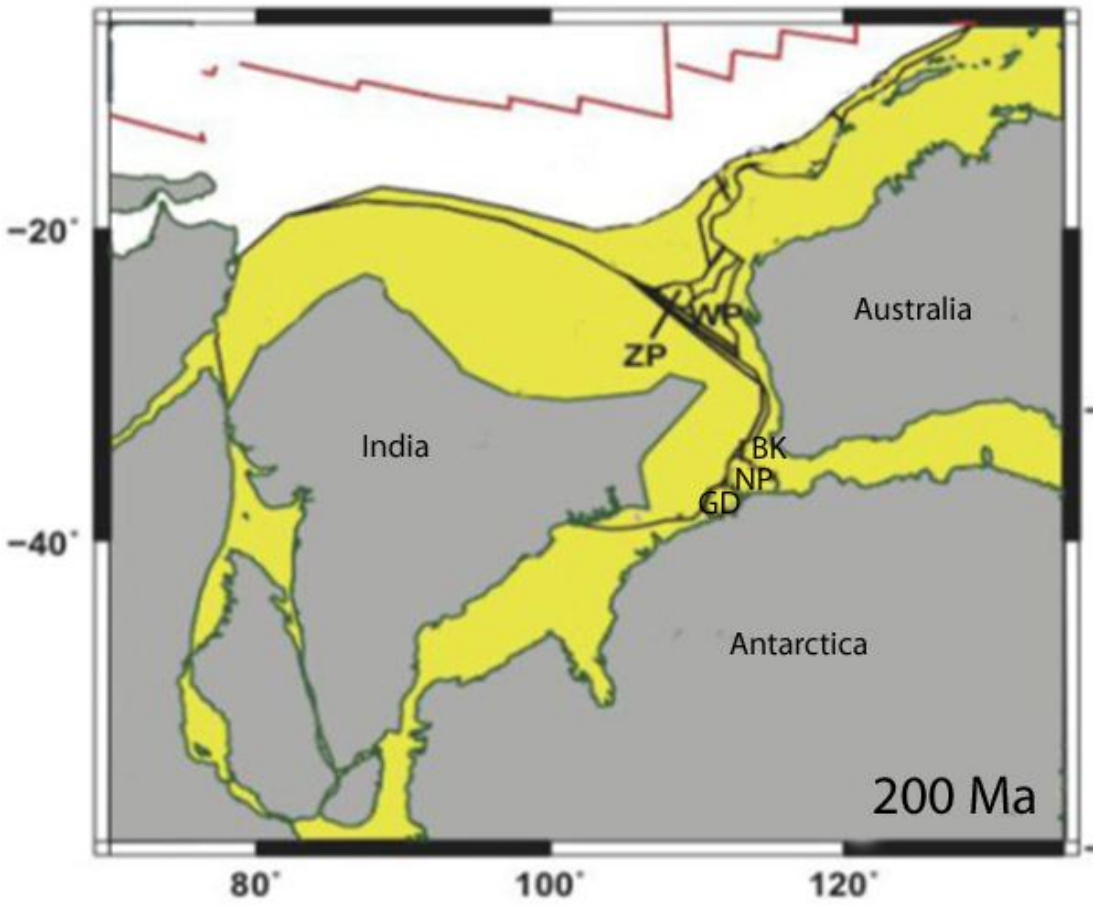

Fig. 1.4. Location of Batavia Knoll and Gulden Draak at ca. 200 Ma. Adapted from Gibbons *et al.*, 2006, Fig. 6, p.68. BK = Batavia Knoll. NP = Naturaliste Plateau. GD = Gulden Draak. WP = Wallaby Plateau. ZP = Zenith Plateau.

1.2 Regional geology of the Kuunga Orogeny

This study presents Batavia Knoll granitoids that have continental crust affinity and have recorded tectonothermal activity from ca. 600-500 Ma, consistent with the Kuunga Orogeny. As such, the following section of this chapter will characterise the igneous and metamorphic ages of crust deformed in the orogenic zone, as well as the significant tectonothermal events of the Kuunga Orogeny. Table 1.1 summarises geochronological data collected from rocks affected by the Kuunga Orogeny in Western Australia, Antarctica and offshore. Fig. 1.5 summarises all analysed rock samples from the Kuunga Orogeny zone in Africa (marked by the collision of the Kalahari and Congo cratons) (Meert, 2003).

Area	Rock type / metamorphic event	Age (Ma)
Leeuwin complex, Western Australia	Granulite facies metamorphism	522
	Aergirine-augite syenite gneiss	523 ±35
	Hbl-Bt granite gneiss	524±12
	Monzogranite	524
	Unfoliated granitic dykes	525
	Aergirine-augite syenite gneiss	535 ±9
	A-type granite	540
	Massive granite Gneiss	540 ±6
Northampton complex, Western Australia	Amphibolite facies shear zone	550
Naturaliste Plateau, Offshore Western Austrailia	Metamorphism	515±5
Bunger Hills, Antarctica	Mafic Dykes	500
Denman Glacier / Mirny, Antarctica	Granulite facies metamorphism	503
	Charnokite intrusion	504
	Syenite	516
Prydz Bay, Antarctica	Alkali Syenite	482±3
	A-type granite	500 ± 4
	Granite	524-501
	Pegmatite	524-501
	Basanite	504
	Leucogneiss	508±11
	Peak metamorphism	508±11
	Granite	514, 516
	A-type granite	524, 565
	Turk orthogneiss	530±4
	Granulite facies metamorphism	530
	Syenogranite	550
	Philpot orthogneiss metamoprhism	553±21
	Ultra high tectono-metamorphism	570-520
	Granulite facies metamorphism	570-510

Table 1.1. Rock type, ages and metamorphic events recorded in the Kuunga Orogeny in Western Australia, Antarctica and offshore from 400-600 Ma (Boger, 2008; Cawood & Korsch, 2003; Janssen *et al.*, 2003; Veevers & Saeed, 2011; Veevers, 2012).

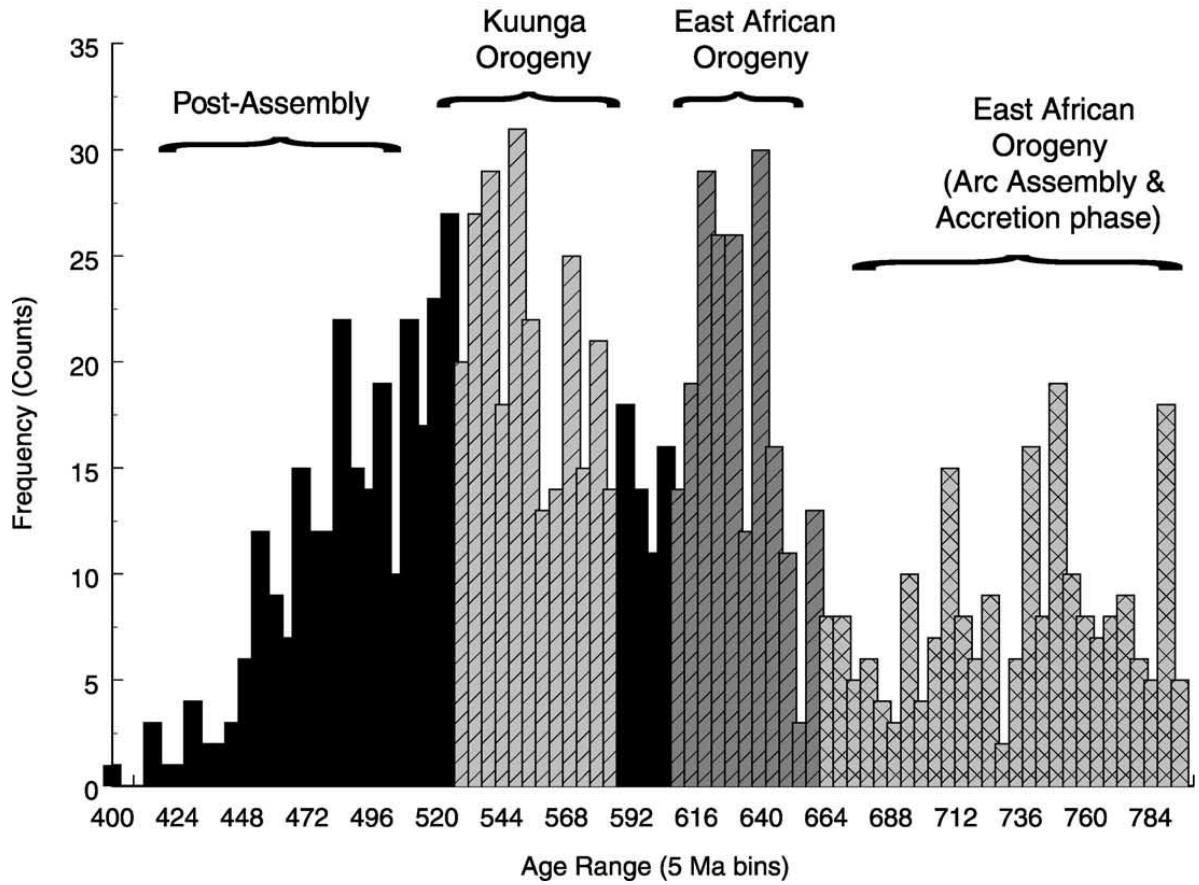

Fig. 1.5. Histogram displaying ages for every recorded rock sample (n=1057) within the Kuunga Orogeny in Africa. Of note is the large peak signifying the Kuunga Orogeny (Meert, 2003, Fig.3, p.6).

Kuunga Orogeny in Western Australia: Leeuwin Complex

Three inliers expose basement to the Perth Basin; these are the Northampton, Mullingarra and Leeuwin complexes (Fig. 1.6) (Cawood & Korsch, 2008). The Mullingarra complex exposes Mesoproterozoic rocks and no evidence of Kuunga orogenesis has been documented. The Northampton Complex contains 550Ma shear zones, inferred to have formed during the Kuunga orogenesis. The Leeuwin Complex records three major magmatic pulses: 1200-1050 Ma, 800-650 Ma and 580-500 Ma; the last phase related to Kuunga orogenesis. Metamorphic grade in the complex varies from amphibolite facies in the south to granulite facies in the north (Cawood & Korsch, 2008). The oldest magmatic pulse emplaced ca. 1200 Ma granitoids that were metamorphosed to garnet augen gneiss and zircon grains experienced lead loss at ca. 1000 Ma (Janssen *et al.*, 2003). The second magmatic pulse emplaced intermediate composition plutons now hornblende gneiss, metamorphosed at ca. 630-600 Ma. The Kuunga-aged magmatic pulse emplaced

granitic rocks at ca. 540-535 Ma and 525 Ma, which are now deformed, indicating a minimum age of Kuunga orogenesis deformation in this area (Cawood & Korsch, 2008; Janssen *et al.*, 2003).

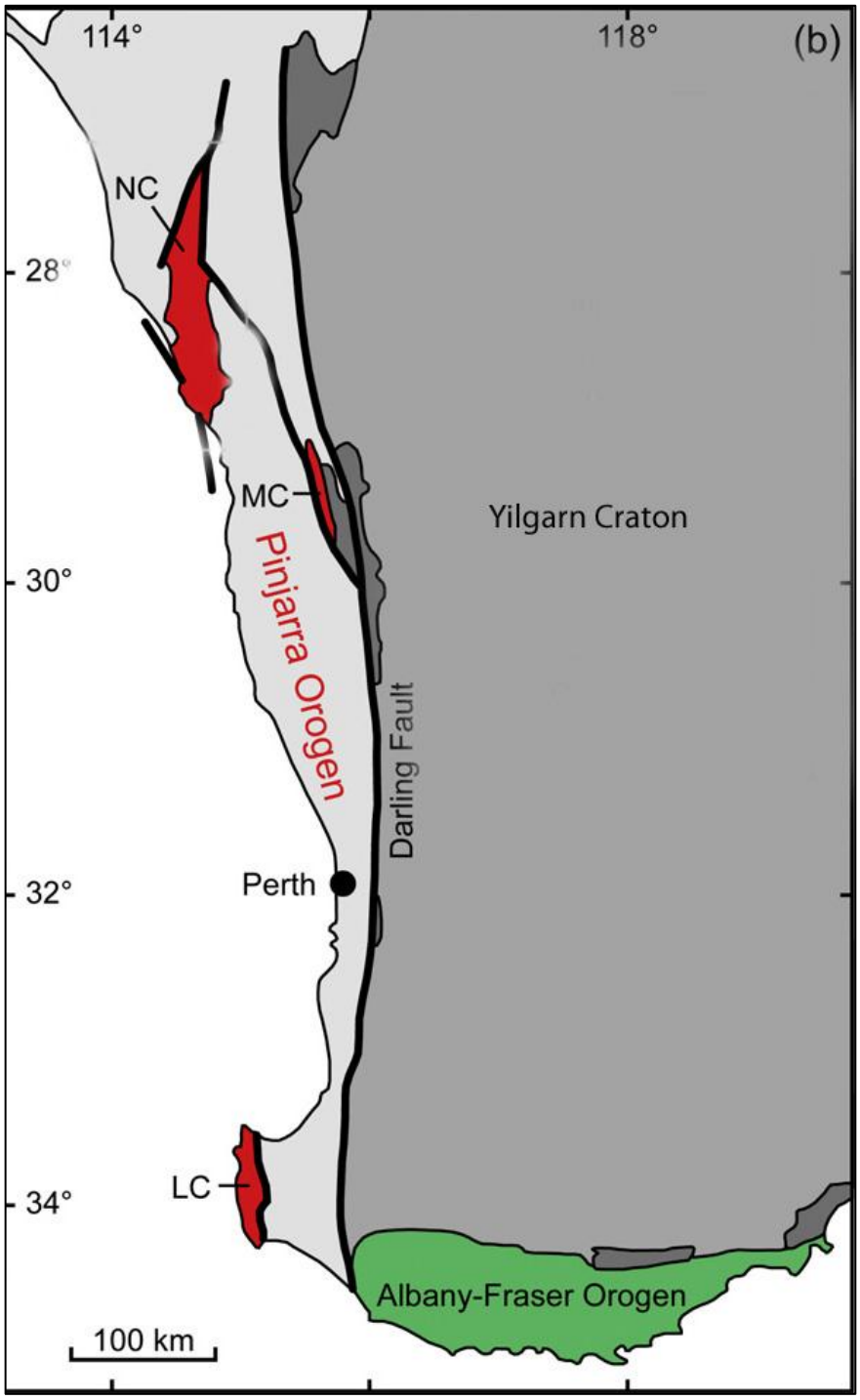

Fig. 1.6. Location of Leeuwin and Northampton complex in Western Australia. Adapted from Ksienzyk *et al.*, 2012, Fig. 1, p.38. NC = Northampton complex. MC = Mullingarra complex. LC = Leeuwin complex.

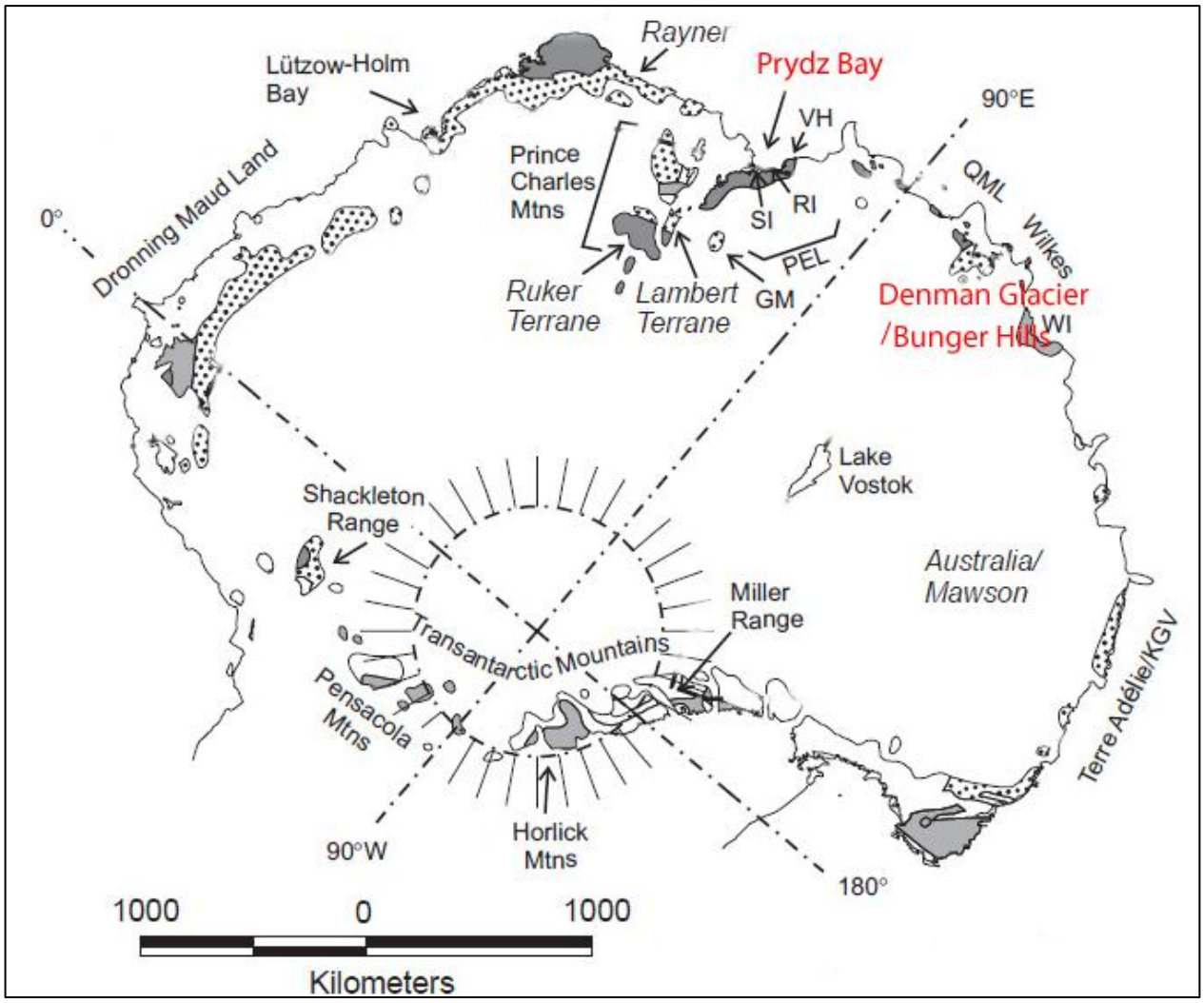

Fig. 1.7. Location of Prydz Bay, Denman Glacier and Bunger Hills in Antarctica. Adapted from Collins & Pisarevsky, 2005, Fig. 8, p.241. GM=Grove Mountains, KGV=King George V Land, PEL=Princess Elizabeth Land, QML=Queen Mary Land, RI= Rauer Islands and Terrane, SI=Sbstrene Island, I=Windmill Islands, Wilkes=Wilkes Land, VH=Vestfold Hills.

Kuunga Orogeny in Antarctica: Prydz Bay, Denman Glacier and Bunger Hills

Prydz Bay and Denman Glacier are located on the coast of eastern Antarctica (Fig. 1.7). Based on tectonic reconstructions of Gondwana and local geochronological data, Kuunga orogenesis extends from offshore Western Australia into Antarctica (Collins & Pisaversky, 2005).

The Prince Charles Mountains in Prydz Bay (Fig. 1.7) can be divided into three domains. The Ruker Province comprises entirely Archean rocks with depositional and intrusive ages ca. 3170 Ma and tectonic activity ca. 2780 Ma. It is separated from the younger Prydz Bay rock units by an unconformity (Boger *et al.*, 2008). The Lambert Province consists of two groups of

metasedimentary rocks with minimum detrital ages of 2500 Ma. Intrusions dated at 2423 Ma and 2065 Ma are present. This region was deformed and metamorphosed by several events in the time between 1310 and 795 Ma, with a major tectonothermal event occurring in the early Cambrian, causing peak metamorphism at 553 and 508 Ma with orthogneiss and leucogneiss protolith emplacement at 530 and 508 Ma respectively. The Fisher Province contains volcanic and plutonic rocks formed between 1300 and 1280 Ma (Boger, *et al.,* 2008).

The Larsemann Hills (Fig. 1.7) consist of the Brattstrand paragneiss (all meta-sedimentary units in the southern Prydz Bay region, deposited between 1100-1000 Ma) overlying the older SØstrene orthogneiss (most meta-igneous units in the area, intruded ca. 1100 Ma). Metamorphism occurred at ca. 1000 Ma, with more felsic and mafic igneous rocks intruded between 980-970 Ma. This was followed by metamorphism at ca. 530 Ma and emplacement of granite and pegmatite between 524 and 501 Ma (Grew *et al.,* 2012).

The Denman Glacier region, located to the west of Bunger Hills, (Fig. 1.7) comprises an igneous precursor orthogneiss dating to 3003 Ma and emplacement orthogneiss at 2641 Ma. A syenite body dated at 516 Ma is also present. Metamorphism occurred in this area at 2889, 1040 and 503 Ma with charnokite intrusions at 504 Ma (Veevers, 2012).

The Bunger Hills located next to Denman Glacier (Fig. 1.7) contains mafic dykes which were emplaced at 500 Ma (Veevers, 2012).

Kuunga Orogeny offshore Western Australia: the Naturaliste Plateau

The Naturaliste plateau is situated off the southwest tip of Australia (Fig. 1.3) (Halpin *et al.,* 2008). Basaltic rocks of 130- 120 Ma that are similar in age and geochemistry to the Bunbury basalts of the South Coast of Western Australia are present (Zhu, 2009). Mesoproterozoic felsic gneisses are also present, emplaced between 1230-1190 Ma and subsequently deformed in the Kuunga Orogeny at ca. 515 Ma (Halpin, *et al.,* 2008).

Kuunga Orogeny offshore Antarctica: Kerguelen Plateau

The Kerguelen Plateau sits approximately 1500km north of Prydz Bay (Ali & Karuse, 2001) and contains fragments of continental crust which include rock types and ages similar to those affected by the Kuunga Orogeny in Antarctica and Australia. Clasts of garnet-biotite gneiss with quartz, alkali feldspar, plagioclase, garnet, zircon, monazite, biotite and muscovite have been found within basaltic sequences at Elan Bank (on the west of the Plateau) (Nicolaysen *et al*., 2002). Zircon dates from the clasts and surrounding sandstone are 938.5±3.2, 836.1±2.1, 795.8±1 and 532.5 Ma, the youngest age being coeval with the Kuunga orogenesis.

1.3 Aims and approach of this study

Aims of this study:

1. To perform a petrographic, geochemical and geochronological characterisation of seven representative dredge samples from Batavia Knoll. Sixty-one rocks were dredged from this location and seven samples were chosen to be studied in detail due to their large sample size, unweathered appearance and overall appearance as the most representative of the dredge;

2. To characterise the petrographic, geochemical and geochronological relationships, or lack thereof, that exist between the seven individual Batavia Knoll rock samples to understand their relative histories;

3. To establish any geochronological relationships that exist between the Batavia Knoll rock samples of this study and rocks that have been affected by the Kuunga Orogeny.

Approach of this study:

The unconstrained spatial relationships of Batavia Knoll dredge samples due to their submergence under approximately 2km of water facilitates the reliance on petrographical, geochemical and geochronological analytical techniques to determine the characteristics of the rocks and their relationships with one another. As such, seven representative rock samples from Batavia Knoll have been chosen for petrographic analysis, whole rock bulk major and minor chemistry, mineral chemistry and zircon U-Pb and Lu-Hf isotope analysis. Such methodology is utilised to determine a greater insight into the processes that have formed and affected these rocks, and an understanding of their relationships with one another and with the Kuunga Orogeny can be attained.

Chapter 2 - Fieldwork

2.1 Introduction

Fieldwork was conducted for three weeks (20thOct 2011 - 9thNov 2011) off the coast of Western Australia on the Perth Abyssal Plain (Fig. 2.1). Research was undertaken aboard the CSIRO research vessel "*Southern Surveyor"* (cruise SS2011_v06) for the duration of the trip by myself, Simon Williams (chief scientist), Nathan Daczko, Jacqueline Halpin, Robyn Gardner and others cited in Appendix A. The ship followed transects shown in Fig. 2.1, measuring the magnetic pattern of the underlying seafloor with a magnetometer. Multibeam swath bathymetry was also measured for the duration of the voyage to map the bathymetry of the sea floor. Seven dredges were performed; two on Batavia Knoll, two on Gulden Draak Knoll and three on Dirck Hartog Ridge (Fig. 2.1). Due to minimal previous research on this expanse of seafloor and initial exciting findings, the itinerary was continuously adapted in accordance with the findings (Fig. 2.2).

2.2 Aims

Previous to this voyage, the area had not been examined. As such, there were two main aims for the voyage:

1. To obtain approximately 3000km of magnetic anomaly data: four profiles across the Perth Abyssal Plain trending NW-SE, and one across the "de Goneville triangle".
2. To carry out 6 dredges on Batavia Knoll, Gulden Draak Ridge, southern flank of the Naturaliste Fracture Zone and Dirck Hartog Ridge.

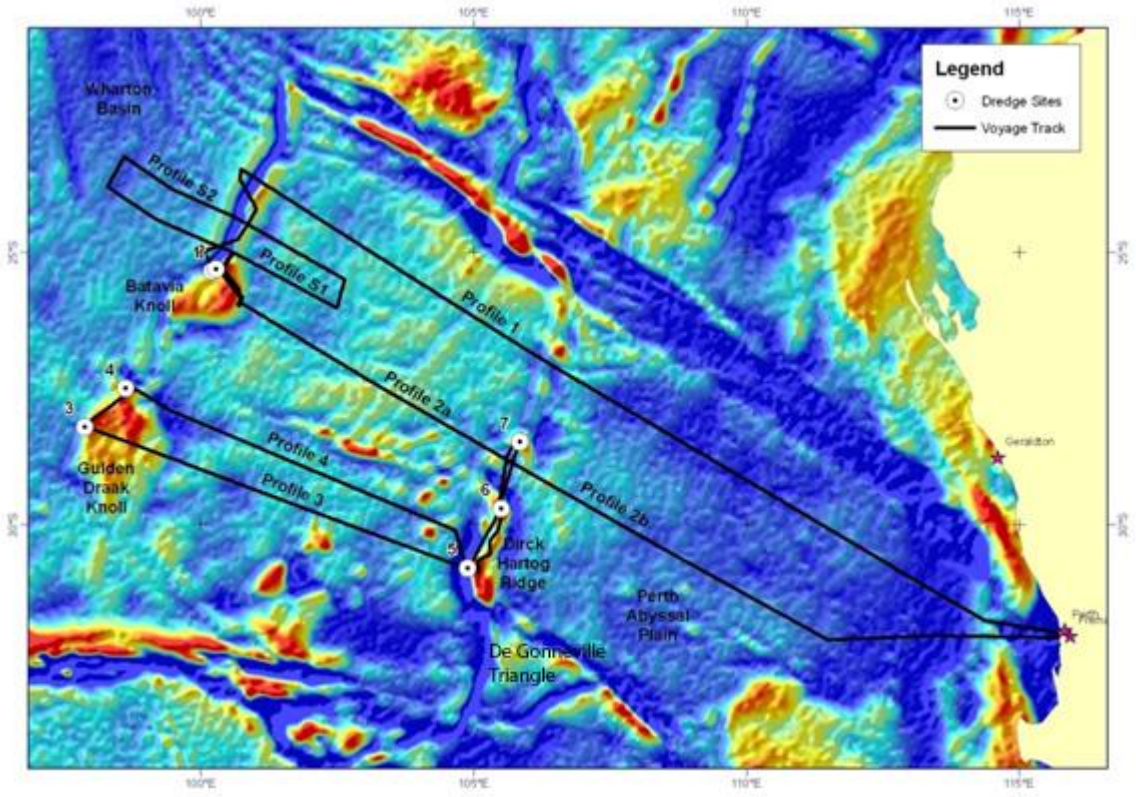

Fig. 2.1. Bathymetric map showing location of Batavia Knoll, voyage track including magnetic profiles and dredge locations.

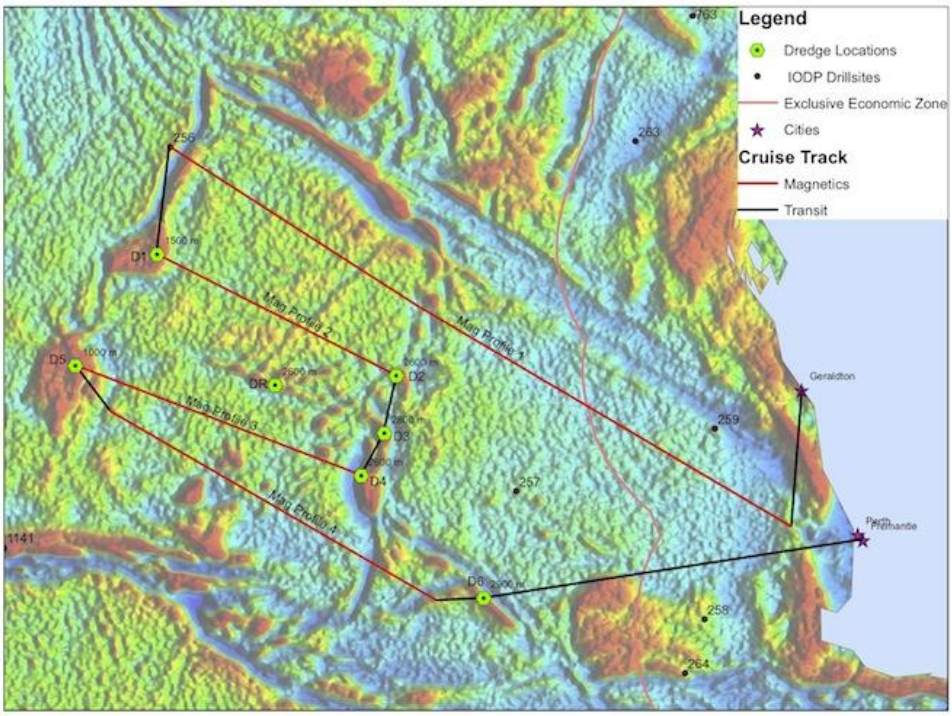

Fig. 2.2. Initial voyage planned track and planned dredge locations. Due to time constraints this track was adapted to above figure 2.1.

2.3 Methods

2.3.1 Dredging

The previously unmapped seafloor of dredge sites was imaged with multi beam swath bathymetry to identify good outcrop locations and record the shape and steepness of the slope. A Simrad EM 300 was utilised for depths shallower than 3000m and a 12 kHz echosounder and 3.5 kHz sub-bottom profiler were used for depths over 3000m. Once a suitable dredge location was found with a steep slope, shallower than 3500m water depth and predominantly rock, dredging began. A standard Southern Surveyor dredge with a maximum depth of 3500m (Fig. 2.3) was deployed off the back of the ship and winched out until it hit the bottom of the sea floor. The ship then sailed at approximately 2 knots, dragging the dredge along the seafloor. Tension of the wire was recorded, and gave a good indication of when the dredge got caught on rock. The dredge was then winched back in, and rock samples removed from the dredge. Rock samples were then washed, sawn with a rock saw, labelled and bagged to ensure no contamination between samples.

2.4 Results

The two aims of this fieldwork were successfully met; with an extra dredge undertaken (seven dredges in total). A list of all rocks from the two dredges on Batavia Knoll are presented in Table 2.1 at the end of this chapter. Hand sample images of all rocks from Batavia Knoll dredge are presented in Appendix B. However, due to time constraints related to initial findings, the aims of the voyage involving the "de Goneville triangle" were not met. For a more detailed description of the voyage, refer to Appendix A.

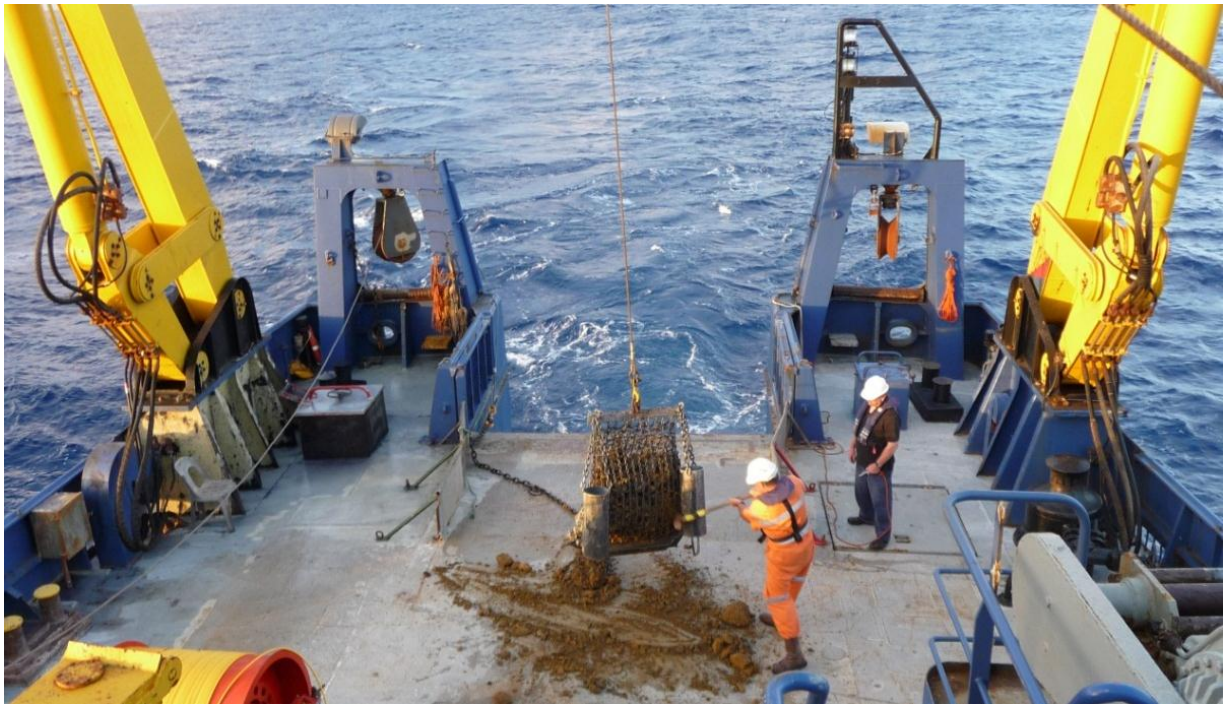

Fig. 2.3 Picture of standard Southern Surveyor Dredge.

2.5 Batavia Knoll Morphology

Due to the depth at which Batavia Knoll sits (approximately 2000-6000m below sea level), geological mapping has not occurred and spatial relationships between samples and outcrop patterns cannot be determined. Multibeam swath bathymetry was utilised to create an understanding of the morphology of the Knoll. The Falou trench runs N-W and sits to the west, with a maximum depth of approximately 6000m (Fig. 2.4a, Fig. 2.5). The western slope adjacent to the trench is very steep and rises 4000m within approximately 4500m, from 6000m to 2000m water depth. Deeply incised gullies are present on the western facing slope (Fig. 2.4a, Fig. 2.5). Due to the depth of the Knoll and the low water erosion rates at this location, it would be unlikely for these gullies to have formed in situ, indicating terrestrial fluvial erosion. The top of the Knoll is relatively flat and has corrugations running E-W, perpendicular to the Falou trench (Fig. 2.4b). The eastern side of the knoll gently grades into the Perth abyssal plain, reaching depths around 4000m (Fig.2.4c, Fig. 2.5). This slope is relatively uniform and does not have gullies.

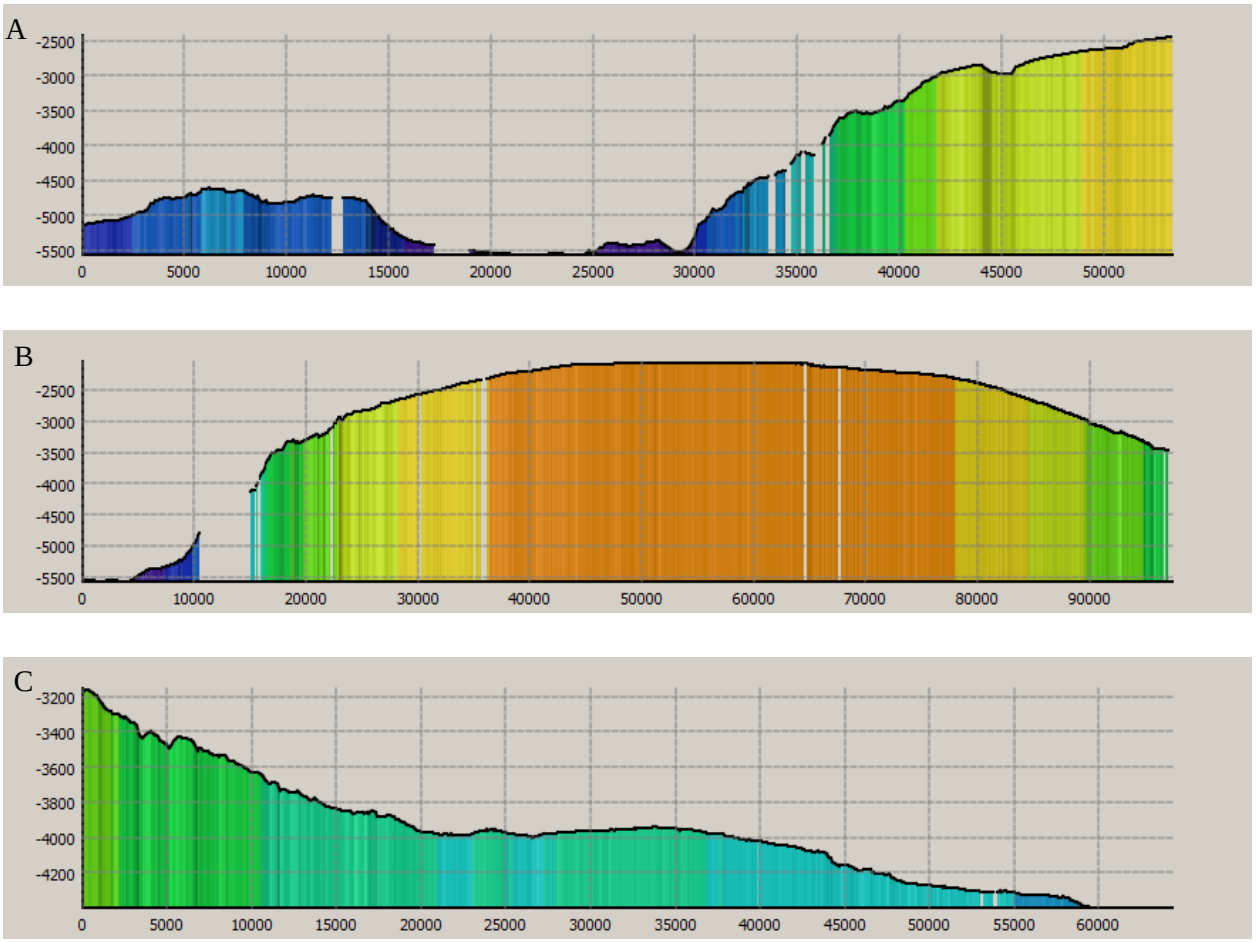

Fig. 2.4 a) Cross section of Falou trench and Western slope of Batavia Knoll. **b)** Cross section of Western slope and top of Batavia Knoll. **c)** Cross section of Eastern slope of Batavia Knoll, grading into the Indian Ocean. All sections W-E.

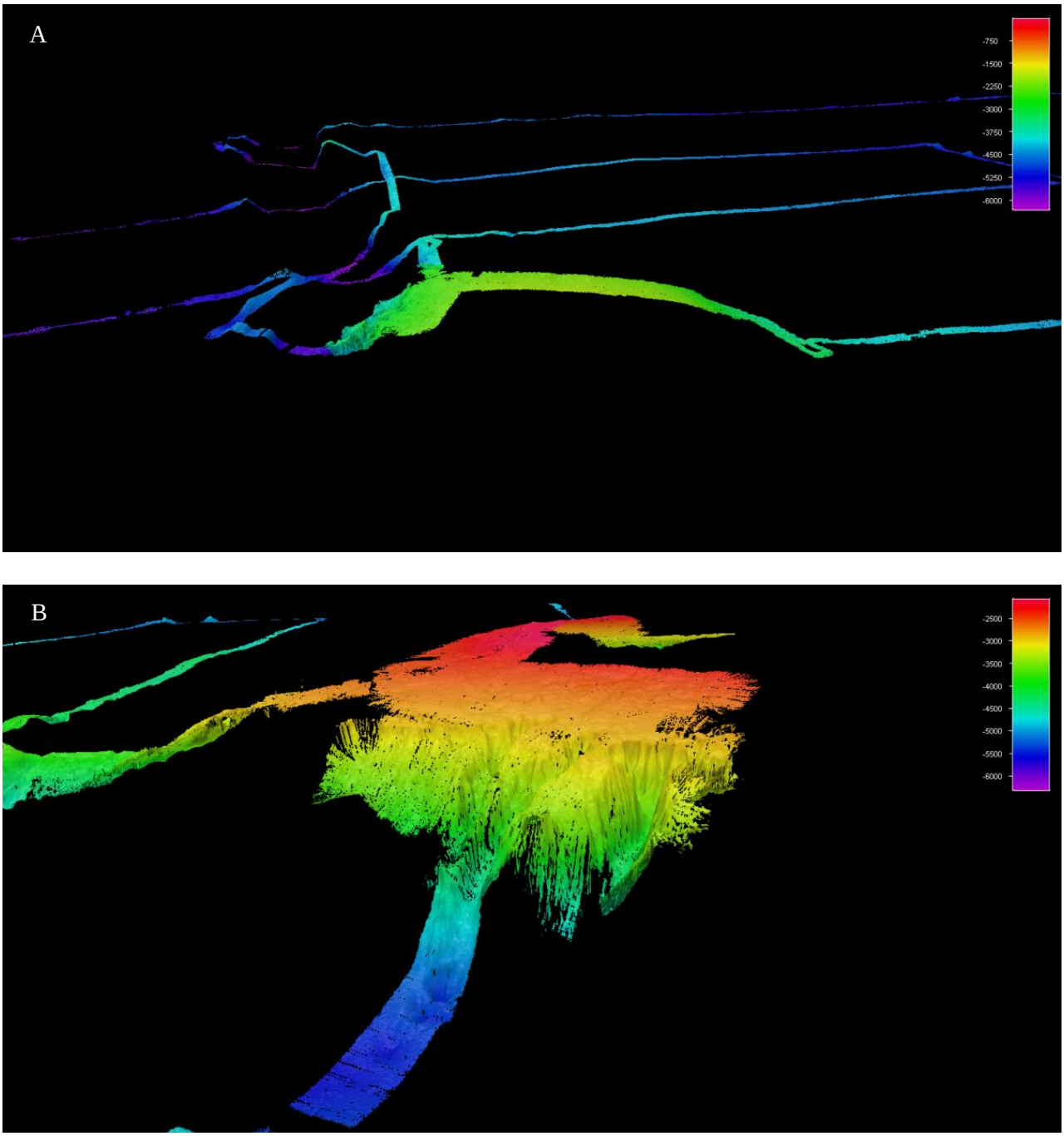

Fig. 2.5. a) Picture of Batavia Knoll and Falou Trench looking north. **b)** Oblique angle picture of Batavia Knoll looking north east.

Dredge one location

Dredge one occurred on the western face of the knoll in a steep gully (Fig. 2.6, Fig. 2.7). Dredging in a gully enabled the highest chance of sampling bedrock.

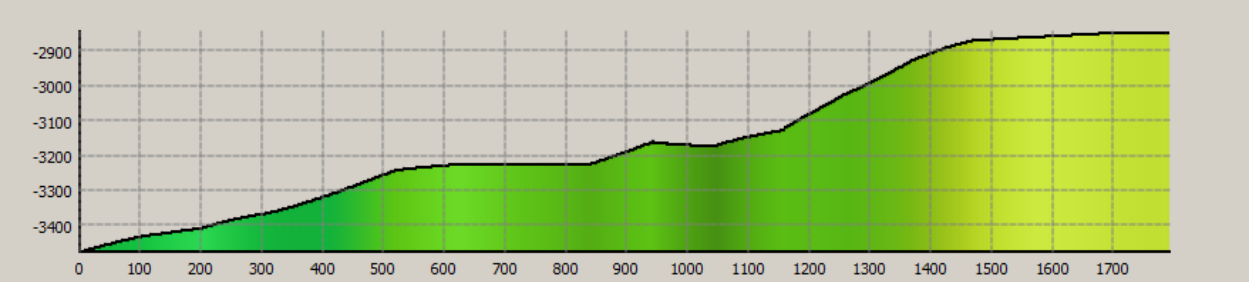

Fig. 2.6. Cross section of Dredge 1, Batavia Knoll. Location seen on Fig. 2.7.

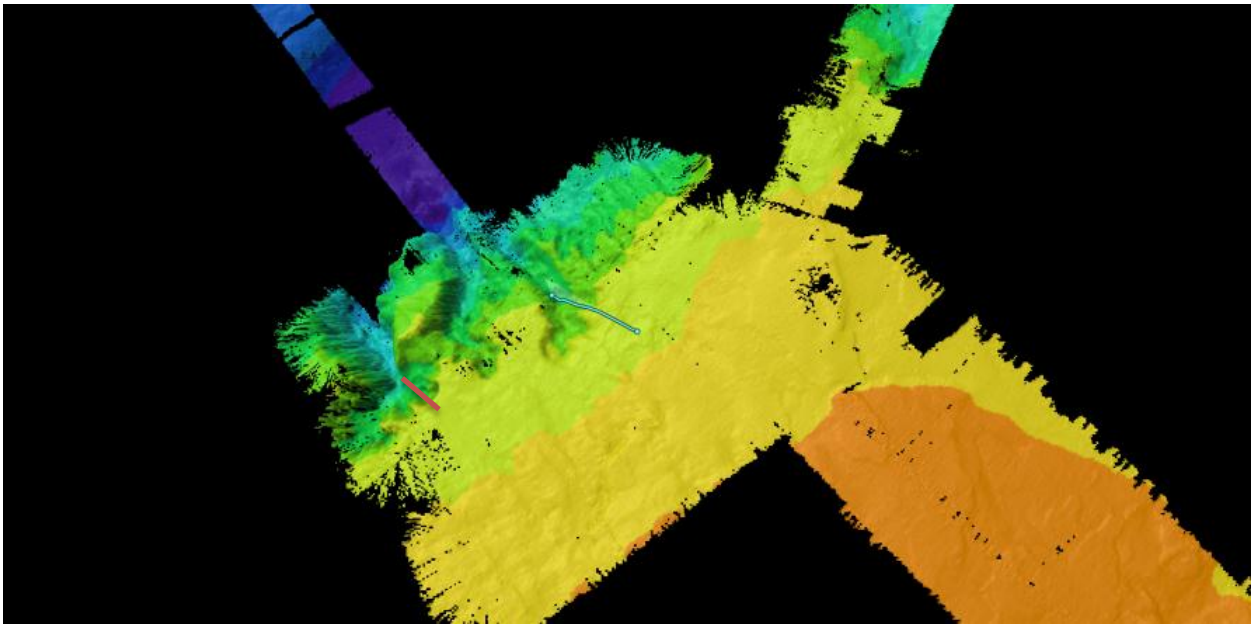

Fig. 2.7. Location of dredge one on Batavia Knoll, indicated by the red line. The light blue line indicates the location of dredge two.

Sample No.	**Sample Description**
DR1-1	Granite (2-5mm grainsize)
DR1-2	Granite (qtz-rich)
DR1-3	***Granite (5-30mm) - kfs-qtz-plag***
DR1-4	***Granite (qtz-rich) in contact with schist***
DR1-5	***Granite gneiss***
DR1-6	Granite gneiss (more felsic than DR1-5)
DR1-7	Granite pegmatite
DR1-8	Qtz vein or pegmatite?
DR1-9 - DR1-17	Granite (5-30mm)
DR1-18 - DR1-29	Granite (qtz-rich), some in contact with ksp-rich granite
DR1-30	Granite
DR1-31	Weathered granite
DR1-32	Intermediate gneiss (bt-rich, fine-grained)
DR1-33	Intermediate gneiss with granite layer
DR1-34	***Intermediate gneiss with <1cm thick granite layer***
DR1-35 - DR1-36	Intermediate gneiss
DR1-37	Chlorite schist (protolith=granite)
DR1-38	***Garnet granite gneiss***
DR1-39	Chlorite schist (less altered)
DR1-40 - DR1-41	***Garnet granite gneiss***
DR1-42	Intermediate gneiss
DR1-43	Biotite schist
DR1-44	Garnet granite gneiss
DR1-45 - DR1-47	Intermediate gneiss
DR1-48 - DR1-51	Fault gauge rock
DR2-1 - DR2-6	Yellow-orange fossiliferous sandstone
DR2-Bag1	Pebbles to fist-sized pieces of sandstones
DR2-Bag2	Brownish sandstone (3 samples)

Table 2.1. List of rocks dredged from Batavia Knoll. DR1 = dredge 1, DR2 = dredge 2. Locations of each dredge can be seen in Fig. 2.7. DR1 is the focus of this study; the rocks in bold and italic font represent the seven chosen for detailed analysis in this study.

Chapter 3 – Methodology

3.1 Sample selection

Sixty-one samples were dredged from Batavia Knoll (Table 2.1). Due to the large abundance of rock and the limited amount of time available for this study, the first dredge was the primary focus, with seven rocks chosen to undergo detailed petrographic, geochemical and geochronological characterisation to gain an overview of the whole dredge (Table 2.1). As such, the sandstone samples from the second dredge on Batavia Knoll will not be addressed in this study. These seven samples from the first dredge encompass the majority of rock types dredged, as well as appearing to be the freshest samples with the most representative mineral assemblages and textures of each rock type. The analysis of only seven samples enables greater detail to be obtained. Due to the unknown spatial relationships between these samples due to submergence under 2km of water, the following analytical techniques will be used to determine the characteristics of, and relationships between the seven rock samples.

Unless otherwise stated all sample preparation and analyses were undertaken in the Geochemical Analysis Unit (GAU) in the Australian Research Council National Key Centre for Geochemical Evolution and Metallogeny of Continents (GEMOC), situated in the Department of Earth and Planetary Sciences at Macquarie University, Sydney.

3.2 Petrography

Seventeen representative samples had the desired section of rock cut on a rock saw, polished to a flat surface on a grinding wheel and subsequently mounted onto a glass slide (25x75mm). These were then ground down to 30µm and polished. These samples were examined using a petrographic microscope and representative images were captured using a Canon EOS 300 digital SLR Camera. The seven most representative samples were then chosen for detailed characterisation.

3.3 X-ray fluorescence

Weathered sections of samples were removed using a diamond saw. A hydraulic press with tungsten carbide plates was used to mechanically crush selected pieces of fresh, unweathered rock into pieces no more than a cubic centimetre in size. The press was cleaned thoroughly with 100% ethanol between samples to prevent cross contamination. Approximately 100 grams of sample was then crushed in a TEMA tungsten carbide mill to a fine powder. The mill was cleaned with 100% ethanol and Milli-Q (18 Mohm) water between samples to prevent cross contamination.

Pressed powder pellets were prepared for trace element analysis by X-ray fluorescence (XRF). Approximately 6-6.5 grams of rock powder and 10-12 drops of elvanol solution were mixed together and then pressed to 80 kN in an aluminium cup. The pellets were dried in an oven at 120 °C for 2 hours. Samples were analysed on a Spectro XLAB2000 energy dispersive XRF spectrometer. Lower limits of detection for elements analysed are presented in Table 3.1. Standard Reference Materials BCR-2 and BHVO-2 were analysed to assess accuracy and precision and results are given in Table 2.2. The elements marked with an "n" have measured values outside 1sd error, and thus will not be used in the XRF chapter (Table 2.2). Loss of ignition was also measured by heating the samples to 1000°C for 1 hour.

Glass disks for major element analysis were prepared using 0.3g of powdered sample, 2.5g of 100% lithium metaborate flux and an ammonium iodide wetting agent. This mixture was heated to 1000°C in a furnace for ~15 minutes, and press-quenched into 30mm glass disks. Major element analysis was undertaken on a SPECTRO XEPOS energy dispersive XRF spectrometer machine in the Department of Geosciences, University of Wollongong.

Major	**Wt.%**	**Minor**	**ppm**	**Minor**	**ppm**
SiO_2	0.01	**V**	1	**Mo**	0.2
TiO_2	0.01	**Cr**	0.3	**Cd**	0.2
Al_2O_3	0.03	**Co**	0.4	**In**	0.3
Fe_2O_3	0.01	**Ni**	0.3	**Sn**	0.4
MnO	0.01	**Cu**	0.3	**Sb**	0.5
MgO	0.02	**Zn**	0.3	**Te**	1.0
CaO	0.01	**Ga**	0.3	**I**	1.0
Na_2O	0.04	**Ge**	0.2	**Cs**	1.5
K_2O	0.01	**As**	0.3	**Ba**	1..5
P_2O_5	0.01	**Se**	0.2	**La**	2.0
		Br	0.3	**Ce**	3.0
		Rb	0.3	**Hf**	2.0
		Sr	0.2	**Tl**	0.7
		Y	0.2	**Pb**	0.2
		Zr	0.2	**Bi**	0.5
		Nb	0.2	**Th**	0.5
				U	0.5

Table 3.1. Major and trace element lower limits of detection analysed by XRF

Element	BCR-2 Concentration (ppm)	1sd	Measured value	Within 1sd error?	BHVO-2 Concentration (ppm)	1sd	Measured value	Within 1sd error?
Ba	677	2	689	n	131	1	129.7	
Cd					0.06	0.006	0.5	
Ce	52.9	0.2	44.5	n	37.5	0.2	32.5	n
Co	37	3	34.6		45	3	41	
Cr	18	2	< 1.6	n	280	19	311.7	
Cs	1.1	0.1	< 1.5	n	0.1	0.01	< 1.5	n
Cu	21	1	19.4		127	7	128.5	
Ga	23	2	23.6		22	2	20.4	
Ge					1.6	0.1	< 0.3	n
Hf	4.9	0.1	3.3	n	4.36	0.14	< 2.0	n
La	24.9	0.2	21.9	n	15.2	0.1	11.6	n
Mn	1520	60	1452					
Mo	250	20	200.1	n	4	0.2	3.7	
Nb	12.6	0.4	10.9		18.1	1	16.6	
Nd	28.7	0.1	33.3	n	24.5	0.1	22.4	
Ni	18	1	11.6	n	119	7	115.5	
Pb	11	1	8	n	1.6	0.3	< 0.5	n
Pr	6.7	0.1	14	n	5.35	0.17	< 5.0	n
Rb	46.9	0.1	47.6	n	9.11	0.04	8.9	
Sb					0.13	0.04	< 0.5	n
Sn					1.7	0.2	1.7	
Sr	340	3	341.5		396	1	390.7	n
Ta					1.14	0.06	< 2.0	n
Th	5.7	0.5	4.9		1.22	0.06	< 0.5	n
U	1.69	0.19	< 0.5	n	0.403	0.001	< 0.5	n
V	416	14	442.9		317	11	327	
Y	37	2	35.9		26	2	26.6	
Zn	127	9	123.3		103	6	98.2	
Zr	184	1	181.1	n	172	11	165.5	

Table 2.2. Minor element standard concentrations and error (1 standard deviation) taken from GeoREM. Measured standard information also included. n = standard analyses outside 1sd error. Blank = within 1sd error.

3.4 Electron microprobe

The seven representative polished thin sections (30 µm) were cleaned with ethanol solution and lint-free tissues to remove all oil. Circles were then drawn around important textures and photographed to improve navigation during analysis. They were then carbon coated to provide an evenly conductive surface during analysis. Major element mineral analyses were carried out on a

CAMECA SX100 Electron Microprobe. Elements analysed include: SiO_2, TiO_2, Al_2O_3, Cr_2O_3, FeO, MnO, MgO, CaO, Na_2O, K_2O and P_2O_5. Instrument operating conditions included: count time of 10 seconds (peak and background), 15 KeV accelerating voltage and 20 nA beam current. Standards used were: K on orthoclase, Ca on $CaSiO_3$, Na on albite, Fe on Fe metal, Mn on spessartine, Al on kyanite, Si and Mg on olivine, P on apatite, Cr on Cr metal and Ba on $BaSO_4$. Lower limits of detection and relative standard deviation based on counting statistics are given in Table 2.2. Corrections were done by PAP software provided by CAMECA.

Element	**LLD (wt%)**	**% rsd**
SiO_2	0.03	0.27
TiO_2	0.02	0.19
Al_2O_3	0.01	0.18
Cr_2O_3	0.04	0.56
FeO	0.03	0.34
MnO	0.03	0.55
MgO	0.03	0.22
CaO	0.02	0.27
Na_2O	0.02	0.56
K_2O	0.01	0.49
NiO	0.03	0.30
P_2O_5	0.01	0.65
HfO_2	0.03	0.19
ZrO_2	0.09	0.30
Y_2O_3	0.03	0.34

Table 2.2. Lower limits of detection (LLD) and relative standard deviation (rsd) for major elements analysed on CAMECA SX100.

The CAMECA SX100 was also used to analyse the HfO_2, SiO_2, ZrO_2 and Y_2O_3 trace element concentrations of zircons to obtain compositions for LA-ICP-MS trace element quantification. Lower limits of detection and relative standard deviation are given in Table 2.2. Operating conditions were 15keV accelerating voltage and 20nA beam current, with a focused beam size of 1 μm. Lα emission lines were used to analyse Y, Hf, and Zr and Kα emission for Si. Natural mineral and synthetic standards were analysed for the elements provided in brackets – zircon (Zr, Si), yttrium aluminium garnet (Y), Hf wire (Hf).

3.5 Zircon separation and imaging

Standard techniques were used to separate individual zircon grains from each sample using SelFrag©. Approximately 200 grams of each sample was disintegrated. SelFrag© uses high powered electrical pulses to disaggregate rock along crystal edges. Due to the small size of zircon (typically < 500µm), a 400µm sieve, followed by a 200 µm sieve was used to separate zircon from larger crystals. These remaining grains were then panned in a two-directional fibre glass pan followed by a watch glass to achieve separation of minerals based on their densities, leaving behind zircon. A Frantz magnetic separator was used on intermediate gneiss sample DR1-34 to remove the more magnetic grains, however, no zircons were yielded. Zircons were then handpicked using a binocular microscope with a UV light attachment, picking all sizes, shapes and colours to ensure a representative sample. The selected grains were mounted in epoxy and polished to expose the internal structure of the grains.

A ZEISS EVO MA15 Scanning Electron Microscope (SEM) was used to obtain cathodoluminescence (CL) images of the zircon grains to see their internal structure. Using the CL images 40-50 representative zircon grains (all sizes, shapes and zoning patterns) were chosen from each sample to undergo further U-Pb and Lu-Hf isotope analysis.

3.6 Zircon U-Pb dating

The zircons were analysed by laser ablation microprobe-inductively coupled plasma mass spectrometry (LA-ICP-MS) using a an Agilent series 7700 LA-ICPMS, attached to a New Wave 213 nm Nd:YAG laser. For a more detailed description of the analytical procedures, refer to Jackson *et al.*, 2004. Operating conditions: spot size 40 and 30um (depending on grain size), intensity 12.97 J/cm^2, pulse rate 5 Hz, total counting time 180 seconds with a laser warm up of 58 seconds. A typical run included between 14-19 unknown zircons , bracketed with two analyses of GJ at the start and the end for external calibration of instrument drift and sensitivity. Reference zircons Mud Tank and 91500 were analysed in each run to assess accuracy and external reproducibility against published values: Mud Tank (732±5 Ma reported by Black & Gulson, 1987) and 91500 (1065±1.01 Ma reported by Wiedenbeck *et al.*, 1995). This study determined 91500 as giving 1068.3±6.1 (1sd; n= 16) with a MSWD = 1.2 and probability = 0.26. Mud Tank gave 733.5±3.8 (1sd; n=16) with a MSWD = 0.33 and probability = 0.993. Both of these values lie within the reported values, thus confirming the accuracy of the method. Certain grains (identified in Appendix B) were identified as having common lead and were corrected using the method of

Anderson (2002). Glitter (v.4) was used to initially reduce the isotope data. This study uses the $^{207}Pb/^{206}Pb$ ratio for zircon ages > 1Ga, and the $^{206}Pb/^{238}U$ ratio for zircon ages < 1Ga.

3.7 Zircon Lu-Hf isotope

A New Wave UP 213 nm laser ablation microprobe attached to a Nu Plasma multi-collector ICP-MS was used to measure Hf isotopes 176, 177, 178, 179 and 180 as well as Yb and Lu in zircon. Refer to Griffin *et al.,* 2000, 2004 for detailed information on the analytical method. Laser operating conditions included: beam diameter 55µm, 5Hz repetition rate, 75% power output. The method involved an ablation time of approx. 180 seconds including 30 seconds background counts. Each run was bracketed with one standard material Mud Tank, and Temora-2 was analysed at the start and end of day to assess accuracy and precision. Mud Tank was calculated with a mean of 0.282509±0.000010, within error (2sd) of the published value of 0.282522±0.000042 (Griffin *et al*., 2007). Temora-2 was calculated with a mean of 0.282668±0.000019, within error (2sd) of the published value of 0.282686 ± 0.000008 (Woodhead & Hergt, 2005). Only concordant grains identified from U-Pb dating were analysed. A crustal model age (T_{DM}) was calculated for individual grains. This age calculation assumes that the depleted mantle was the original source for the average continental crust ($^{176}Lu/^{177}Hf = 0.015$) from which the parental magma was derived. T_{DM} values were adopted from Blichert-Toft *et al.,* 1997 using a ^{176}Lu decay constant of $1.93x10^{-11}$.

Chapter 4 - Petrography

4.1 Introduction

Of the sixty one rocks dredged from Batavia Knoll (images presented in Appendix B), seventeen representatives from the first dredge were chosen to have thin sections made. On the basis of thin section analysis, seven of these samples were chosen to be petrographically analysed in detail to estimate mineral modes, characteristics and their microstructures (Table 4.1). These seven samples will be used throughout the entire study. Characterisation was used to identify textures and positions on the thin section for mineral chemistry electron microprobe analysis. It was also utilised to identify samples that contain zircon for U-Pb zircon dating. The intermediate gneiss sample does not show zircon in thin section, but zircon extraction was attempted. This section will add context to the upcoming U-Pb chapter, as high strain and deformation microstructures may indicate potential Pb-loss in zircon crystals. Due to the lack of knowledge on spatial relationships and outcrop patterns of these samples, hand sample images have been supplied to demonstrate the appearance of the rock. Certain samples have been grouped together to give an overall characterisation of each rock type:

Granite: DR1-3, DR1-4
Schist: DR1-4
Granite Gneiss: DR1-5
Garnet Granite Gneiss: DR1-38, DR1-40, DR1-41
Intermediate Gneiss: DR1-34

These groupings have been maintained throughout the rest of this thesis. The aim of this section is to undertake a reconnaissance characterisation of each rock sample to subsequently group rocks based on similarities and differences.

4.2 Granite (DR1-3, DR1-4)

Twenty-seven granite rock samples were dredged, two of which were selected for analysis in this study (Fig. 4.1). The granite samples are very light in colour in both hand specimen and thin section, dominated by leucocratic minerals. Samples are typically coarse grained (1-15mm) and

massive with no foliation, but show evidence for alteration and recrystallisation. They comprise K-feldspar, plagioclase, quartz, biotite ± minor myrmekite and zircon. Individual sample modes can be seen in Table 4.1.

Fig. 4.1. Left: Granite DR1-3 hand specimen. Right: Granite DR1-4 hand specimen. Of note is the schist layer on the top of DR1-4.

The K-feldspar grains are typically interstitial to the quartz and plagioclase grains (Fig. 4.2). Extensive sericite alteration is found at the edges, in the middle and along planes of weakness such as twins and fractures, alongside a wispy, perthitic texture (Fig. 4.2). Minor myrmekite is found at the grain boundaries between K-feldspar and quartz following that of the grain boundaries in DR1-3, but is absent in DR1-4 (Fig. 4.2).

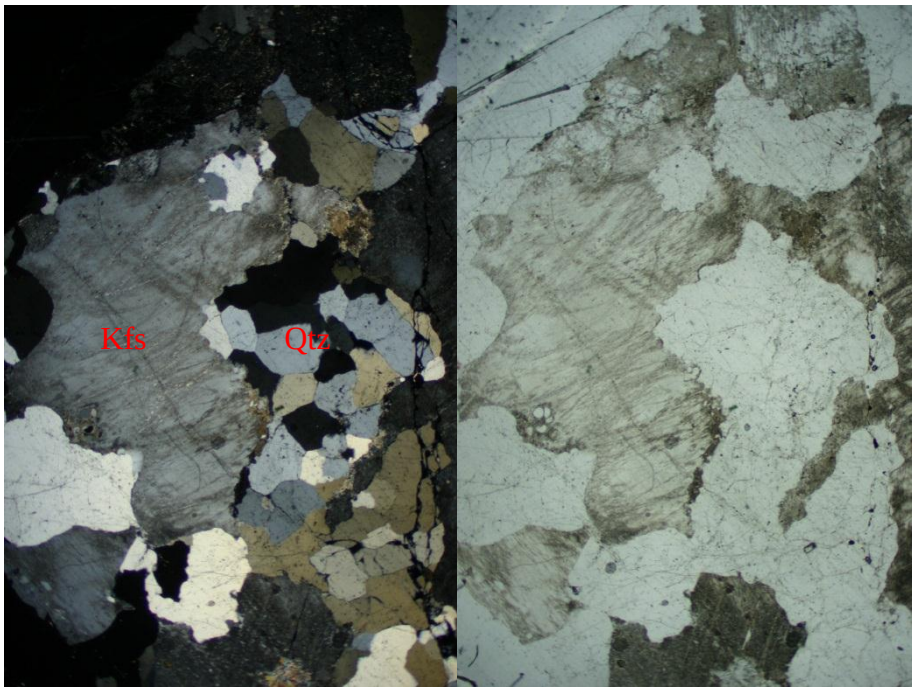

Fig. 4.2. Sample DR1-3. Interstitial characteristic of K-feldspar (Kfs) grain, alongside wispy perthitic texture and sericite alteration. Relict rectangular quartz (Qtz) grain outlined by a domain of recrystallised quartz. Photo width 7mm. Left = Crossed polarised light (XPL). Right = Plane polarised light (PPL).

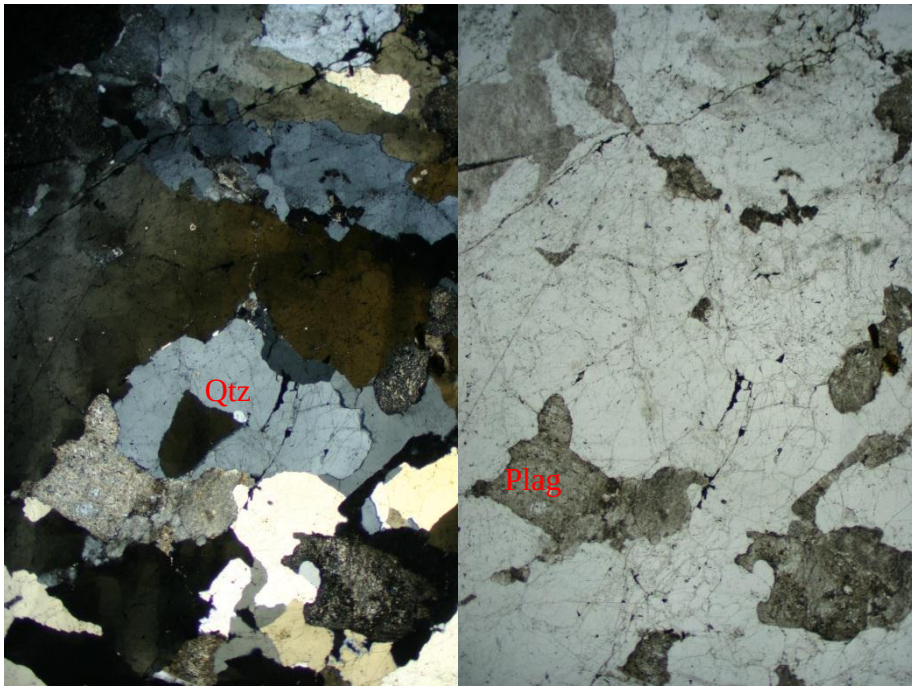

Fig. 4.3. Sample DR1-4. Tabular plagioclase (Plag) crystals with sericite alteration alongside undulose extinction in quartz (Qtz) grains. Photo width 7mm. Left = XPL. Right = PPL.

Plagioclase grains have an overall euhedral crystal habit with sericite alteration common along planes of weakness (Fig. 4.3).

Larger quartz grains (not recrystallised grains within relict quartz grains (Fig. 4.2)) typically have lobate or irregular crystal shape with undulose extinction (Fig. 4.3). Smaller grains (domain of recrystallised quartz) with a granoblastic polygonal crystal habit and 120º dihedral angles are present in DR1-3, and are typically found in a larger, rectangular grain (Fig. 4.2).

Biotite has both euhedral (as inclusions in plagioclase and K-feldspar) and anhedral crystal habits within DR1-3 (Fig. 4.4). Biotite is rare in DR1-4 with anhedral crystal edges, forming stubby grains. It exhibits a red/brown pleochroic colour. Chlorititisation is common along cleavage planes.

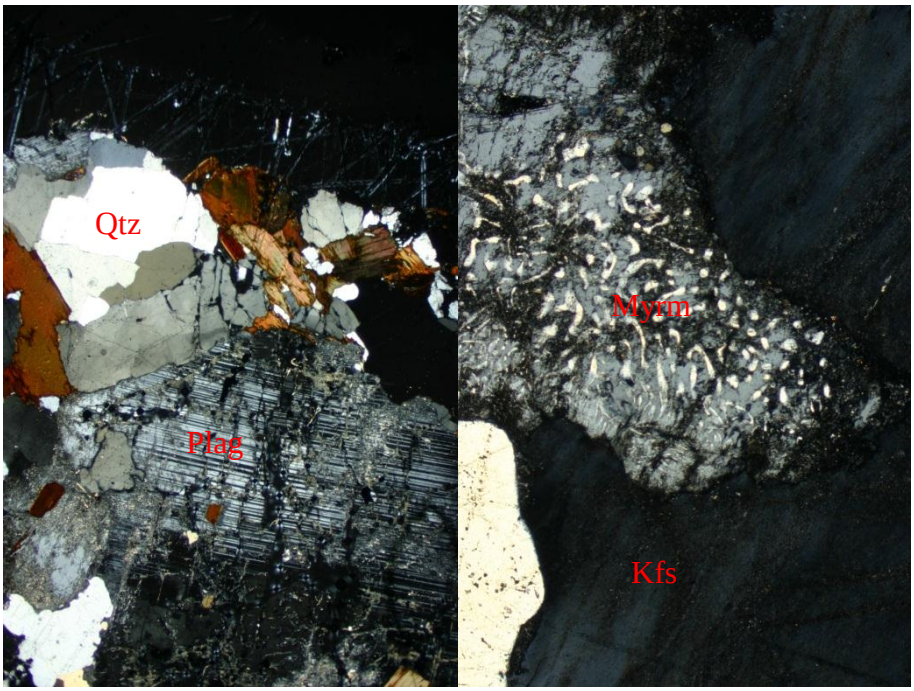

Fig. 4.4. Left: Sample DR1-3. Anhedral, stubby crystal habit of biotite (Bt) with chloritisation along cleavage planes, alongside sericite alteration in plagioclase (Plag) and recrystallised quartz (Qtz). Photo width 7mm. XPL. Right: Sample DR1-3. Myrmekite (Myrm) at boundary of K-feldspar and quartz grains. Photo width 1.7mm. XPL.

Summary

The key features of this rock group include an igneous origin with a metamorphic overprint and evidence for alteration. Overall, sample DR1-3 shows more evidence of strain then DR1-4.

Recrystallised quartz and symplectic intergrowths are found in DR1-3, and are absent in DR1-4. The rectangular crystal habit of plagioclase in both samples is retained and biotite chloritisation and sericite alteration of feldspar is extensive in both samples.

4.3 Schist (DR1-4)

Four schist rock samples were dredged, one of which will be analysed in detail (Fig. 4.1). The schist is fine grained with a well-defined foliation in hand specimen and thin section. It is part of DR1-4 in contact with granite and comprises biotite, quartz and plagioclase. Sample modes can be seen in Table 4.1.

Biotite has both euhedral (elongate, found in contact with other biotite grains) and subhedral (stubby, in contact with quartz and feldspar) crystal habits. It defines a strong foliation through the schist, with elongate, smaller grains wrapping around a large, porphyroblast of quartz (Fig.4.5). It exhibits a green/brown colour in plane polarised light. Grains close to the schist / granite contact have extensive chloritisation along cleavage planes.

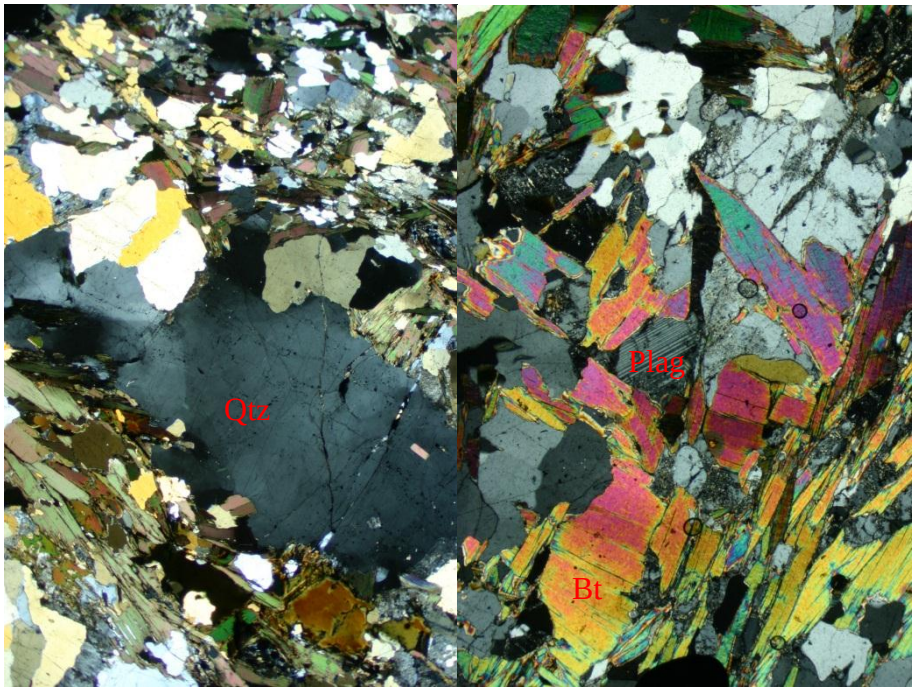

Fig. 4.5. Left: Sample DR1-4. Foliation defined by biotite (Bt), seen wrapping around a quartz (Qtz) porphyroblast. Photo width 7mm. XPL. Right: Sample DR1-4. Close up on biotite grains. Photo width 1.7mm. XPL.

The quartz grains have sutured grain boundaries, tending to bulge into adjacent grains with undulose extinction. 120° dihedral angles between quartz grains are common. Elongate grains with euhedral crystal edges are found when in contact with the biotite. Biotite inclusions are common and rounded quartz inclusions <0.1mm are found in biotite and K-feldspar. Symplectic intergrowths with both biotite and K-feldspar are found at the contact of the schist and granite.

Plagioclase grains are subhedral to anhedral with minor sericite alteration and twins.

Summary

This rock group is distinguished by significant strain evident through the alignment of biotite and recrystallised quartz.

4.4 Granite Gneiss (DR1-5)

One of the two granite gneiss rock samples that were dredged will be analysed in detail (Fig. 4.6). The granite gneiss exhibits a well-defined foliation in thin section and hand specimen, dominated by leucrocratic minerals, with smaller darker bands predominantly of biotite. Grain size ranges from medium (leucrocratic) to fine grained (melanocratic). Minerals include quartz, biotite, plagioclase, and K-feldspar. Mineral characteristics and modal percentages differ between the dark and light bands of this rock (Table 4.1).

Fig. 4.6. Granite gneiss DR1-5 hand specimen.

K-feldspar exhibits an interstitial crystal habit, with moderate sericite alteration focused at crystal edges and along fracture planes (Fig. 4.7).

Quartz grains are typically anhedral with sutured grain boundaries, commonly bulging into adjacent grains (Fig. 4.7). Grains with 120° dihedral angles and undulose extinction are common. Rounded inclusions of sericite altered K-feldspar occur.

Both euhedral and subhedral plagioclase grains with moderate sericite alteration, focused along fracture planes and the middle of the grains are found (Fig. 4.7, Fig. 4.8). Rectangular grains are porphyroblastic while subhedral grains define the foliation. Euhedral and rounded inclusions of biotite and rounded quartz are common.

Biotite forms a distinct foliation which is pervasive in thin section and in hand sample (Fig. 4.8). Elongate crystal habit is common, with euhedral sides and anhedral ends. Quartz embayments are common in the anhedral faces. Monazite and zircon are concentrated as inclusions in biotite.

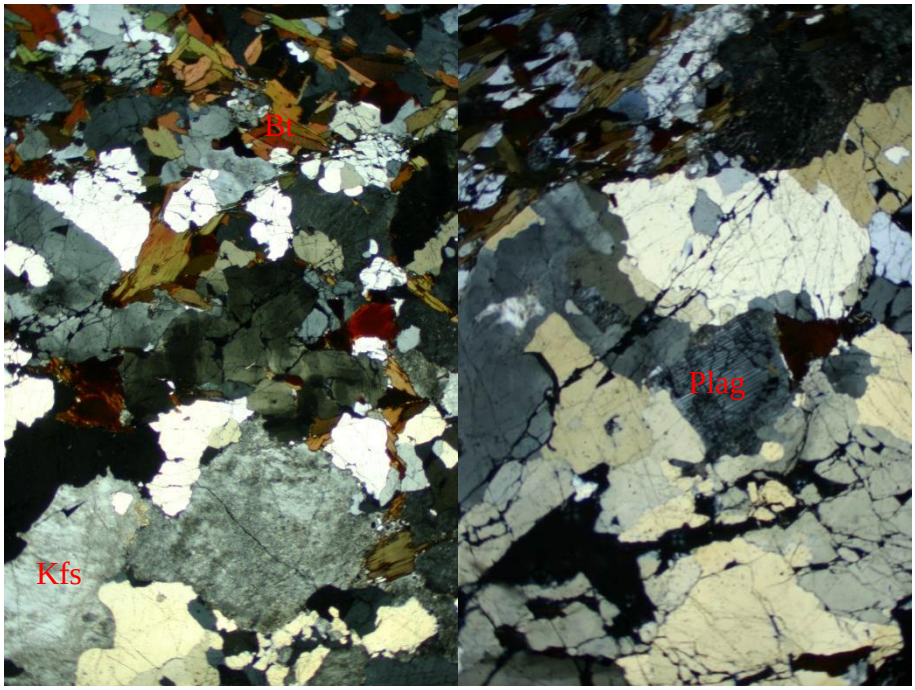

Fig. 4.7. Left: Sample DR1-5. Recrystallised quartz (Qtz) with undulose extinction. K-feldspar (Kfs) exhibits an interstitial crystal habit with sericite alteration and a wispy perthitic texture. Photo width 7mm. XPL. Right: Sample DR1-5. Rectangular plagioclase (Plag) grain with sericite alteration. Photo width 7mm. XPL.

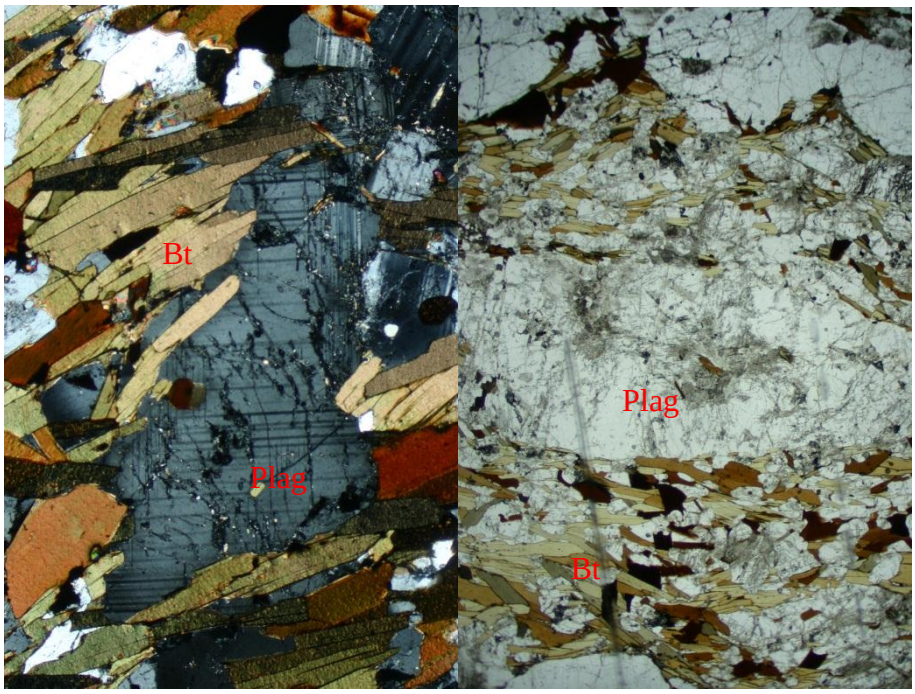

Fig. 4.8. Left: Sample DR1-5. Metamorphic plagioclase (Plag) grain surrounded by biotite (Bt). Photo width 1.7mm. XPL. Left: Sample DR1-5. Distinct foliation defined by biotite. Photo width 7mm. PPL.

Summary

The key features of this rock group include an igneous origin with a metamorphic overprint, alongside evidence for alteration. There is distinct light and dark banding throughout the rock with foliation defined by biotite, alongside recrystallised quartz and metamorphic plagioclase. However, rectangular plagioclase grains remain. Alteration is also evident through chloritised biotite and sericite alteration of feldspar.

4.5 Garnet Granite Gneiss (DR1-38, DR1-40, DR1-41)

Three of the four garnet granite gneiss rock samples dredged will be analysed in detail (Fig. 4.9). There are two types of garnet granite gneiss: group A (DR1-38, DR1-41) with coronal garnet breakdown textures and group B (DR1-40) without. Minerals include garnet, quartz, plagioclase, biotite, chlorite ± K-feldspar ± orthopyroxene with minor zircon and monazite. Both groups have a defined foliation in hand specimen (Fig. 4.9); group A fine grained and group B course grained. Individual sample modes can be seen in Table 4.1.

Fig. 4.9. Top left: Sample DR1-38. Top right: Sample DR1-40. Bottom centre: Sample DR1-41.

Quartz grains typically meet at 120° dihedral angles with undulose extinction and sutured grain boundaries in samples DR1-38 and DR1-40. Sample DR1-41 exhibits elongated quartz grains that define the foliation (Fig.4.10).

Plagioclase exhibits both euhedral and anhedral (found bordering quartz) crystal habits. Sericite alteration at grain boundaries and along twin planes is common. Kinked, bent, truncated and cross cutting twins are common in Group A, whilst undeformed twins are present in DR1-40.

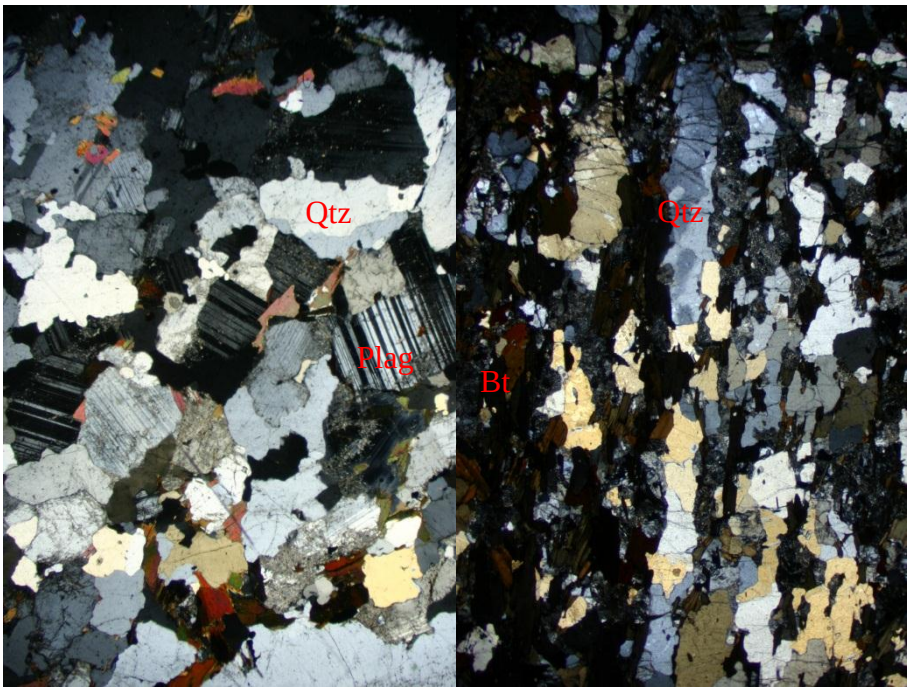

Fig. 4.10. Left: Sample DR1-38. Granoblastic polygonal recrystallised quartz (Qtz) grains. Photo width 7mm. XPL. Right: Sample DR1-41. Elongate quartz grains helping to define the foliation, alongside biotite (Bt). Photo width 7mm. XPL.

Biotite has an elongate crystal habit and forms a distinct pervasive foliation in thin section and hand sample in group A (Fig. 4.10). Chloritisation along cleavage planes is common. Group B biotite is rare with an anhedral stubby crystal habit.

Garnet differs between group A and B. Group A garnet is present only in the biotite rich layers. There is a corona texture surrounding the garnet of biotite and plagioclase; both of which are smaller than in garnet-free areas of the rock (Fig. 4.11). Group B garnet is porphyroblastic with subhedral crystal habit and no corona texture. Inclusions of plagioclase, quartz and biotite are common (Fig. 4.12).

Clinopyroxene is found in sample DR1-38 being partly pseudomorphed by chlorite, exhibiting a radiating texture (Fig. 4.12). It is found in the biotite rich layers.

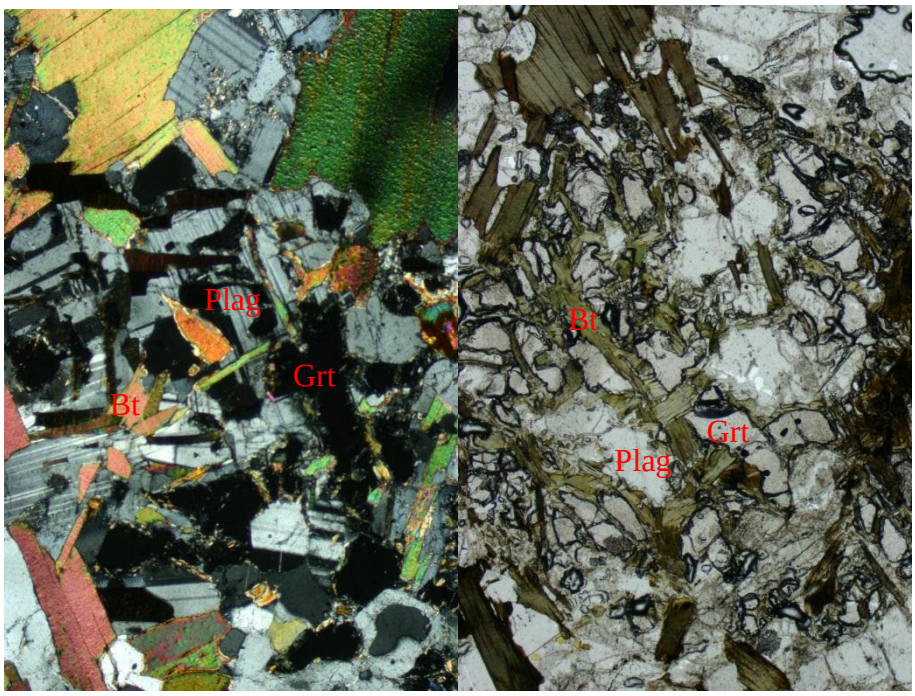

Fig. 4.11. Sample DR1-38. Coronal texture of garnet (Grt) with smaller biotite (Bt) and plagioclase (Plag) grains within the texture. Photo width 1.7mm. Left = XPL. Right = PPL.

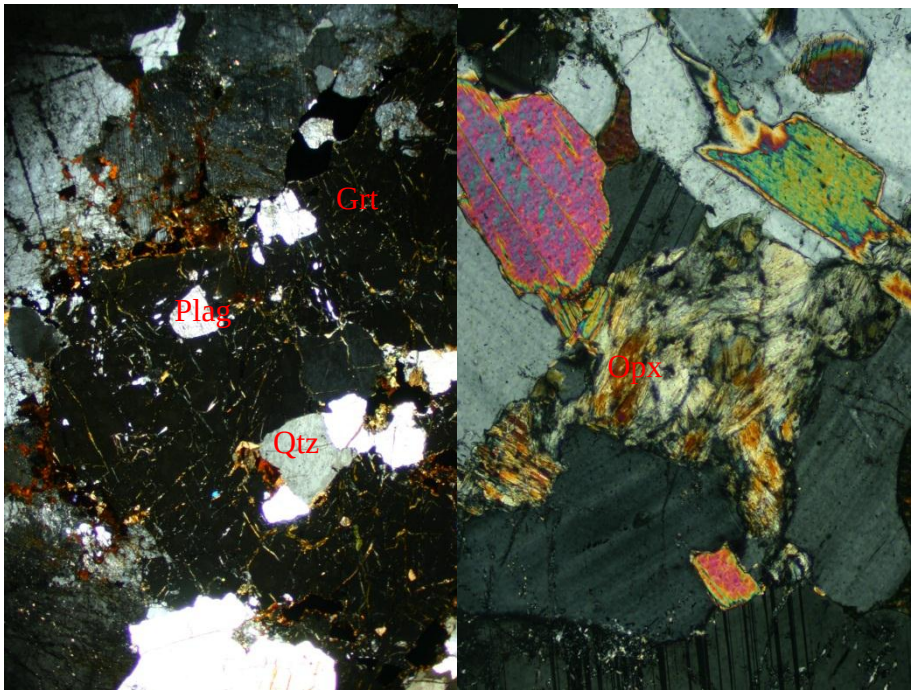

Fig. 4.12. Left: Sample DR1-40. Porphyroblastic garnet (Grt) with inclusions of plagioclase (Plag) and quartz (Qtz). Photo width 7mm. XPL. Right: Sample DR1-38. Orthopyroxene (Opx) partly pseudomorphed by chlorite. Photo width 0.7mm. XPL.

Summary

This rock group is defined through the presence of garnet. Both groups of garnet granite gneiss show evidence for significant strain and alteration. Distinct banding and foliation is present alongside chlorisitaion of biotite and sericite alteration of feldspar. Sample DR1-41 appears to have undergone slightly more strain than DR1-38, seen through the elongated quartz that follows the foliation. Group A is distinguished from group B through the presence of the coronal texture.

4.6 Intermediate gneiss (DR1-34)

Eight intermediate gneiss rock samples were dredged, one of which was chosen for detailed analysis (Fig. 4.13). The intermediate gneiss is noticeably darker than the other samples, dominated by melanocratic minerals such as biotite, amphibole and pyroxene. A defined foliation is present in thin section and hand sample. Minerals present include quartz, plagioclase, biotite, diopside and orthopyroxene. There is a feldspar-rich vein, which contains quartz, plagioclase and K-feldspar. See Table 4.1 for individual samples modes.

Fig. 4.13. Sample DR1-34. Of note is the leucocratic vein on the end of the gneiss sample.

Amphibole grains are poikiloblastic with rounded inclusions of plagioclase and quartz, helping to define the foliation (Fig. 4.14). Amphibole grains are found in higher abundance near the vein, and grains further from the vein appear partly altered (Fig. 4.14). Inclusions are more pronounced in the

intact grains near the contact with the vein. The more pseudomorphed grains appear to be very irregular while the more intact grains are subhedral to anhedral.

Biotite exhibits a long, elongate crystal habit forming a distinct foliation (Fig. 4.14). Grain size becomes coarser towards the vein, with grains wrapping around the minerals at the contact of the vein.

Pyroxene is found as small equiangular euhedral porphyroblasts with distinct crystal edges (Fig. 4.15). Some edges appear to have grown around pre-existing minerals.

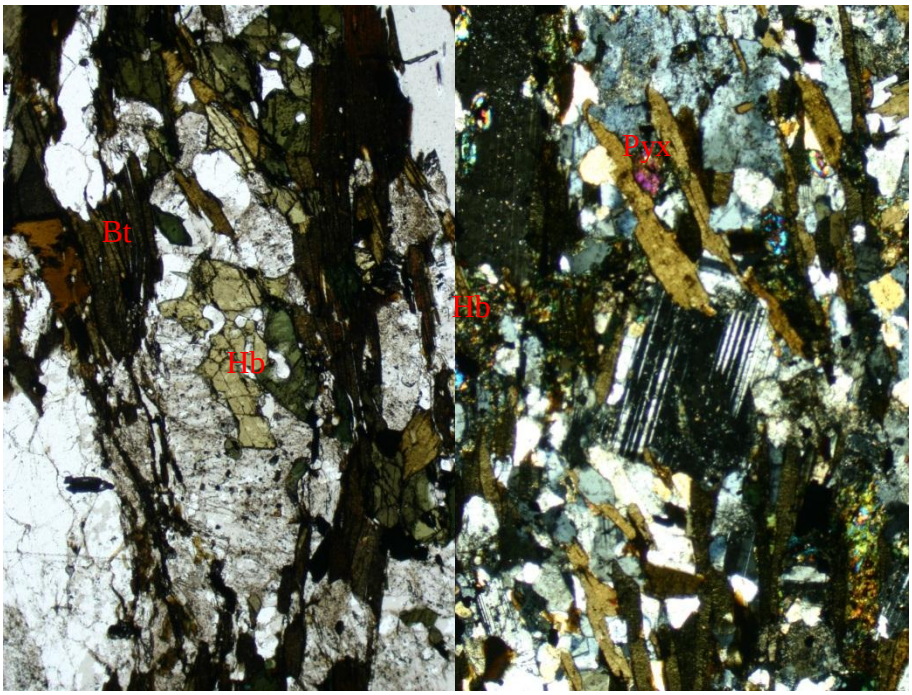

Fig. 4.14. Left: Sample DR1-43. Intact crystal of amphibole (Hb) with inclusions of quartz (Qtz) and plagioclase (Plag). Biotite (Bt) is present forming a distinct foliation. Photo width 1.7mm. PPL. Right: Sample DR1-34. Small crystal of pyroxene (Pyx), as well as partly altered amphibole crystals. Photo width 1.7mm. XPL.

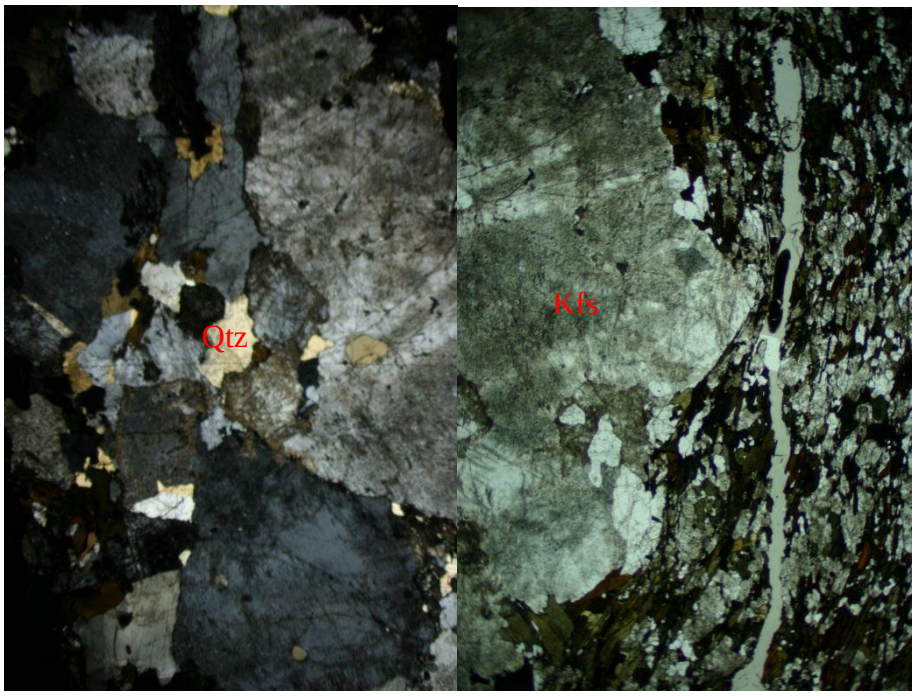

Fig. 4.15. Left: Sample DR1-34. Wispy, sericite altered K-feldspar (Kfs) grains from the vein. Photo width 7mm. XPL. Right: Sample DR1-34. Contact of vein and gneiss with biotite (Bt) wrapping around the K-feldspar grain. Photo width 7mm. XPL.

Plagioclase grains define the foliation with long, subhedral (and sometimes stubby) crystal habits. Twins can be seen with moderate sericite alteration distributed across all areas of grains.

Quartz grains have a distinct polygonal habit (Fig. 4.14). Opaque grains exhibit the same shape and size of the quartz grains.

The leucocratic vein is comprised predominantly of K-feldspar with a wispy texture (Fig. 4.15). Quartz, plagioclase and rare biotite are also present. Grain size is relatively larger compared to the main rock matrix.

Summary

This rock group is defined by its smaller grain size compared to the other groups, as well as the presence of orthopyroxene and amphibole. The mineral assemblage of this rock is indicative of amphibolite facies metamorphism.

Sample	Mineral	Mode %	Size (mm)	Shape	Comments
Granite DR1-3	K-Feldspar	40	5-10	Rectangular and Irregular / euhedral and anhedral	Sericite alteration and a wispy texture.
	Plagioclase	35	15-7	Rectangular / euhedral	Sericite alteration and twins.
	Quartz	20	3-<0.5	Granoblastic polygonal	120° angles, undulose extinction, recrystallised within shape of older larger grains.
	Biotite	5	3-<0.5	Rectangular / euhedral	Chloritisation along cleavage planes.
	Myrmekite	Minor	1-<0.5	Irregular / anhedral	Found at contacts between quartz and k-feldspar
DR1-4 (schist layer)	Biotite	60	1x0.5-<0.5	Long, elongate; square	Green in PPL. Chloritisation along cleavage planes.
	Quartz	30	<0.5	Irregular (sutured)	Undulose extinction, sutured and 120° angles
	Plagioclase	10	1-<0.5	Irregular	Sericite alteration and twins.
DR1-4 (granite layer)	Quartz	90	7-1	Sutured	Undulose extinction, sutured and bulging edges.
	Plagioclase	8	5-1	Irregular	Sericite alteration, interstitial between quarts grains.
	Biotite	2	1x1	Truncated, crystal edges evident	Brown due to higher Fe compared to schist layer? Chloritisation along cleavage planes.
Granite Gneiss DR1-5	Quartz	45	10-<0.5	Irregular, sutured	120° angles, undulose extinction.
	Biotite	35	2x0.5-<0.1	Long and elongate	Forms a defined foliation. Rich in monazite / zircon.
	Plagioclase	10	5- 1x1	Rectangular and Irregular	Sericite alteration, relict twins. Rectangular indicates igneous origin.
	K-feldspar	10	5- 1x1	Interstitial	Sericite alteration
Intermediate Gneiss DR1-34	Biotite	40	1x <0.1 – 0.1x0.1	Long and elongate	Forms a distinct foliation. Courser towards the vein
	Plagioclase	20	2x0.5 – 0.1x0.1	Rectangular and irregular	Helps form the foliation. Twins and moderate sericite alteration are present.
	Amphibole	15	2x0.5 – 0.1x0.1	Subhedral – anhedral	Poikiloblastic with inclusions of quartz and plagioclase. Altered away from
	Quartz	15	0.1x0.1	Very polygonal	
	Orthopyroxene	5	0.1x0.1	Euhedral – subhedral, polygonal	Small, unaltered grains
	Opaques	5	0.1x0.1	Polygonal	Same size and shape as quartz grains.
Garnet Granite Gneiss DR1-38	Quartz	30	7-0.5	Irregular, sutured, granoblastic polygonal	Biotite inclusions (<0.1mm, rectangular). Some undulose extinction.
	Plagioclase	30	3-0.5	Square, some irregular mainly near quartz	Deformation twins. Sericite alteration, mostly at grain boundaries.

	Biotite	20	1-<0.1	Elongate (schist), stubby irregular (granite)	Chloritisation along cleavage planes. Forms foliation in biotite rich layer. Not abundant in the plagioclase/quartz section.
	Garnet	5	<0.5	Irregular	Breakdown texture= smaller plagioclase and biotite within corona texture.
	Clinopyroxene	10	< 1	Radiating	Partly pseudomorphed by chlorite, with a radiating texture
	Opaques	5	1x1 - <0.5		
Garnet Granite Gneiss DR1-40	Quartz	35	.1x.1 - .5x.2	Granoblastic polygonal	120° angles. Undulose extinction. In some cases, recrystallised in old relict grains. Monazite and zircon inclusions with internal zoning obvious.
	Plagioclase	35	.25x.25 - .5x.35 – 1x1	Rectangular and irregular	Sericite alteration in the centre and along cracks.
	Garnet	20	12x9	Irregular, blob like	Porphyroblastic. Inclusions of quartz, plagioclase and biotite. The smaller inclusions of plagioclase and quartz (<0.1) are rounded, the larger ones more square (1x1). Biotite is chloritised and has a stubby crystal habit.
	Opaques	5	2x2 - <0.1	Irregular	
	Biotite	minor	.5x.5	Short and stubby	
Garnet Granite Gneiss DR1-41	Biotite	50	2.5x0.5 - <0.2	Elongate	Forms a foliation. Smaller grains found near garnet. Chloritisation along cleavage planes.
	Quartz	30	3x1 - <0.1	Elongate	Forms a foliation, is long and stung out.
	Plagioclase	15	1x1- <0.1	Euhedral	
	Garnet	5	<0.2	Subhedral	Breakdown texture= smaller plagioclase and biotite in corona

Table 4.1. Table showing mineral modes, sizes, shape and general characteristics for the seven representative Batavia Knoll rock samples.

Chapter 5 –Major and Minor Bulk Rock Chemistry by X-ray Fluorescence

5.1 Introduction

X-ray fluorescence (XRF) is a standard geochemical technique used for determining the major and minor trace element compositions for representative whole rock analyses. The aim of this chapter is to provide a reconnaissance characterisation of the seven representative rock samples from this study and to determine the relationships, or lack thereof between samples. The data will also be used to determine the degree of alteration of each sample.

5.2 Results

Seven samples were analysed for major (Table 5.1) and minor (Table 5.2) bulk rock chemistry by XRF.

Major Element (Wt. %)	DR1-3	DR1-4	DR1-5	DR1-34	DR1-38	DR1-40	DR1-41
SiO_2	68.8	73.49	69.57	74.53	73.94	76.21	63.99
TiO_2	0.53	0.57	0.59	0.4	0.23	0.61	1.42
Al_2O_3	12.23	13.74	14.57	14.1	14.58	11.32	14.82
Fe_2O_3	6.86	5.25	5.66	2.97	1.46	6.99	8.12
MnO	0.14	0.05	0.06	0.03	0.02	0.03	0.08
MgO	3.43	1.8	1.79	< 0.01	0.2	< 0.01	2.79
CaO	2.27	0.76	0.76	0.34	1.26	2	2.33
Na_2O	0.79	0.12	0.21	2.38	0.93	1.14	1.12
K_2O	2.05	2.57	2.38	4.78	5.67	0.68	2.2
P_2O_5	0.19	0.12	0.12	0.17	0.15	0.14	0.31
SO_3	0.05	0.03	0.04	0.03	0.02	0.01	0.05
LOI	1.09	0.83	1.38	1.45	1.77	0.43	0.91
Total	98.42	99.33	97.12	101.18	100.23	99.56	98.14

Table 5.1. Major weight percent oxide data for seven representative rock samples. LOI = loss on ignition.

Minor Element (ppm)	DR1-3	DR1-4	DR1-5	DR1-34	DR1-38	DR1-40	DR1-41
V	< 5.4	7.7	30.6	107	120	N/A	N/A
Cr	12.5	4.1	83.5	27.4	153.9		
Mn	0.00396	0.00433	0.0083	0.09222	0.118		
Fe	0.3734	0.485	2.255	7.289	5.072		
Co	72.7	107.3	83.4	36.4	59.1		
Ni	< 0.8	< 0.8	9.7	35.5	35		
Cu	6.6	5.1	7	22.3	64.8		
Zn	< 0.4	< 0.4	< 0.4	196.9	66.5		
Ga	12.9	9.2	17.9	21.9	18.1		
Ge	2.3	11.4	3.7	< 0.3	1.5		
As	< 0.3	1.5	1.1	< 0.3	2.1		
Se	1.3	1.7	1.1	< 0.2	0.2		
Rb	319.9	102.7	213.1	191.6	178.6		
Sr	163.1	58.8	144.6	770.7	124.7		
Y	13.8	10.3	7.5	73.6	24		
Zr	72.8	99.6	327.6	469.1	211.9		
Nb	8.6	8.9	15	31.7	12.5		
Mo	0.5	0.2	< 0.2	1.6	1.7		
Ag	< 0.8	< 0.8	< 0.8	< 0.8	< 0.8		
Cd	< 0.2	< 0.2	< 0.2	0.4	< 0.2		
Sn	2.1	1.5	3.2	3.7	6.6		
Sb	< 0.5	< 0.5	< 0.5	< 0.5	< 0.5		
Te	< 0.2	< 0.1	< 0.2	< 0.3	< 0.2		
Cs	5.4	3.9	4.7	3	9		
Ba	962.5	209.6	634.7	2008	473.5		
La	23	51.2	52.8	118.9	26.5		
Ce	36	86.2	87.4	238	47.4		
Pr	6.6	24.7	4.9	33.5	< 5.0		
Nd	18.5	34.7	23.6	115.6	13.7		
Hf	< 2.0	4.5	4.5	1.4	< 2.0		
Ta	2.5	7.1	2.3	< 2.0	< 2.0		
Tl	9	10.2	7.6	< 0.7	2		
Pb	74.4	16.6	43.5	26.8	12.2		
Bi	2.6	3.3	1.4	< 0.5	< 0.5		
Th	12.4	28.9	36.4	22.4	11.6		
U	< 0.5	< 0.5	< 0.5	0.6	< 0.5		

Table 5.2 Minor element data for five of the seven representative rock samples. Two samples (DR1-40 and DR1-41) were prepared after the GAU XRF instrument broke down.

Total Alkali vs. Silica Plots

Samples DR1-40 and DR1-41 did not have minor trace elements determined due to time constraints associate with XRF instrument problems. A plot of total alkalis (Na_2O + K_2O) vs. silica (SiO_2) (TAS plot) shows five out of the seven samples have low total alkali contents, and do not plot within standard TAS diagram fields (Fig. 5.1 a,b), consistent with element mobility and loss of alkalis. As such, only the following immobile trace elements were used for analysis: Sc, Y, Th, Zr, Hf, Ti, Nb, Ta, P, Co, Ni, V and Cr (Rollinson, 1993). Garnet granite gneiss and intermediate gneiss samples DR1-38 and DR1-34 have higher total alkali contents, plotting as granite (Fig. 5.1 a,b.)

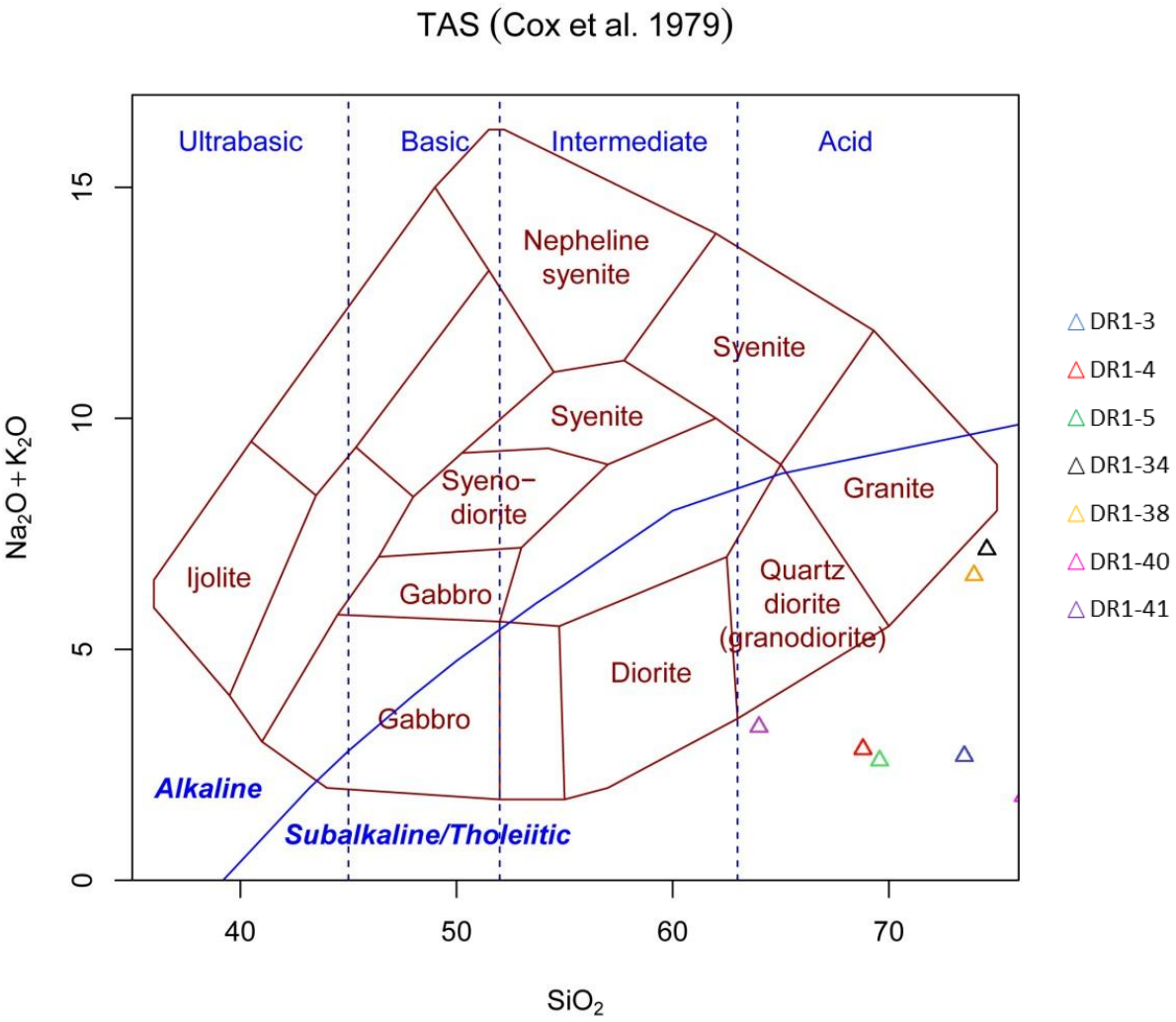

Fig. 5.1 a) Total alkali vs. silica (TAS) diagram as per Cox *et al.*, 1979.

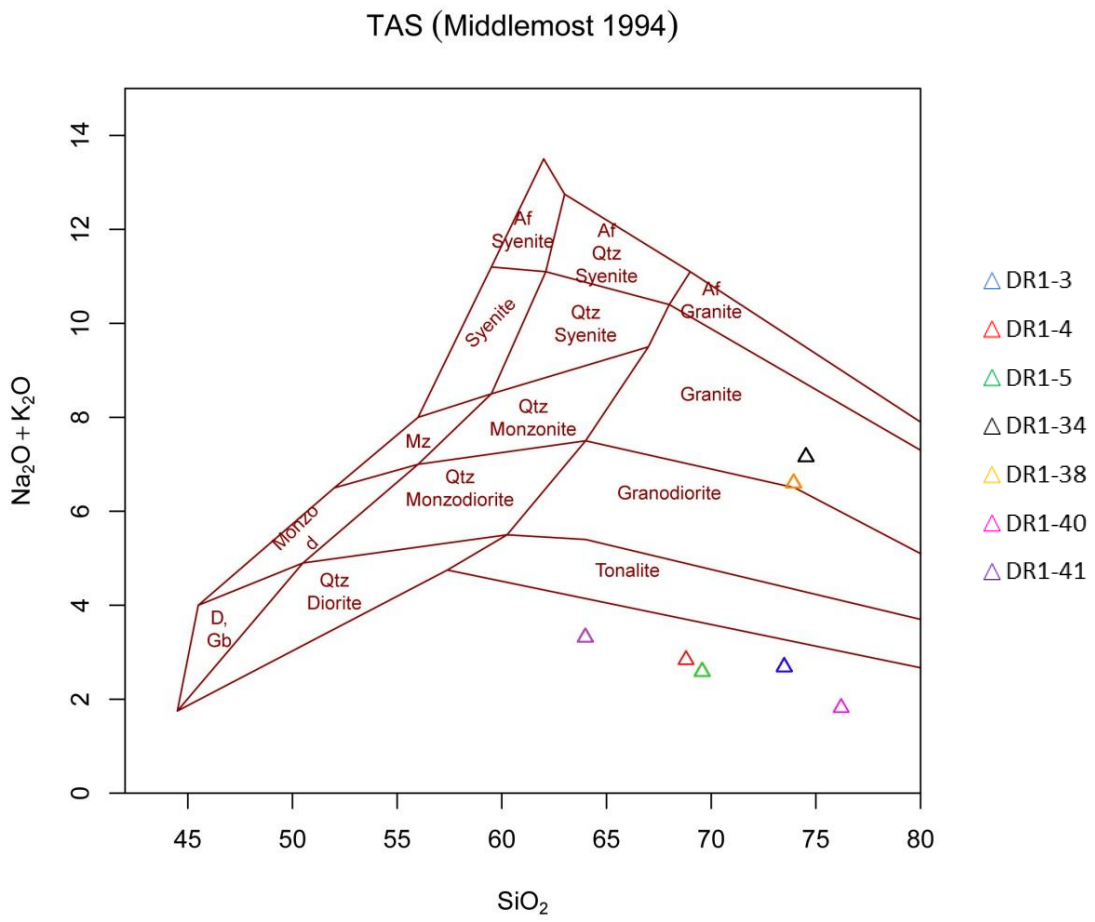

Fig. 5.1 b). Total alkali vs. silica (TAS) diagram as per Middlemost, 1994.

Granite discrimination diagrams

Using the immobile elements Rb, Y and Nd from the samples that had minor trace elements determined (DR1-3, DR1-4, DR1-5, DR1-38), these samples have been shown to plot as syn-collisional granites and volcanic arc granites (Fig. 5.2a, b). Intermediate gneiss sample DR1-34 plots as within-plate granite (Fig. 5.2a,b).

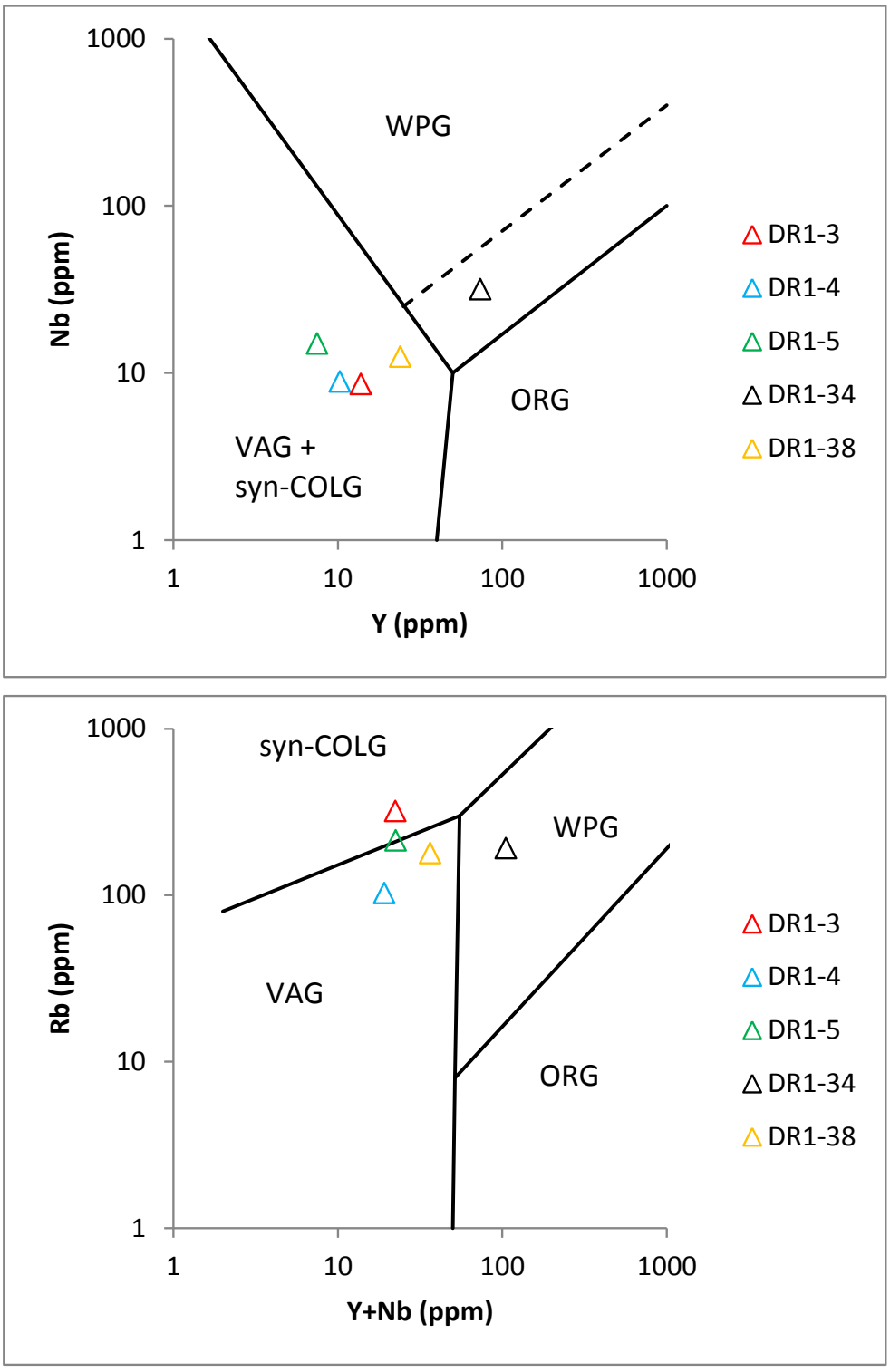

Fig. 5.2 a) Nb-Y discrimination diagram for granites after Pearce *et al.*, 1984, showing the fields of volcanic-arc granites (VAG), syn-collisional granites (syn-COLG), within plate granites (WPG) and ocean ridge granites (ORG). The broken line is the field boundary for ORG from anomalous ridges. **b)** Rb-(Y+Nb) discrimination diagram for granites showing VAG, syn-COLG, WPG and ORG as described above.

Aluminium Saturation Index

The ASI (Aluminium Saturation Index) of all samples is >1.1 (Table 5.3).

Sample	ASI
DR1-3	2.39*
DR1-4	3.98*
DR1-5	4.35*
DR1-34	1.88
DR1-38	1.86
DR1-40	2.97*
DR1-41	2.62*

Table 5.3. ASI of samples, calculated as $Al_2O_3/(K_2O+Na_2O+CaO)$. * High values possibly due to alkali loss during alteration (see Discussion).

CIPW normative calculations

CIPW normative calculations were performed on all seven samples (Table 5.4). Due to the known quantity of Fe_2O_3 and the unknown quantity of FeO, the approach of Ivine & Baragar, 1971 was adopted in determining a ratio. All samples contain normative quartz, plagioclase, orthoclase, corundum, ilmenite, apatite and Na_2SO_4. Hypersthene is calculated in sample DR1-3, DR1-4, DR1-5, DR1-38 and DR1-41. Magnetite is calculated in all samples except for DR1-38 and DR1-40. The normative minerals rutile, magnetite, zircon and chromite were found in some samples, in small concentrations (<0.44 wt.%) (Table 5.4). The other minerals included in normative calculations: nepheline, leucite, kalsilite, diopside, wollastonite, olivine, larnite, acmite, K_2SiO_3, perovskite, sphene, pyrite, halite, fluorite, anhydrite, calcite, Na_2CO_3 were not calculated in any of the samples, and thus were not included here.

Normative Wt. %	DR1-3	DR1-4	DR1-5	DR1-34	DR1-38	DR1-40	DR1-41
Quartz	44.06	57.68	53.61	41.60	44.19	63.13	39.19
Plagioclase	16.43	3.83	4.56	20.76	13.04	18.59	18.68
Orthoclase	12.51	15.26	14.32	29.05	33.69	4.02	13.00
Corundum	5.01	9.68	10.54	4.60	4.96	5.42	7.17
Hypersthene	14.67	7.48	8.04	0	0.50	0	10.93
Rutile	0	0	0	0	0.22	0.58	0
Ilmenite	1.01	1.08	1.12	0.76	0.02	0.06	2.70
Magnetite	3.22	3.18	3.25	2.16	0	0	4.23
Hematite	0	0	0	0.49	1.46	7.22	0
Apatite	0.44	0.28	0.28	0.39	0.35	0.32	0.72
Zircon	0.01	0.01	0.06	0.09	0.04	0	0
Chromite	0	0	0.01	0	0.03	0	0
Na_2SO_4	0.09	0.05	0.07	0.05	0.04	0.02	0.09
Total	97.45	98.53	95.86	99.95	98.54	99.36	96.71

Table 5.4. Normative calculation for samples, using the method of Kurt Hollocher. Ratio of Fe_2O_3/FeO was determined using method of Irvine & Baragar, 1971.

Haker diagrams

Haker diagrams show no correlations between the seven samples, and thus representative diagrams can be seen in Fig. 5.3a-h.

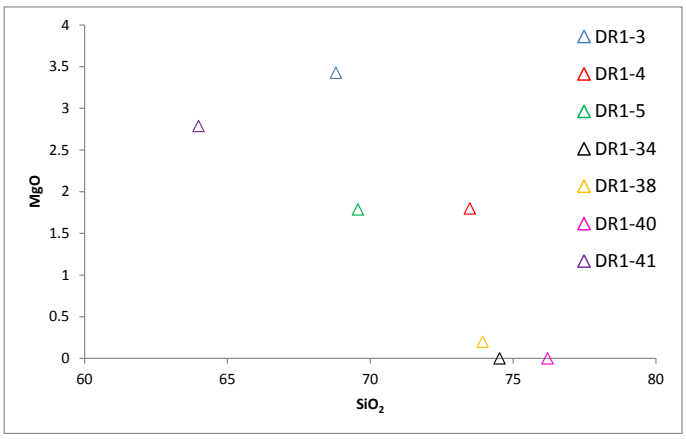

A

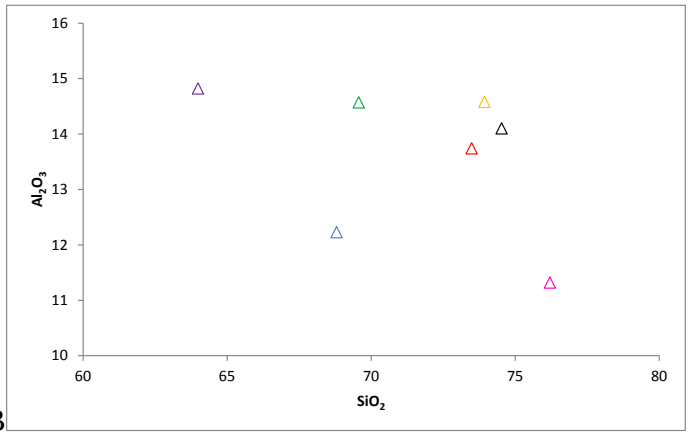

B

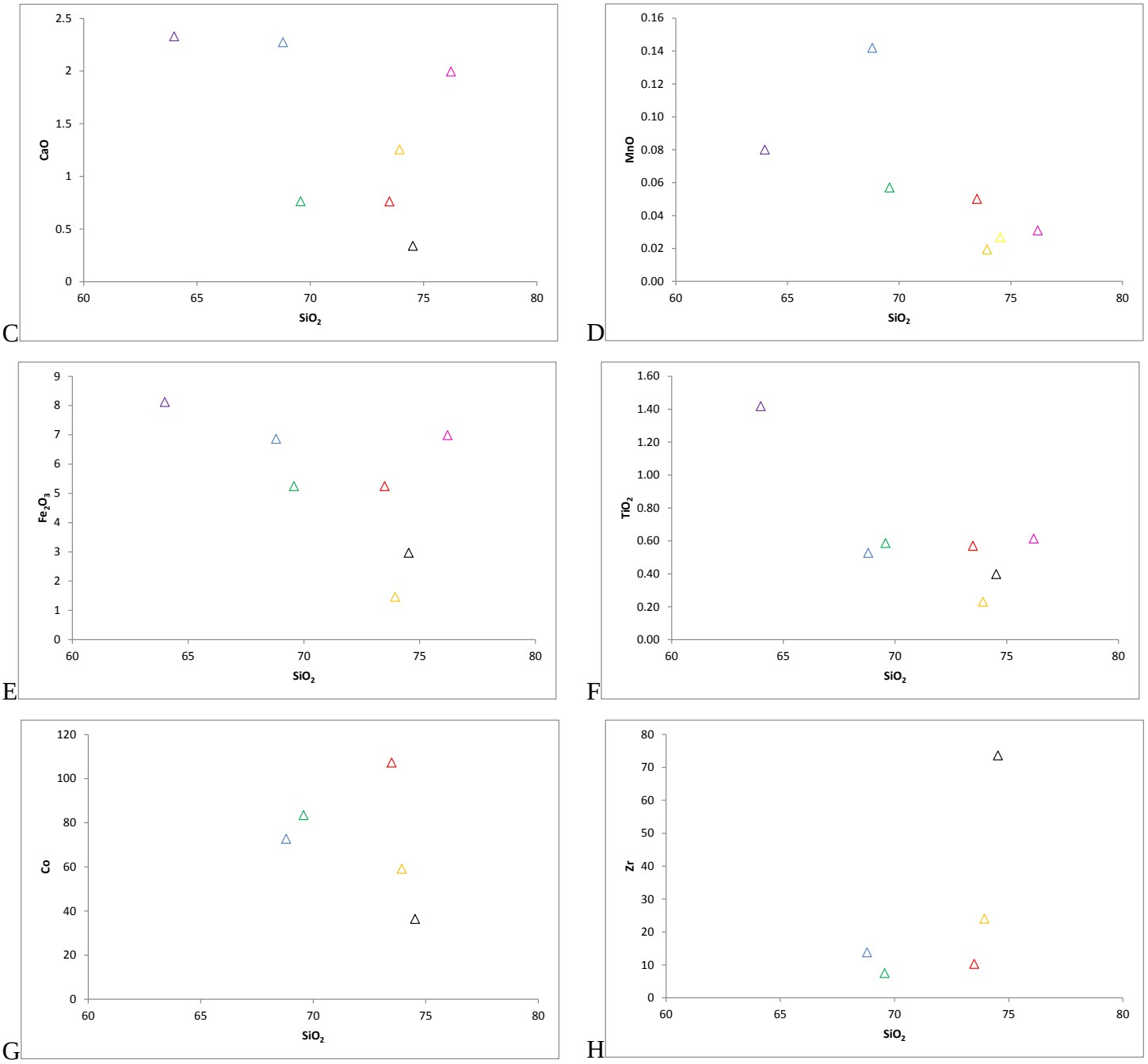

Fig. 5.3. Haker diagrams showing various weight percent oxides (a-f) vs. SiO_2 and various minor elements (g-h) vs. SiO_2. Key presented in a). All data points plotted are above detection limits, except DR1-34 and DR1-40 in a). No correlation between samples can be made.

Chapter 6 – Mineral Geochemistry by Electron Microprobe

6.1 Introduction

Mineral spot analysis by electron microprobe (EMP) enables the quantitative analysis of major and minor elements. These data are useful for comparison of mineral chemistry within and between samples as well as characterising zoning, or lack thereof in minerals. This method is applied to the seven representative rock samples from Batavia Knoll to gain insight into the relationships between samples and to understand the processes which have formed and affected these rocks. This is of importance due to the unconstrained spatial relationships between the rocks due to submergence under 2km of water. Raw data is presented in Appendix C.

6.2 Results

6.2.1 Feldspar

Feldspars were analysed from all seven samples with plagioclase found in all samples (Table 6.1a, Fig. 6.1a-c), and K-feldspar found in DR1-3, DR1-4, DR1-5 and DR1-34 (Table 6.1b, Fig. 6.1a-c). Feldspar data were calculated for three end members as follows (based on 8 oxygen per formula unit; Ca, Na and K are cations per unit formula):

$$XAn = Ca / (Ca+Na+K) *100$$
$$XOr = K / (Ca+Na+K) *100$$
$$XAb = Na / (Ca+Na+K) *100$$

In this study, the general formula for feldspar mineral chemistry will be $An_aOr_bAb_c$, where $_{a, b}$ and $_c$ represent end member percentages as calculated above. Stoichiometry was checked based on typical feldspar equations of Al+Si = 4 cations and Na+Ca+K = 1 cation (on the basis of 8 oxygen per formula unit), and analyses that deviated by more than 5% from the stoichiometry were rejected (n=10) (Appendix C).

A) Granite and Granite Gneiss Samples

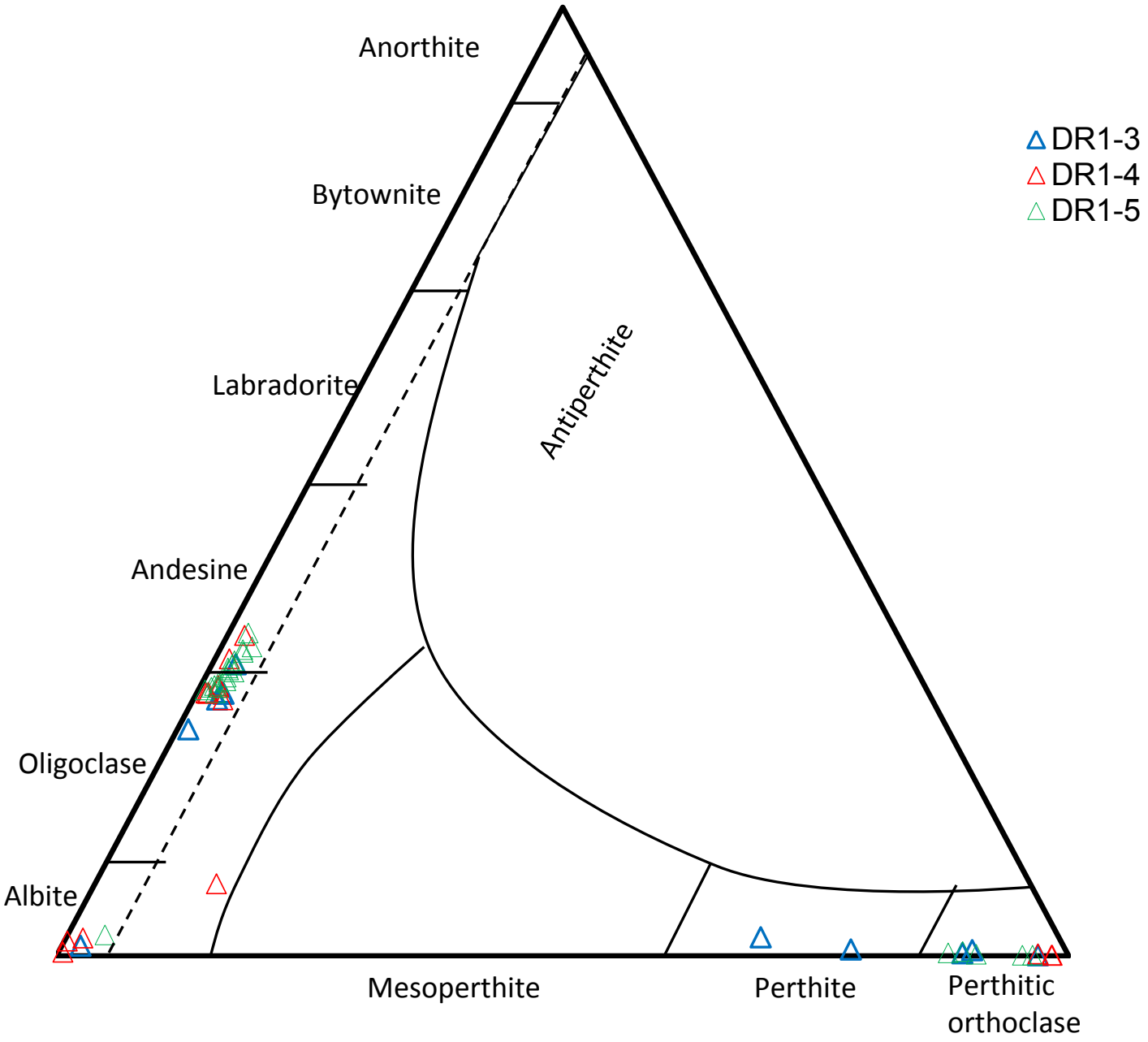

B) Garnet Granite Gneiss Group A Samples

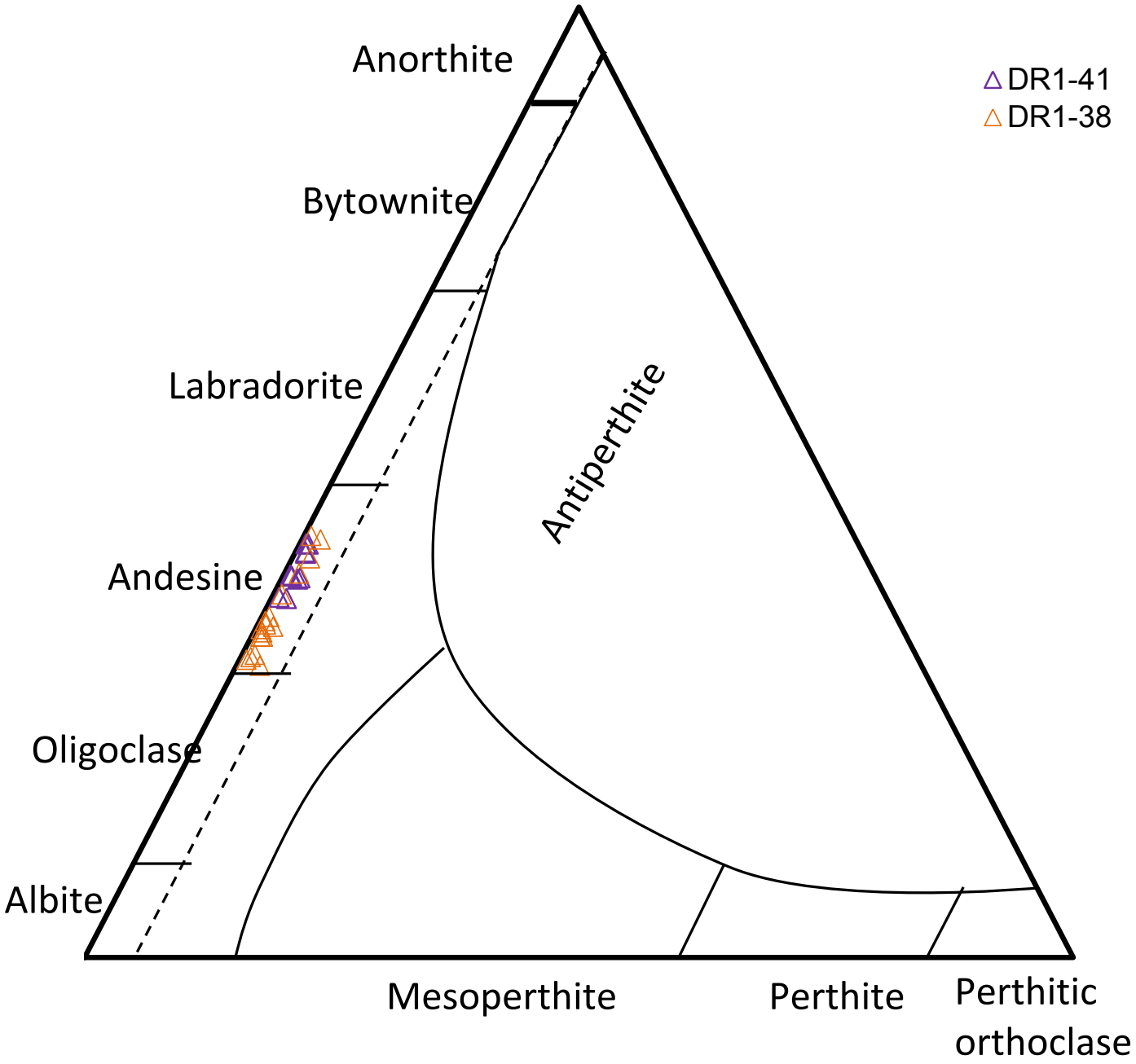

C) Garnet Granite Gneiss and Intermediate Gneiss Samples

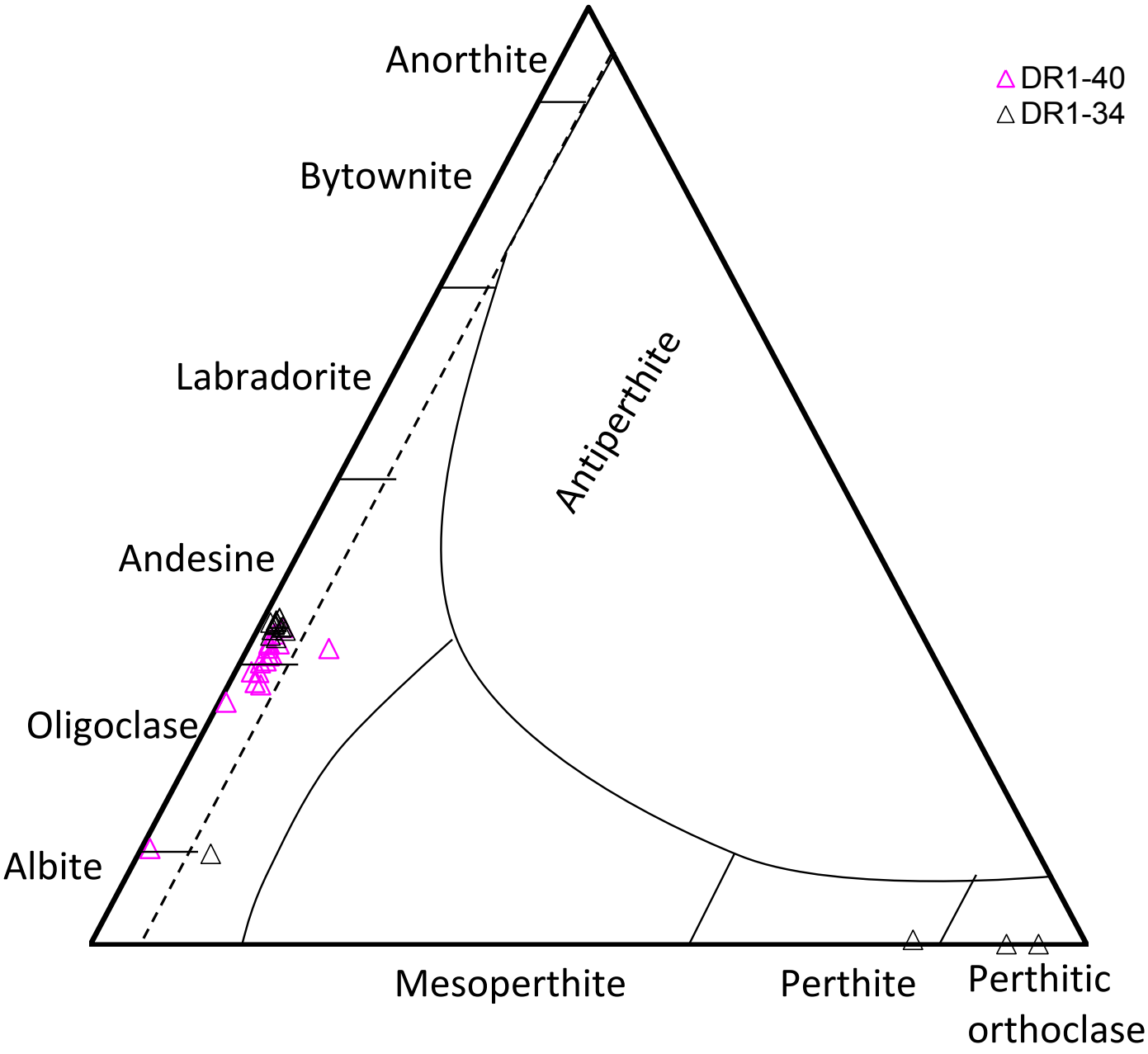

Fig. 6.1 Feldspar ternary diagrams (Deer *et al.*, 2007, p.393). a) Granite and Granite Gneiss samples DR1-3, DR1-4 and DR1-5. b) Garnet Granite Gneiss Group A samples DR1-38 and DR1-41. c) Intermediate Gneiss and Garnet Granite Gneiss group B samples DR1-34 and DR1-40. ±1sd error is represented by the size of the data symbols.

Granite and Granite Gneiss samples

Granite and granite gneiss samples DR1-3, DR1-4 and DR1-5 exhibit similar feldspar compositions, with three main groups: group A ranging from andesine → oligoclase, group B as albite and group C as perthitic orthoclase (Fig. 6.1a). The compositional variation outside analytical error is not a function of core/rim or spatial relationship analyses.

Granite sample DR1-3 group A grains have end member percentages of $An_{31-24,}$ $Or_{3-1,}$ Ab_{75-67} (Fig. 6.1a). One grain is albite (group B) and was analysed from a K-feldspar core. Group C grains range from perthite → perthitic orthoclase with end member percentages of $An_{2-0,}$ $Or_{97-69,}$ Ab_{29-3}.

Granite sample DR1-4 in thin section and hand sample comprises a schist layer and a granite layer (Chapter 4). Group A grains originate from the schist and granite layers and have end member percentages of $An_{34-27,}$ $Or_{2-0,}$ Ab_{72-65} (Fig. 6.1a). Group B and C grains originate from the granite layer, group C end member percentage of An_0 $Or_{98-97,}$ Ab_{3-2}.

Granite gneiss sample DR1-5 group A grains have end member percentages of $An_{34-28}Or_{2-0,}$ Ab_{72-65} (Fig. 6.1a). One group B grain, albite, was analysed from the core of a K-feldspar grain. Group C grains have end member percentages of An_0 $Or_{96-88,}$ Ab_{12-4}.

Garnet Granite Gneiss Group A samples

Garnet granite gneiss group A samples (DR1-38 and DR1-41) have similar feldspar composition of andesine (Fig. 6.1c).

Sample DR1-38 grains spread throughout the whole andesine section with end member percentages of $An_{45-31}Or_{1-0,}$ Ab_{68-55}, and exhibit slight variation outside ±1sd error. This variation is not related to core/rim or spatial relationship analyses.

Sample DR1-41 grains form more of a cluster than DR1-38 with end member percentages of $An_{44-38}Or_{1-0,}$ Ab_{62-56} (Fig. 6.1b).

Garnet Granite Gneiss Group B sample

Garnet granite gneiss group B sample DR1-40 has similar composition to DR1-3, DR1-4 and DR1-5, with the majority of grains ranging from andesine→ oligoclase (Fig. 6.1c). The main cluster of grains have end member percentages of $An_{34-26}Or_{4-0,}$ Ab_{74-63}. The one albite analysis was taken from the core of a K-feldspar grain (Fig. 6.1c).

Intermediate Gneiss sample

Intermediate gneiss sample DR1-34 comprises three groups: group A is a tight cluster of andesine with end member percentages of $An_{35-33}Or_{1-0,}$ Ab_{66-64} (Fig. 6.1b). Group B is one outlier on the boundary of oligoclase and albite. Group C ranges from Perthitic orthoclase → Perthite with end member percentages of $An_0Or_{95-82,}$ Ab_{17-5}. Group B and C were analysed from the leucocratic vein identified in thin section (Chapter 4), while group A grains were analysed from the main groundmass.

6.2.2 Garnet

Garnet cores, rims and traverses were analysed from all three garnet granite gneiss samples; DR1-38, DR1-40 and DR1-41 (Table. 6.2). The minimal Cr cations and the range of Al cations (based on 12 oxygen per formula unit) from 1.90-2.06 indicates that there is minimal Fe_2O_3 (Appendix C). As such, four end members were calculated (based on 12 oxygen per formula unit: Mg, Fe, Mn and Ca represent cations per formula unit):

Pyrope = XPrp = Mg / (Mg+Fe+Mn+Ca) *100
Almandine = XAlm = Fe / (Mg+Fe+Mn+Ca) *100
Spessartine = XSps = Mn / (Mg+Fe+Mn+Ca) *100
Grossular = XGrs = Ca / (Mg+Fe+Mn+Ca) *100

For the purpose of this study, the general formula for garnet mineral chemistry $Prp_aAlm_bSps_cGrs_d$ is presented; $_a$, $_b$, $_c$ and $_d$ representing the end members as calculated above.

Garnet Granite Gneiss Group A

Garnet grains in samples DR1-38 and DR1-41 are zoned. End member percentages are DR1-38 ($Prp_{17-5}Alm_{67-66}Sps_{26-15}Grs_{7-4}$), DR1-41 ($Prp_{16-12}Alm_{71-69}Sps_{27-12}Grs_{12-6}$) (Fig.6.3, Fig.6.4).

The cores of garnet grains exhibit higher concentrations of Almandine (DR1-38 core = 64.9±1.7, rim = 61.1±1.4) and Pyrope (DR1-38 core = 14.9±1.8, rim = 11.4±2.2) and lower concentrations of Spessartine (DR1-38 core = 14.7±1.2, rim = 21.1±3.6) compared to the rim (Fig. 6.3, Fig.6.4). Grossular (DR1-38 core = 5.4±1, rim = 6.3±0.8) shows no zonation outside error between core and rim. The cores in both samples are unzoned, with narrow rims (up to 50µm).

Samples DR1-38 and DR1-41 show similar positive linear correlations in XFe vs Spessartine (Fig. 6.5) with R^2 values of 0.918 and 0.9225 respectively.

Garnet Granite Gneiss Group B

Garnet grains in sample DR1-40 are not zoned outside error ($Prp_{13-9}Alm_{88-83}Sps_{5-4}Grs_{8-4}$). Compared to DR1-38 and DR1-41, this sample has a much higher Almandine content (DR1-40 = 83.6±1) and much lower Spessartine (3.7±0.7), Pyrope (8.7±2.0) and Grossular (4.5±1.5) contents (Fig. 6.2, Fig. 6.3, Fig. 6.4).

DR1-40 shows a short, negative trend in XFe vs Spessartine (Fig 6.5) with a low R^2 value of 0.4972.

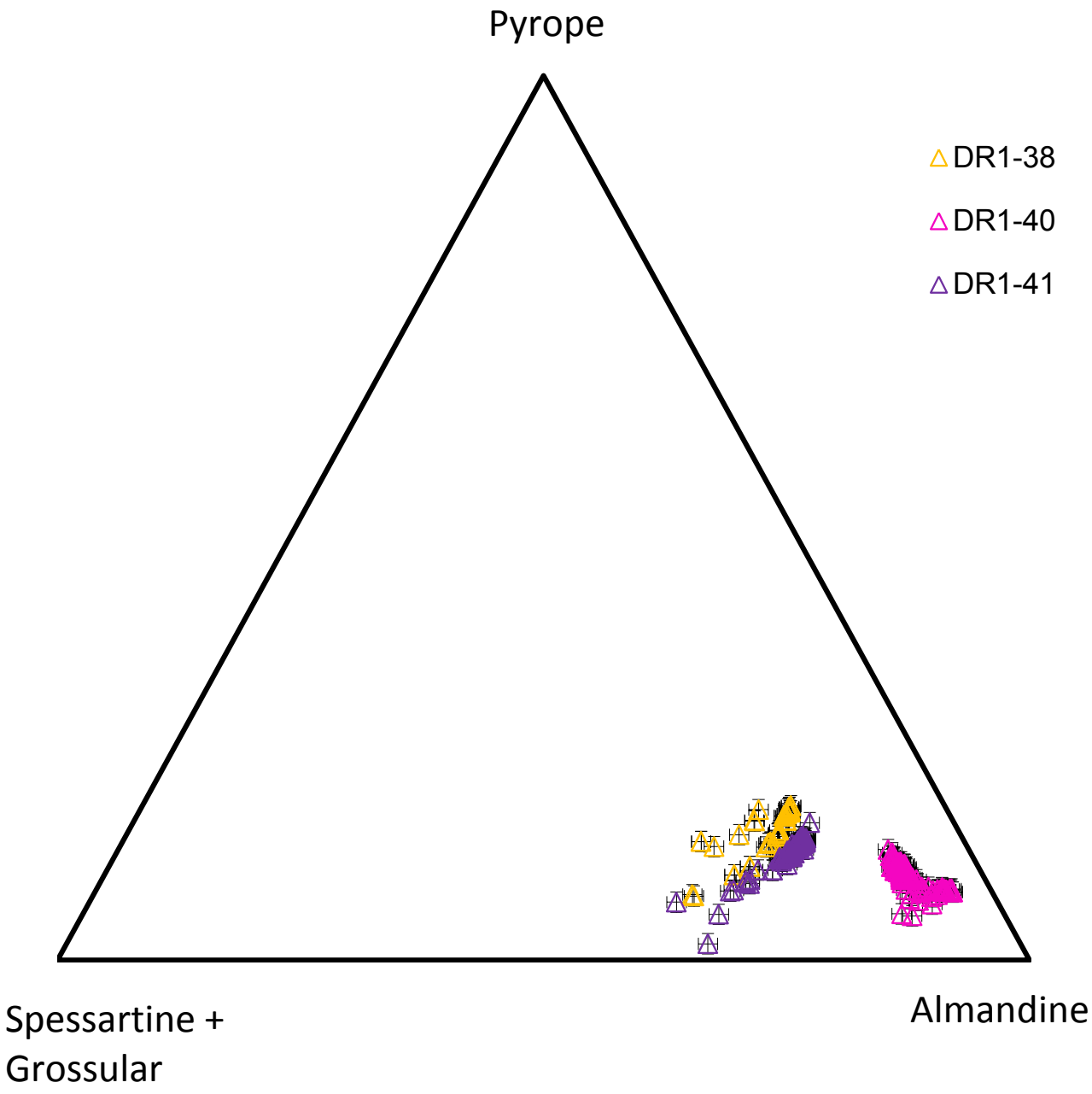

Fig. 6.2. Ternary Plot of Garnet End Member percent for DR1-38, DR1-40 and DR1-41. Error bars represent ±1sd.

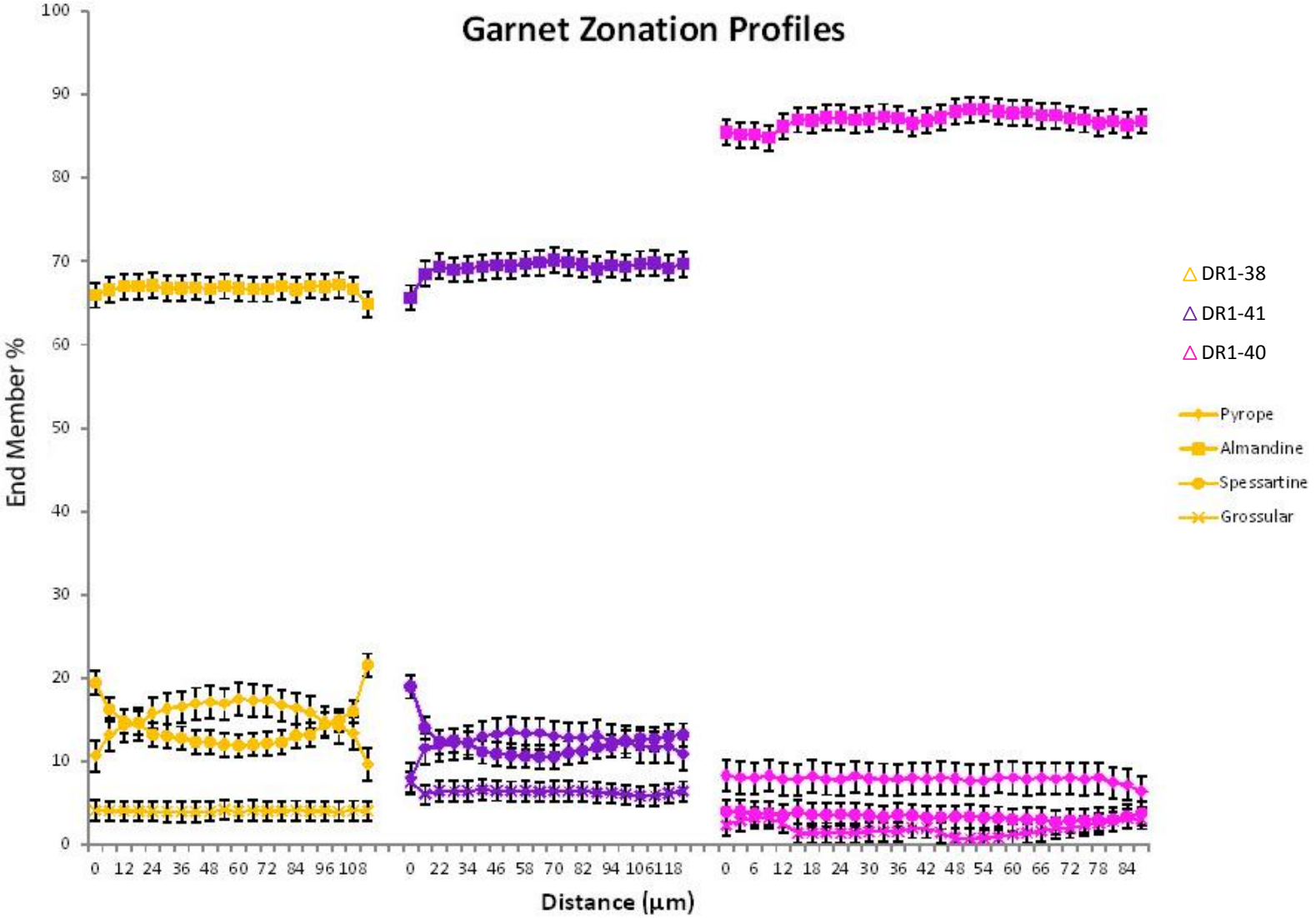

Fig. 6.3. Garnet zonation profiles of individual grains in garnet granite gneiss samples DR1-38, DR1-40 and DR1-41. Of note are the similar profiles of DR1-38 and DR1-41. Sample DR1-40 shows no significant zonation. Error bars represent ±1 standard deviation.

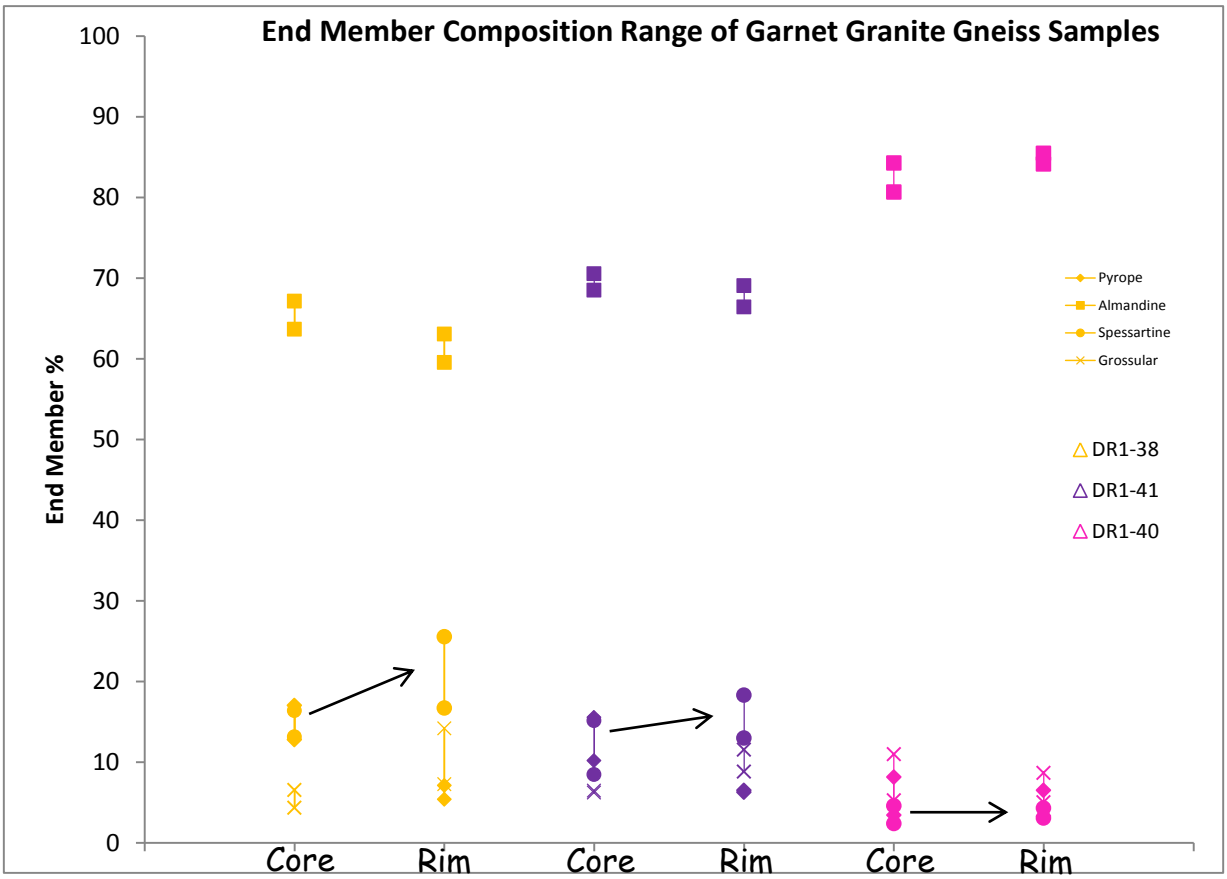

Fig. 6.4. End member composition range of garnet bearing gneisses. Of note is the increase in spessartine (Mn) from core to rim in both DR1-38 and DR1-41 (shown by the black arrow).

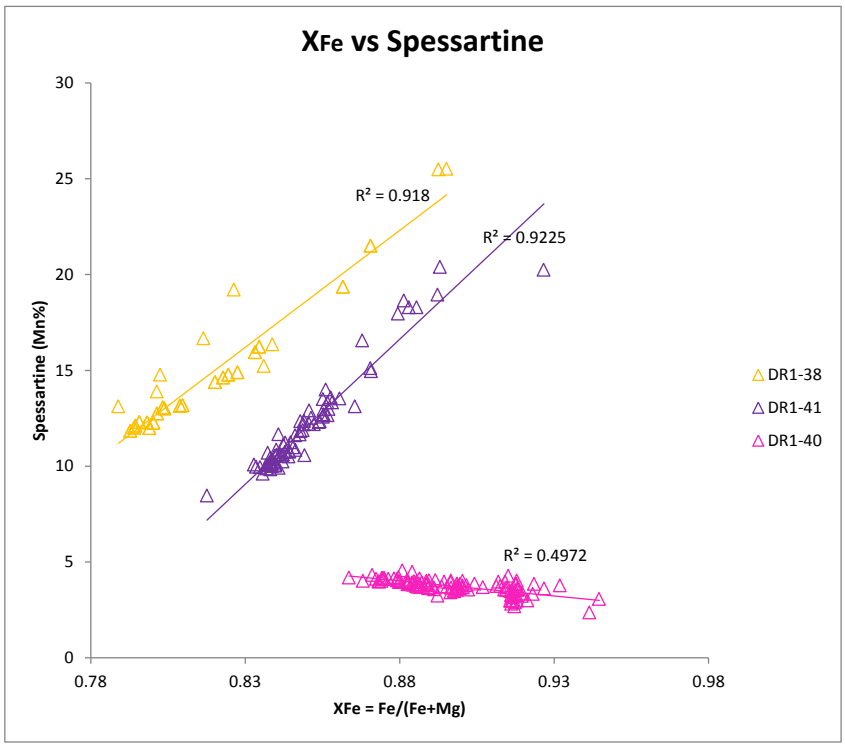

Fig. 6.5. XFe vs. Spessartine for all garnet analyses. The slope of the line represents the degree of retrograde resorption; steeper longer slopes represent a higher degree of resorption, while clusters and short arrays indicate minimal resorption (Spear, 1993).

6.2.3 Amphibole

Amphibole was analysed from the intermediate gneiss, DR1-34, and was classified as per Leake *et al.* (2004) with the standard formula $A_{0-1}\ B_2\ C_5\ T_8O_{22}(OH)_2$. There are five groups as per this classification:

1. Mg-Fe-Mn-Li amphibole
2. Calcic amphibole
3. Sodic-calcic amphibole
4. Sodic amphibole
5. Na-Ca-Mg-Fe-Mn-Li amphiboles

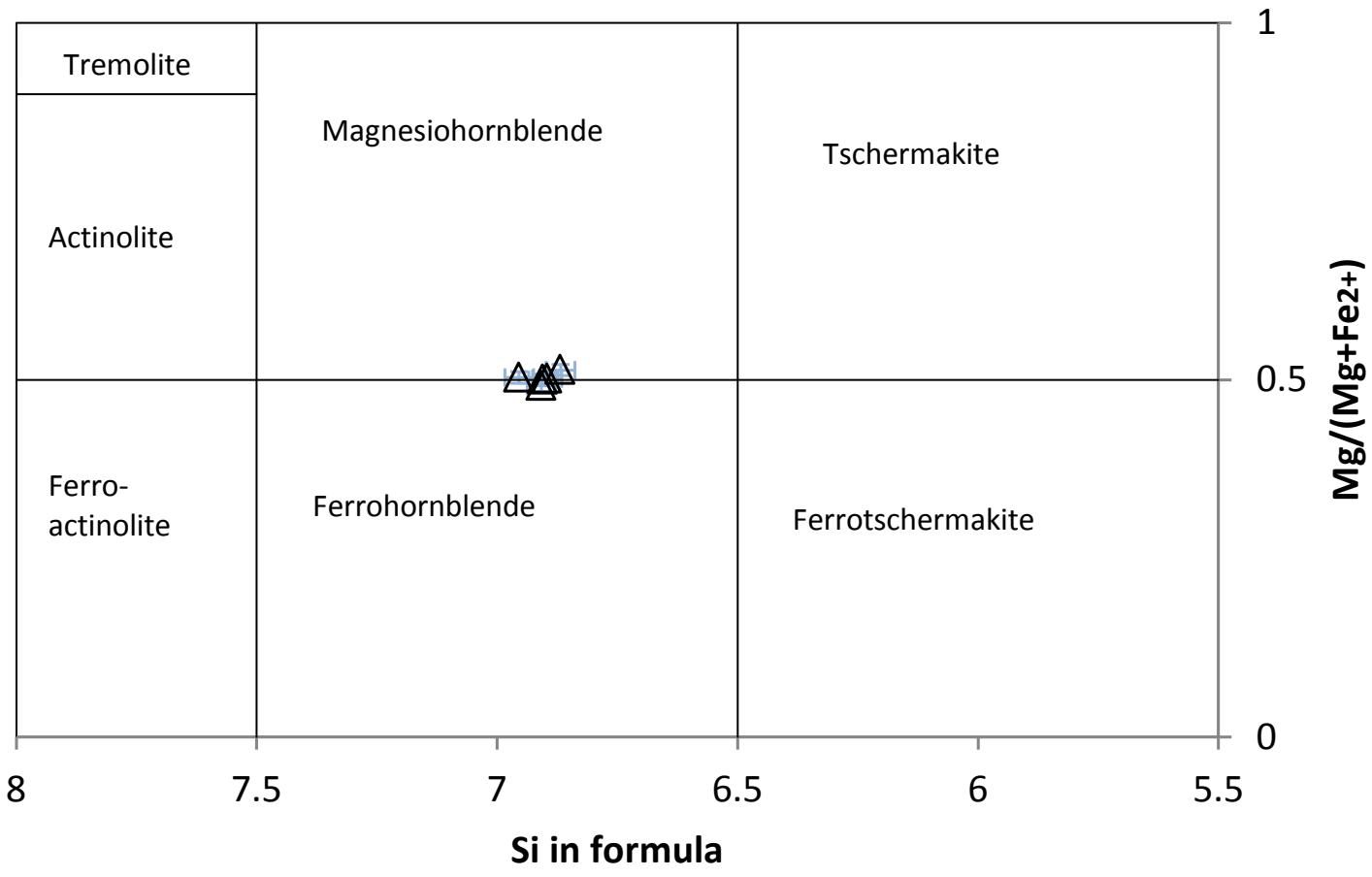

Fig. 6.6. Amphibole classification of intermediate gneiss DR1-34, showing one cluster of data on the boundary between Ferrohornblende and Magnesiohornblende. Error bars (blue) represent ±1sd.

In all analyses, $Ca_B > 1.5$, $Na+K_A > 0.5$ and $Ca_A < 0.5$ (on the basis of 23 oxygen per formula unit), and thus the calcic amphibole diagram was used (Leake *et al.*, 2004). All five analyses fall within one cluster on the boundary between ferro-hornblende and magnesio-hornblende (Fig. 6.6, Table 6.3).

6.2.4 Pyroxene

Pyroxene was found and analysed from two samples: intermediate gneiss DR-34 and garnet granite gneiss DR1-38, and was classified using the technique of Morimoto *et al.*, (1988). The general formula for pyroxene is given as: $M2M1T_2O_{6,}$ based on 6 oxygen per formula unit. For a more detailed description of methods see Morimoto *et al.*, 1988.

Clinopyroxene is found in both samples, plotting as Diopside (DR1-34) and Ferrosilite (DR1-38) (Fig. 6.7, Table 6.4). Both samples form clusters and there is no compositional zonation outside ±1sd error.

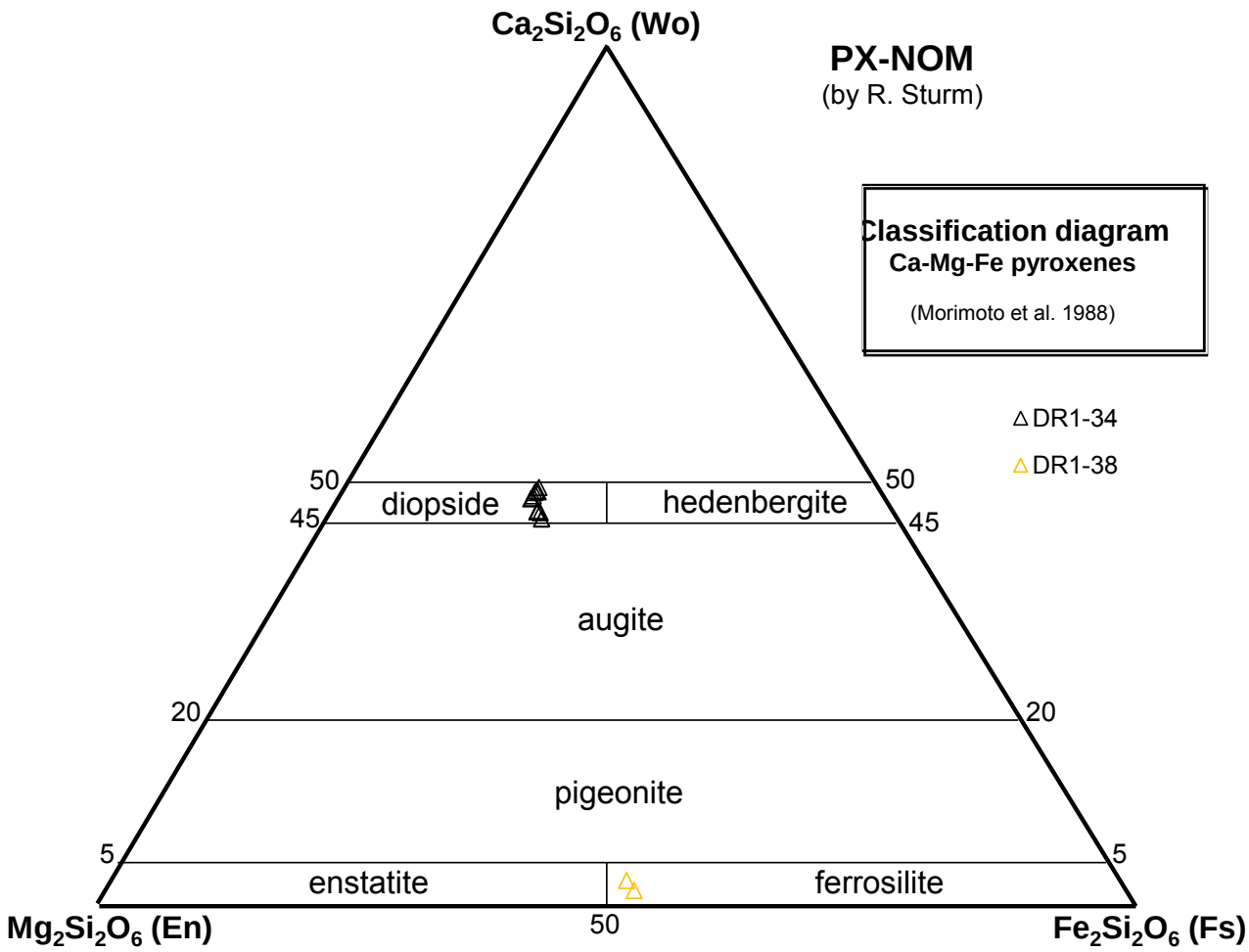

Fig. 6.7. Ca-Mg-Fe Pyroxene classification diagram (Morimoto *et al.*, 1988) for intermediate gneiss sample DR1-34 and garnet granite gneiss sample DR1-38.

6.2.5 Biotite

Biotite was analysed from all seven samples, and was classified using the following formula (based on 22 oxygen) (Table 6.5):

$$K_2(Mg, Fe^{2+})_{6-4}(Fe^{3+}, Al, Ti)_{0-2}(Si_{6-5}\ Al_{2-3}\ O_{20})\ (OH, F)_4$$

There are several important characteristics of biotite including K_2O, total Ti cations, the ratio of Mg an Fe^{2+}, (XFe), calculated as $Fe^{2+}/(Fe^{2+}+Mg)$ and the left over Al in the octahedral site (Al^{V1}). Analyses with K_2O <8% were rejected as low K_2O indicates partial chloritisation due to low grade alteration. Ti cations per formula unit in biotite is a common indicator of temperature and pressure conditions, as Ti content increases with metamorphic grade. Mg and Fe^{2+} substitute for each other

in biotite, causing the ratio (XFe) to vary due to bulk rock composition, mineral assemblage and/or metamorphic grade. A high amount of Al^{V1} in biotite is indicative of high periluminocity.

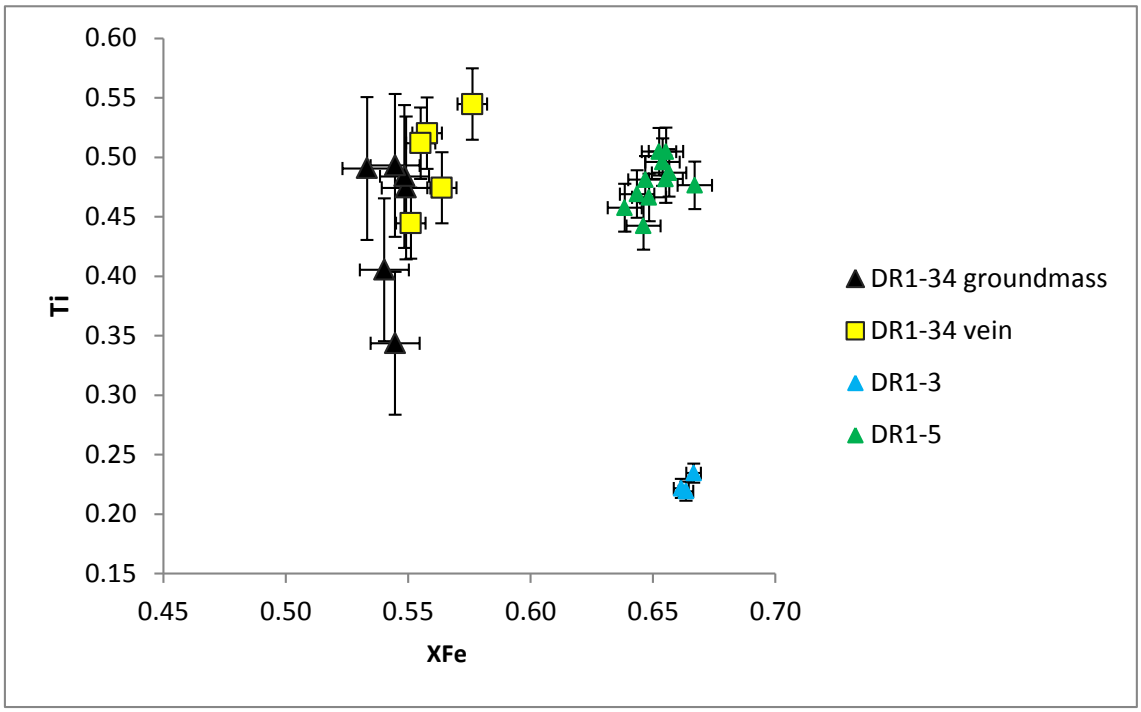

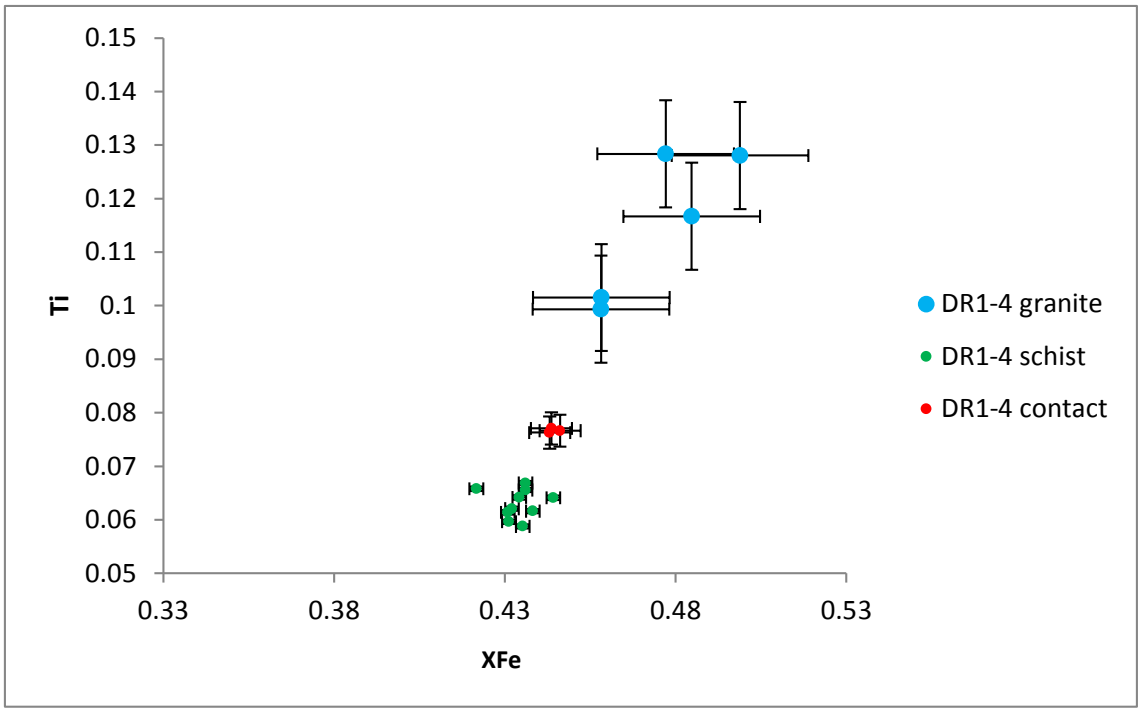

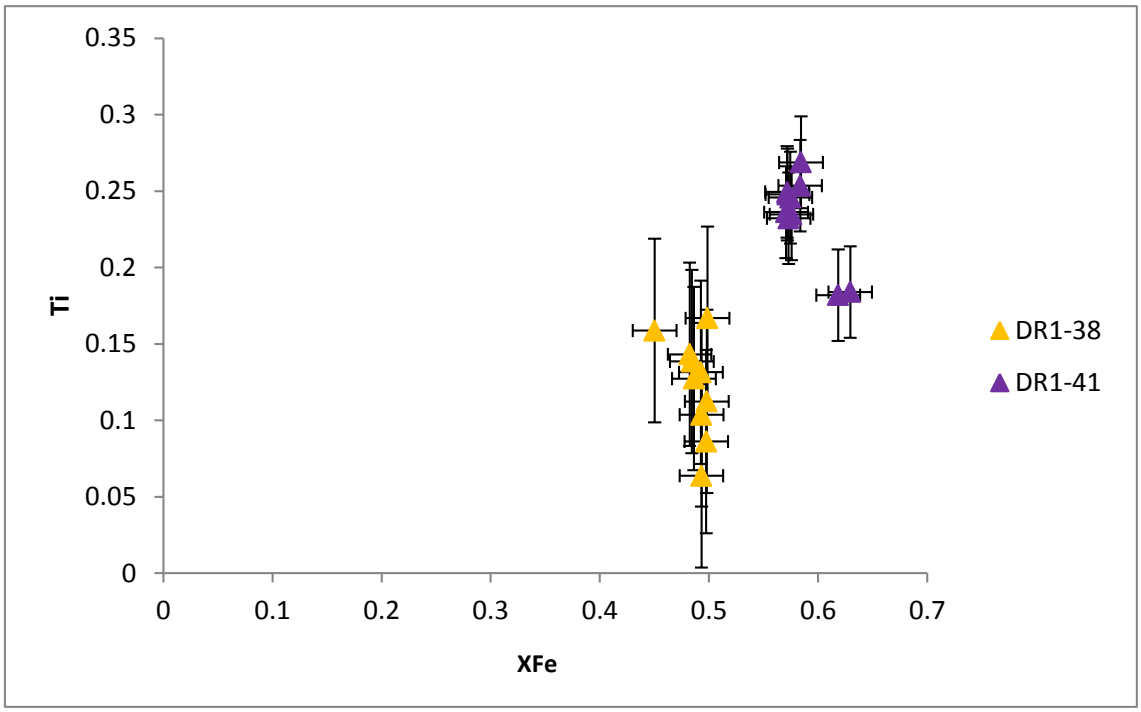

Fig. 6.8. XFe vs. Ti content for **a)** granite DR1-3, granite gneiss DR1-5 and intermediate gneiss DR1-34, **b)** granite DR1-4 and **c)** garnet granite gneiss samples DR1-38 and DR1-41. Error bars represent ±1sd.

Granite and Granite Gneiss

Biotite grains in granite sample DR1-3 and granite gneiss sample DR1-5 do not show any significant variation (outside ±1sd) in Ti, XFe or K_2O values (Table 6.5, Fig. 6.8a). Only five grains of biotite in sample DR1-3 were analysed, and two of these were rejected due to complete or partial chloritisation (K_2O < 8 wt.%). Two out of thirteen were rejected for the same reason in DR1-5. The Al^{V1} is relatively high for these two samples; DR1-3 (0.28±0.03) and DR1-5 (0.29±0.03) (Table 5.5).

Granite sample DR1-4 has three distinct types of biotite which correlate with the schist, granite and schist-granite contact layers documented in thin section and hand sample (Chapter 4). Granite biotite has higher Ti and XFe than the schist biotite (Fig. 6.8b). Biotite from the schist-granite contact has Ti and XFe values between the other two biotites (Fig. 6.8b). Five grains out of twenty-three were rejected due to partial or complete chloritisation; three from schist and one each from contact and granite. The Al^{V1} is relatively high for all three layers, but is highest in the schist (0.46±0.01), lowest in the granite (0.39±0.09) and in between in the contact (0.42±0.01) (Table 6.5).

Intermediate Gneiss

Biotite was analysed from the groundmass of the gneiss and the leucocratic vein. The biotite chemistries from these two layers overlap (Fig. 6.8a). Four grains out of sixteen were rejected due to partial or complete chloritisation; three from the groundmass and one from the vein. The Al^{V1} from this sample is zero (Table 6.5).

Garnet Granite Gneiss

Garnet granite gneiss group A samples (DR1-41 and DR-38) each have one type of biotite (Fig. 6.8c). The variation seen in individual sample XFe and Ti contents is within ±1sd error. DR1-41 overall has a higher Ti and XFe content than DR1-38. Sample DR1-38 had three grains out of fifteen rejected due to partial or complete chloritisation and DR1-41 had thirteen out of twenty-three rejected. The Al^{V1} for DR1-38 is relatively high (0.33±0.14), as is that of DR1-41 (0.18±0.05) (Table 6.5).

Biotite in sample DR1-40 is rare, and only two grains of biotite were analysed. The Al^{V1} is relatively high (0.28±0.09), however has a large standard deviation (Table 6.5).

Plagioclase	DR1-38	1 sd	DR1-3	1 sd	DR1-4	1 sd	DR1-5	1 sd	DR1-34	1 sd	DR1-40	1 sd	DR1-41	1 sd
P_2O5	0.04	0.03	0.02	0.02	0.02	0.03	0.02	0.02	0.01	0.01	0.01	0.01	0.05	0.02
SiO_2	58.06	1.12	60.24	0.72	59.80	0.52	59.59	0.65	58.26	0.48	58.04	3.14	56.47	0.94
TiO_2	BDL		BDL		BDL		BDL		BDL		BDL		BDL	
Al_2O_3	25.86	0.71	24.42	0.35	24.73	0.47	24.83	0.27	25.42	0.27	24.05	1.51	26.35	0.96
Cr_2O_3	BDL		BDL		BDL		BDL		BDL		BDL		BDL	
FeO	0.10	0.07	0.04	0.02	0.11	0.12	0.06	0.03	0.16	0.06	0.11	0.08	0.05	0.02
MnO	BDL		BDL		BDL		BDL		BDL		BDL		BDL	
MgO	BDL		BDL		BDL		BDL		BDL		BDL		BDL	
CaO	7.67	0.86	5.93	0.53	6.28	0.49	6.46	0.36	7.32	0.14	6.43	0.53	8.42	1.25
BaO	BDL		BDL		BDL		BDL		BDL		BDL		BDL	
K_2O	0.21	0.09	0.41	0.11	0.30	0.12	0.36	0.10	0.32	0.10	0.48	0.26	0.23	0.11
Na_2O	7.45	0.58	8.44	0.35	8.32	0.31	8.10	0.35	7.66	0.08	7.85	0.63	7.02	0.45
Total	99.39		99.50		99.58		99.42		99.14		96.98		98.59	
An	0.36	0.04	0.27	0.02	0.29	0.02	0.30	0.02	0.34	0.01	0.30	0.02	0.39	0.05
Or	0.01	0.01	0.02	0.01	0.02	0.01	0.02	0.01	0.02	0.01	0.03	0.02	0.01	0.01
Ab	0.63	0.04	0.70	0.03	0.69	0.02	0.68	0.02	0.64	0.01	0.67	0.03	0.59	0.05

Table 6.1 a). Averages, standard deviations and end member percentages for plagioclase feldspar determined by EMP for each sample. BDL = below detection limits. An = Anorthite. Or = Orthoclase. Ab = Albite.

K-Feldspar	DR1-3	1 sd	DR1-4	1 sd	DR1-5	1 sd	DR1-34	1 sd
P_2O_5	0.02	0.01	BDL		0.02	0.02	0.00	0.00
SiO_2	63.38	0.64	63.11	0.64	63.03	0.34	62.75	0.39
TiO_2	BDL		BDL		BDL		BDL	
Al_2O_3	18.74	0.42	19.66	2.53	18.69	0.17	18.57	0.23
Cr_2O_3	BDL		BDL		BDL		BDL	
FeO	0.07	0.11	0.11	0.14	0.05	0.03	0.03	0.03
MnO	BDL		BDL		BDL		BDL	
CaO	0.14	0.15	0.40	0.77	0.03	0.04	0.03	0.05
BaO	BDL		BDL		BDL		BDL	
K_2O	14.53	1.75	12.84	7.17	15.56	0.50	15.04	0.99
Na_2O	1.67	1.22	2.46	4.46	0.88	0.41	1.11	0.72
Total	98.54		98.57		98.25		97.52	
An	0.01	0.01	0.02	0.04	0.00	0.00	0.00	0.00
Or	0.85	0.11	0.76	0.43	0.92	0.04	0.90	0.07
Ab	0.15	0.11	0.22	0.39	0.08	0.04	0.10	0.06

Table 6.1 b) Averages, standard deviations and end member percentages for K-feldspar determined by EMP for samples DR1-3, DR1-4, DR1-5 and DR1-34. BDL = below detection limits. An = Anorthite. Or = Orthoclase. Ab = Albite.

Garnet	DR1-38C	1sd	DR1-38R	1sd	DR1-41C	1sd	DR1-41R	1sd	DR1-40	1sd
P_2O_5	0.02	0.02	0.02	0.02	0.01	0.01	0.02	0.02	0.01	0.01
SiO_2	37.08	0.20	36.85	0.32	36.55	0.31	36.54	0.42	35.21	0.84
TiO_2	BDL		BDL		BDL		BDL		0.03	0.02
Al_2O_3	21.15	0.08	20.91	0.08	21.08	0.06	20.90	0.28	20.59	0.58
Cr_2O_3	BDL		0.04	0.02	BDL		0.04	0.02	BDL	
FeO	30.35	0.66	27.61	1.46	32.11	0.39	31.06	0.59	37.90	1.19
MnO	6.77	0.53	9.43	1.69	5.34	1.14	6.91	1.08	1.67	0.18
MgO	3.90	0.50	2.88	0.79	3.24	0.49	2.69	0.30	2.40	0.39
CaO	1.98	0.37	2.22	0.23	2.29	0.03	2.29	0.05	1.29	0.46
BaO	0.00	0.00	0.00	0.00	0.00	0.00	0.00	0.00	0.01	0.02
K_2O	BDL		0.01	0.01	0.01	0.01	0.01	0.01	BDL	
Na_2O	0.02	0.01	0.02	0.01	0.02	0.01	0.02	0.00	BDL	
Total	101.28		99.99		100.65		100.48		99.13	
Pyrope	0.15	0.02	0.11	0.03	0.13	0.02	0.11	0.01	0.08	0.02
Almandine	0.65	0.02	0.61	0.01	0.69	0.01	0.68	0.01	0.84	0.02
Spessartine	0.15	0.01	0.21	0.04	0.12	0.02	0.14	0.02	0.04	0.01
Grossular	0.05	0.01	0.06	0.01	0.06	0.00	0.06	0.00	0.05	0.01

Table 6.2. Averages and standard deviations for garnet determined by EMP for garnet granite gneiss samples. C = core. R= rim. BDL = below detection limits.

Amphibole	Average	1sd
P_2O_5	0.02	0.02
SiO_2	43.40	1.37
TiO_2	0.82	0.36
Al_2O_3	6.81	1.15
Cr_2O_3	BDL	
FeO	18.51	0.50
MnO	0.37	0.03
MgO	10.30	0.34
CaO	11.97	0.29
BaO	BDL	
K_2O	0.80	0.19
Na_2O	1.01	0.16
Total	94.02	

Table. 6.3. Averages and standard deviations for amphibole from sample DR1-34, determined by EMP. BDL = below detection limits.

Pyroxene	DR1-34	1sd	DR1-38	1sd
SiO2	49.74	0.78	51.63	0.53
Cr2O3	BDL		BDL	
TiO2	0.11	0.08	0.05	0.00
Al2O3	0.80	0.48	1.30	0.51
FeO	11.78	0.49	25.99	0.58
MnO	0.64	0.07	2.59	0.02
MgO	11.40	0.17	14.37	0.01
CaO	22.98	0.76	1.17	0.36
K2O	0.01	0.01	0.02	0.02
Na2O	0.32	0.10	0.24	0.06
Total	97.79		97.35	

Table. 6.4. Averages and standard deviations for pyroxene from sample DR1-34 and DR1-38 determined by EMP. BDL = below detection limits.

Biotite	XFe	Ti	Al^{V1}
DR1-3	0.66	0.23	0.28
1sd	0.00	0.01	0.03
DR1-4 schist	0.43	0.06	0.46
1sd	0.01	0.00	0.01
DR1-4 contact	0.44	0.08	0.42
1sd	0.00	0.00	0.01
DR1-4 granite	0.48	0.11	0.39
1sd	0.02	0.01	0.09
DR1-5	0.65	0.24	0.29
1sd	0.01	0.01	0.03
DR1-34	0.55	0.24	0.00
1sd	0.01	0.03	0.04
DR1-38	0.48	0.10	0.33
1sd	0.02	0.06	0.14
DR1-40	0.75	0.36	0.28
1sd	0.00	0.09	0.10
DR1-41	0.59	0.23	0.18
1sd	0.02	0.03	0.05

Table. 6.5. Averages and standard deviation of XFe (Fe/(Mg+Fe), Ti weight percent and Al left over in the octahedral site of the biotite (Al^{V1}) from each sample.

Chapter 7 – Zircon U-Pb geochronology and Lu-Hf isotopes

7.1 Introduction

Zircon has long been recognised as a useful and robust mineral for the U-Pb dating of rocks. While U-Pb isotope systems can change in response to changed conditions such as increase in heat and pressure, it has now been shown that the initial $^{176/177}$Hf isotope of zircon is decoupled from U-Pb and does not change once it has been incorporated into the crystal lattice of the grain (Halpin *et al*., 2012). Once zircon crystallises from a magma, it is stable up to high metamorphic grades. Due to the very low Lu/Hf in zircon, it can preserve the $^{176/177}$Hf of the host magma at the time of crystallisation. Thus, the link between the age and the isotopic composition of the magma is more likely to be preserved than in whole rock isotopic systems. High values of $^{176/177}$Hf indicate a "juvenile" or mantle derived origin for the magma, while low values indicate the reworking of older crystal material (Belousova, pers. comm. 2012). The combination of U-Pb and Lu-Hf isotope data is thus an invaluable tool for determining the crustal evolution of complex terrains. Halpin *et al.*, (2012) also showed that by using certain criteria, a minimum crystallisation/metamorphism age can be determined for zircon grains which spread along the concordia for tens to hundreds of millions of years. Criteria: grains must be concordant and have consistent Hf isotopic data results. This is important for this study as five out of six samples from Batavia Knoll show significant isotopic disturbance through a spreading along the concordia for tens to hundreds of millions of years.

Intermediate gneiss sample DR1-34 yielded no zircon. As such, the remaining six rock samples (Table 7.1) have undergone U-Pb dating and Lu-Hf isotope analysis with the aim to characterise the geochronological history of each sample, recognise the relationships between each sample and to correlate the data to published data to understand their history/role in relation to super continent cycles, in particular the formation and break-up of Gondwanaland. U-Pb and Lu-Hf data is presented in Appendix D.

7.2 Results

7.2.1 Zircon morphology

Representative cathodoluminescence (CL) images of each sample can be seen in Fig. 7.1a – 7.1f. CL images of all zircons are presented in Appendix E.

DR1-3

One type of zircon is found in sample DR1-3. Grains typically exhibit euhedral, double terminating, fully formed prismatic grains ranging in size from 240x90 – 30x50 µm. Colours range from colourless to pink through brown. Whilst oscillatory zoning is most common, cores and rims as well as rare sector zoning occurs. Luminesce is generally low.

DR1-4

One type of zircon is found in sample DR1-4. Grains range in colour from colourless to light pink and have distinct cores and rims. Rims typically exhibit oscillatory zoning and euhedral crystal edges (prisms) with low luminesce. Cores have high luminesce, typically with oscillatory zoning however in some cases the cores are ghosted. Size ranges from 170x90 – 40x40 µm.

DR1-5

Two forms of zircon are present in sample DR1-5. Group A typically exhibit oscillatory zoning without cores and rims. Size ranges from 200x80 – 40x30 µm and grain shapes are double terminating, euhedral prismatic with a low luminesce. Glomeroporphyritic grains are present. Group B comprises cores and rims with size ranging from 120x80 – 50x30 µm. Both the core and rim of grains are oscillatory zoned; with the core having a much higher luminesce than the duller rims. Resorption along the core-rim boundary is common. Grain shapes are dominantly euhedral with occasional ovoid grains. Cores typically appear to be fragments with a rim overgrowth.

DR1-38

Sample DR1-38 contains two distinct types of zircon. Group A exhibit a long, thin, euhedral crystal habit, ranging in size from 180x30 – 30x40 µm. No cores and rims are present, and sector zoning is common, with moderate luminesce. Colours range from colourless to pink through brown. Group B

ranges in colour from colourless to pink through brown and has distinct cores and rims. Size ranges from 120x60 – 20x40 µm. Cores and rims are oscillatory zoned. There is a relatively bright, uneven luminesce band seen at the boundary between core and rim. The overall crystal shape is euhedral, although some grains are slightly more rounded. Cores typically appear to be fragments with a rim overgrowth.

DR1-40

One group of zircon was identified in this sample ranging from dark orange to pink in colour. Grains are euhedral with defined crystal edges and rare embayments, ranging in size from 280x90 – 80x50 µm. Cores and rims are present in some grains, following the typical oscillatory zoning patterns of all other grains. Luminesce is typically low except in rare cores where it is relatively high.

DR1-41

One group of zircon is present in sample DR1-41, ranging in size from 120x80 – 30x30 µm. Cores and rims are common with oscillatory zoning in the cores and sector zoning on the rims. Typically there is a high luminesce band separating the core and rim, alongside resorption textures. The general shape is subhedral rounded with rare soccer balls.

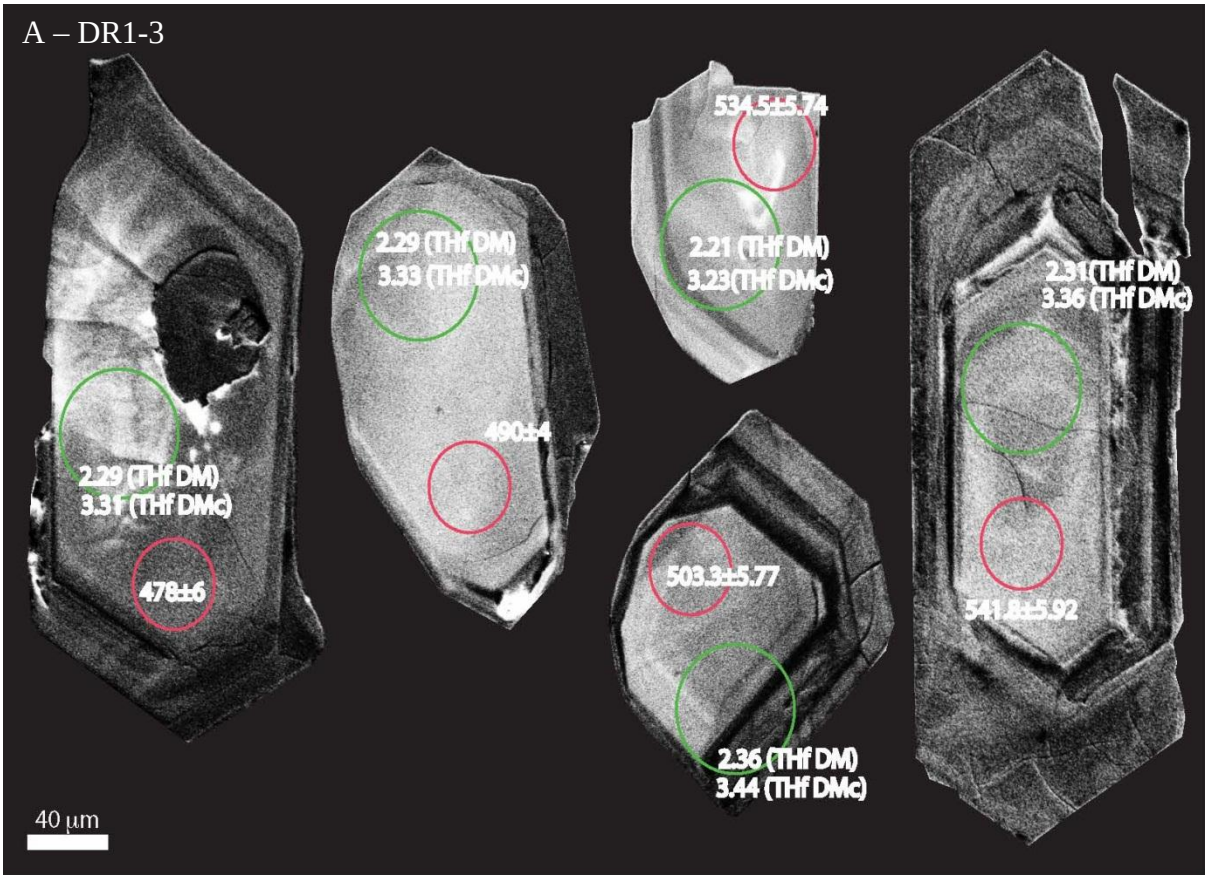
A – DR1-3
534.5±5.74
2.21 (THf DM)
3.23(THf DMc)
2.29 (THf DM)
3.33 (THf DMc)
490±4
2.29 (THf DM)
3.31 (THf DMc)
478±6
503.3±5.77
2.36 (THf DM)
3.44 (THf DMc)
2.31(THf DM)
3.36 (THf DMc)
541.8±5.92
40 μm

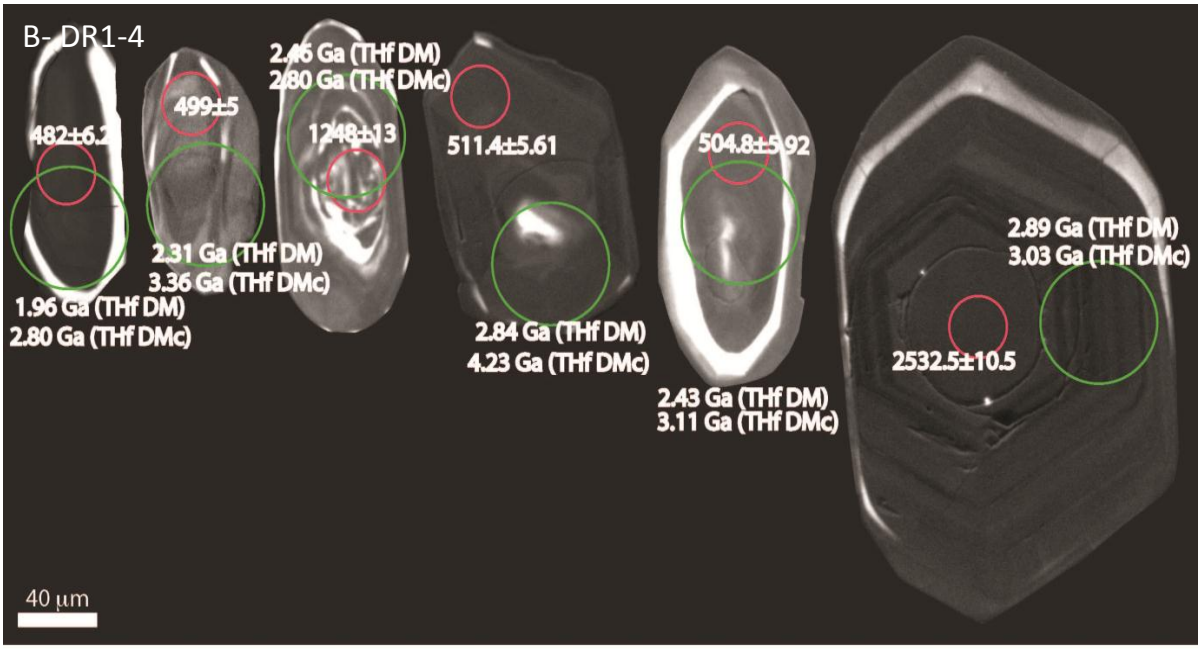
B- DR1-4
2.46 Ga (THf DM)
2.80 Ga (THf DMc)
499±5
482±6.2
1248±13
511.4±5.61
504.8±5.92
2.89 Ga (THf DM)
3.03 Ga (THf DMc)
2.31 Ga (THf DM)
3.36 Ga (THf DMc)
1.96 Ga (THf DM)
2.80 Ga (THf DMc)
2.84 Ga (THf DM)
4.23 Ga (THf DMc)
2532.5±10.5
2.43 Ga (THf DM)
3.11 Ga (THf DMc)
40 μm

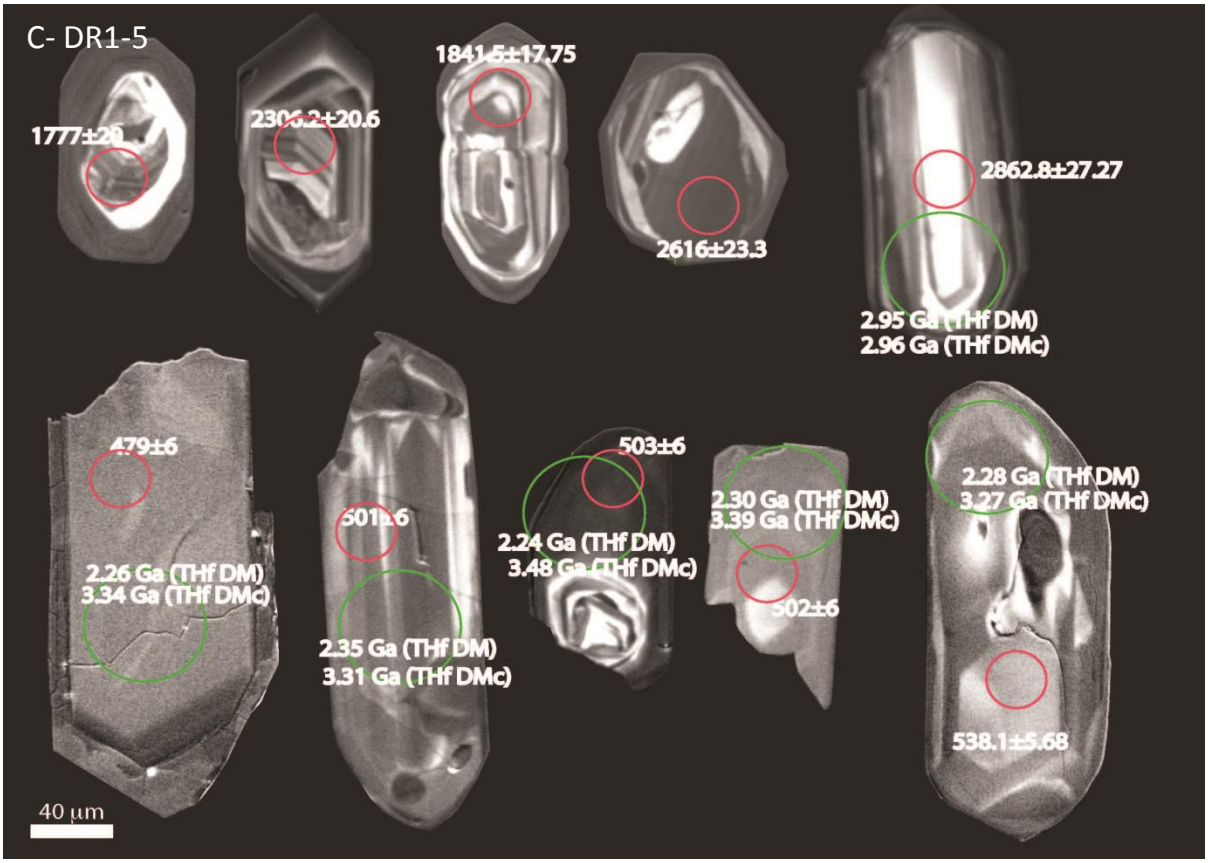
C- DR1-5
1777±20
2306.2±20.6
1841.5±17.75
2616±23.3
2862.8±27.27
2.95 Ga (THf DM)
2.96 Ga (THf DMc)
479±6
2.26 Ga (THf DM)
3.34 Ga (THf DMc)
501±6
2.35 Ga (THf DM)
3.31 Ga (THf DMc)
503±6
2.24 Ga (THf DM)
3.48 Ga (THf DMc)
2.30 Ga (THf DM)
3.39 Ga (THf DMc)
502±6
2.28 Ga (THf DM)
3.27 Ga (THf DMc)
538.1±5.68
40 µm

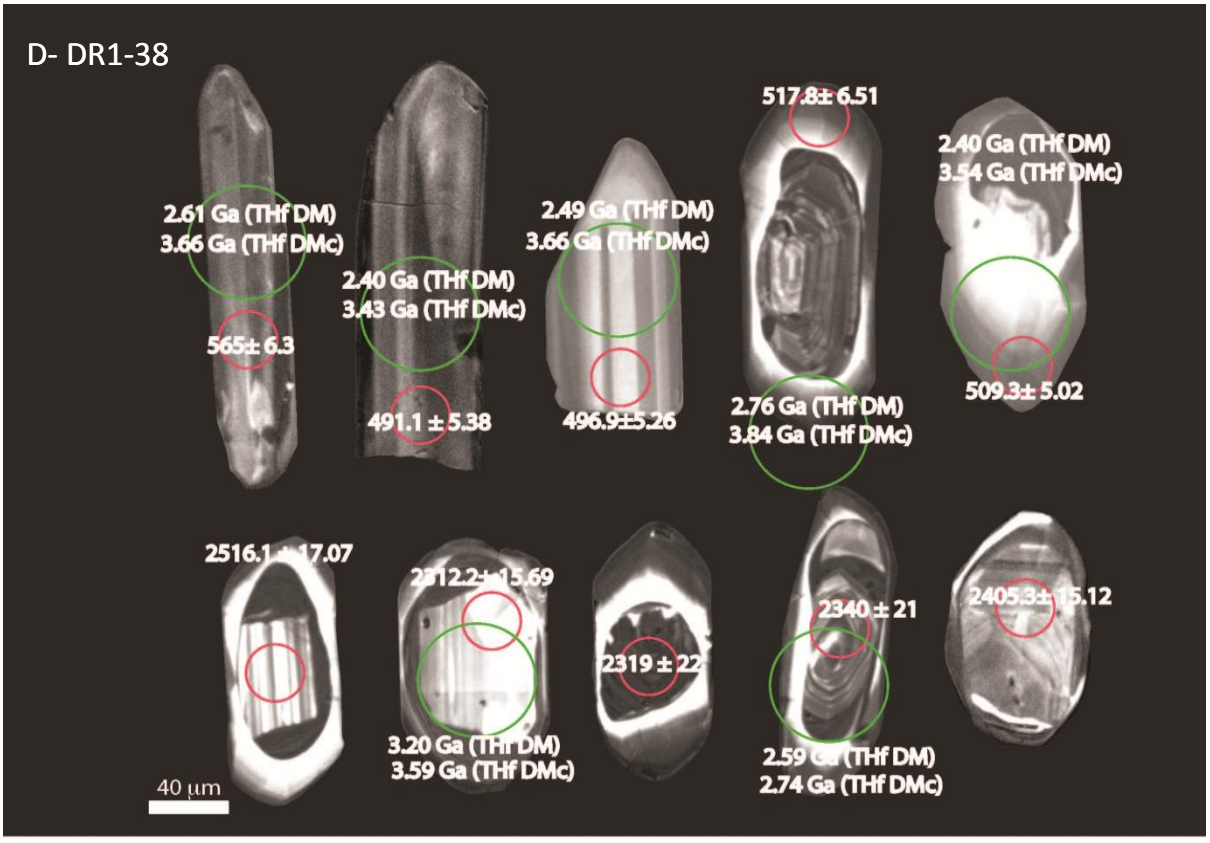
D- DR1-38
2.61 Ga (THf DM)
3.66 Ga (THf DMc)
565± 6.3
2.40 Ga (THf DM)
3.43 Ga (THf DMc)
491.1 ± 5.38
2.49 Ga (THf DM)
3.66 Ga (THf DMc)
496.9±5.26
517.8± 6.51
2.76 Ga (THf DM)
3.84 Ga (THf DMc)
2.40 Ga (THf DM)
3.54 Ga (THf DMc)
509.3± 5.02
2516.1 ± 17.07
2512.2± 15.69
3.20 Ga (THf DM)
3.59 Ga (THf DMc)
2319 ± 22
2340 ± 21
2.59 Ga (THf DM)
2.74 Ga (THf DMc)
2405.3± 15.12
40 µm

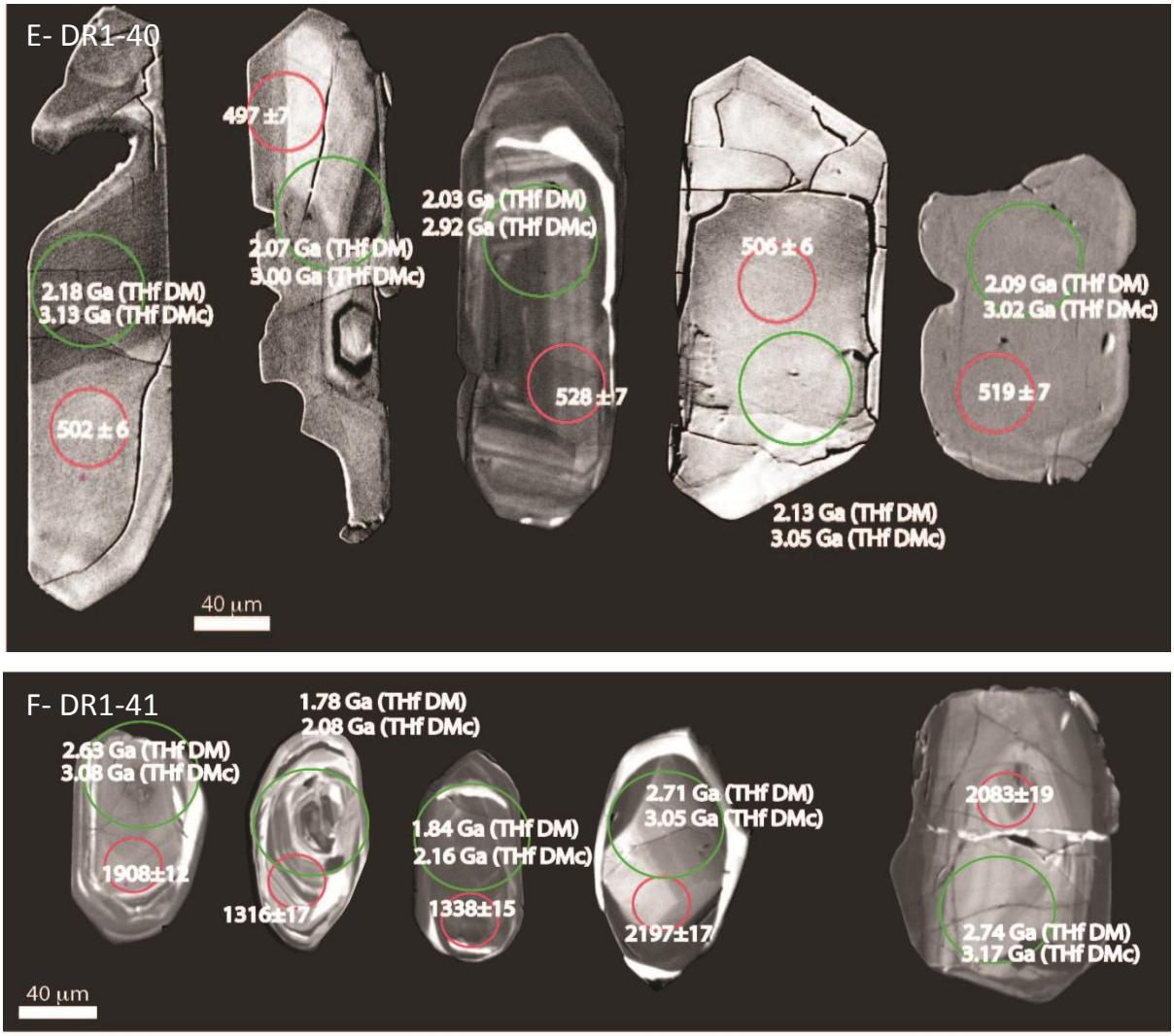

Fig. 7.1. Representative cathodoluminescence images of individual zircons from samples A) DR1-3, B) DR1-4, C) DR1-5, D) DR1-38, E) DR1-40, F) DR1-41.

7.2.2 Zircon U-Pb Geochronology

For all six samples, a maximum of two age groups of zircons per sample were found. For the purpose of this chapter, the younger group of zircons will be named group 1 and the older group, group 2. Five out of the six samples contain group 1 zircons (DR1-3, DR1-4, DR1-5, DR1-38, DR1-40) and four out of six contain group 2 zircons (DR1-4, DR1-5, DR1-38, DR1-41).

Sample	**DR1-3**	**DR1-4**	**DR1-5**	**DR1-38**	**DR1-40**	**DR1-41**
No. U-Pb analyses	47	54	55	50	28	21
No. Lu-Hf analyses	20	16	28	18	14	5
No. Zircon groups	1	2	2	2	1	N/A
No. Group 1 zircons	47	49	27	38	28	3
No. Group 2 zircons	N/A	5	28	12	N/A	N/A
Zircon Types	Igneous	G1 = Igneous G2 = Igneous cores	G1 = Igneous G2 = Igneous cores	G1 = Igneous G2 = Igneous cores	Igneous	N/A
Th content (ppm)	53-1522	29-2103	17-689	66-1145	42-2663	11-13635
U content (ppm)	570-2590	173-2608	103-1728	119-4465	641-6496	174-7742
Initial $^{176/177}$Hf (ppm)	0.281507-0.281700	G1 = 0.281323-0.281827 G2 = 0.281104-0.281746	G1 = 0.281491-0.28653 G2=0.280730-0.281340	G1 = 0.281332-0.281530 G2 = 0.280843-0.281290	0.281413-0.281752	0.281182-0.281916
THf_{DM} (Ga)	2.07-2.42	G1 = 1.96- 2.84 G2 = 2.08- 2.84	G1 = 2.14-2.69 G2 = 2.09-3.30	G1 = 2.35-2.90 G2 = 2.59-3.20	2.03-2.78	1.78-2.08
THf_{DM} (Ga) "crustal"	3.00-3.44	G1 = 2.80-4.23 G2 = 2.80- 3.03	G1= 3.13-4.02 G2 =1.82-3.54	G1= 3.43-3.91 G2 =2.74-3.59	2.92-3.57	2.08-3.17
Epsilon Hf range	-25.30 to -33.32	G1= -22.41 to -46.85 G2= -1.97	G1= -27.96 to -43.41 G2= 5.22 to -5.93	G1= -32.07 to -41.86 G2=1.18 to -12.25	-24.24 to -34.51	-1.10 to -10.37
No. grains common Pb corrected	1	34	24	23	5	8
No. grains rejected for common Pb >2%	7	6	5	3	3	3
Group 2 zircon age range (Ma)	N/A	706-2532.5	961.8-2940.1	2312.2-2706	N/A	381-3171 (all grains age range)

Crustal model line intersects DM (Ga) at	N/A	3.12	3.4	3.68	N/A	N/A
No. grains rejected for pinned intercept	19	26	15	20	13	N/A
No. grains used for group 1 pinned intercepts	28	24	12	18	15	N/A
Min. crystallisation age (Ma)	541.8±5.9	576.5±7.4	538.1±5.7	565±6.3	510.5 ±5.3 (weighted mean average)	N/A
Range of smearing in group 1 zircons (conc. only) (Myr)	541.8 - 478	576.7 - 482	538.1 - 479	565 - 484	528-497	N/A
Smearing range (Myr)	64	95	59	81	31	N/A
MSWD 500 Ma	2.8	3.5	2.7	3.4	1.2	N/A
MSWD 400 Ma	2.2	2.8	1.7	2.5	1.4	N/A
MSWD 300 Ma	2.2	2.5	1.4	2.5	1.4	N/A
MSWD 132 Ma	2.3	2.0	1.16	2.6	1.4	N/A
MSWD 0 Ma	2.5	1.8	1.04	2.6	1.4	N/A

Table 7.1. U-Pb and Lu-Hf isotope data for all six rock samples. G1 = Group 1. G2 = Group 2. THf_{DM} (Ga) = Hf depleted mantle model age. THf_{DM} (Ga) "crustal" = Crustal Hf depleted mantle model age. DM = Depleted Mantle. MSWD = mean square weighted deviation. Conc. = concordant.

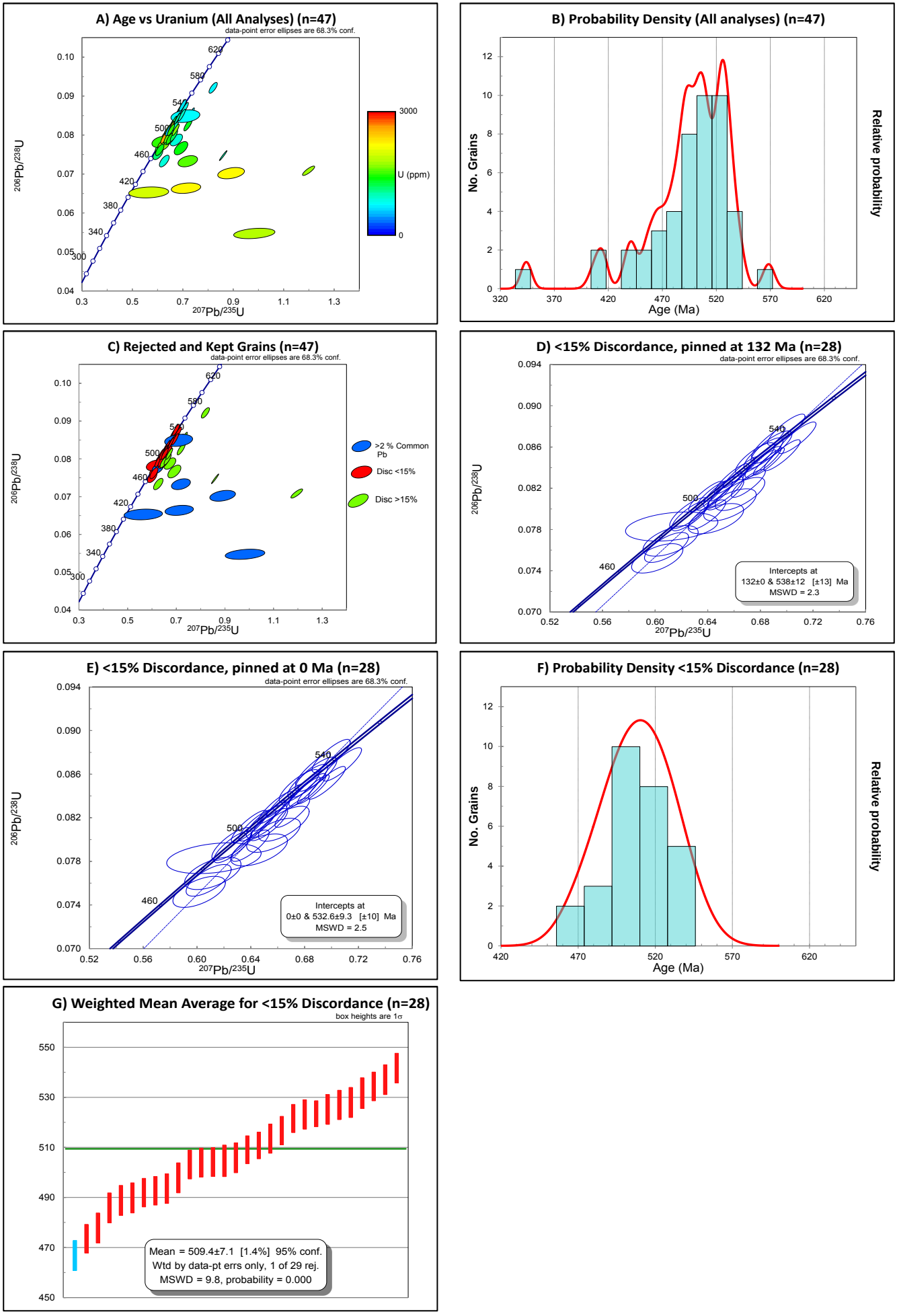

Fig. 7.2. Granite sample DR1-3

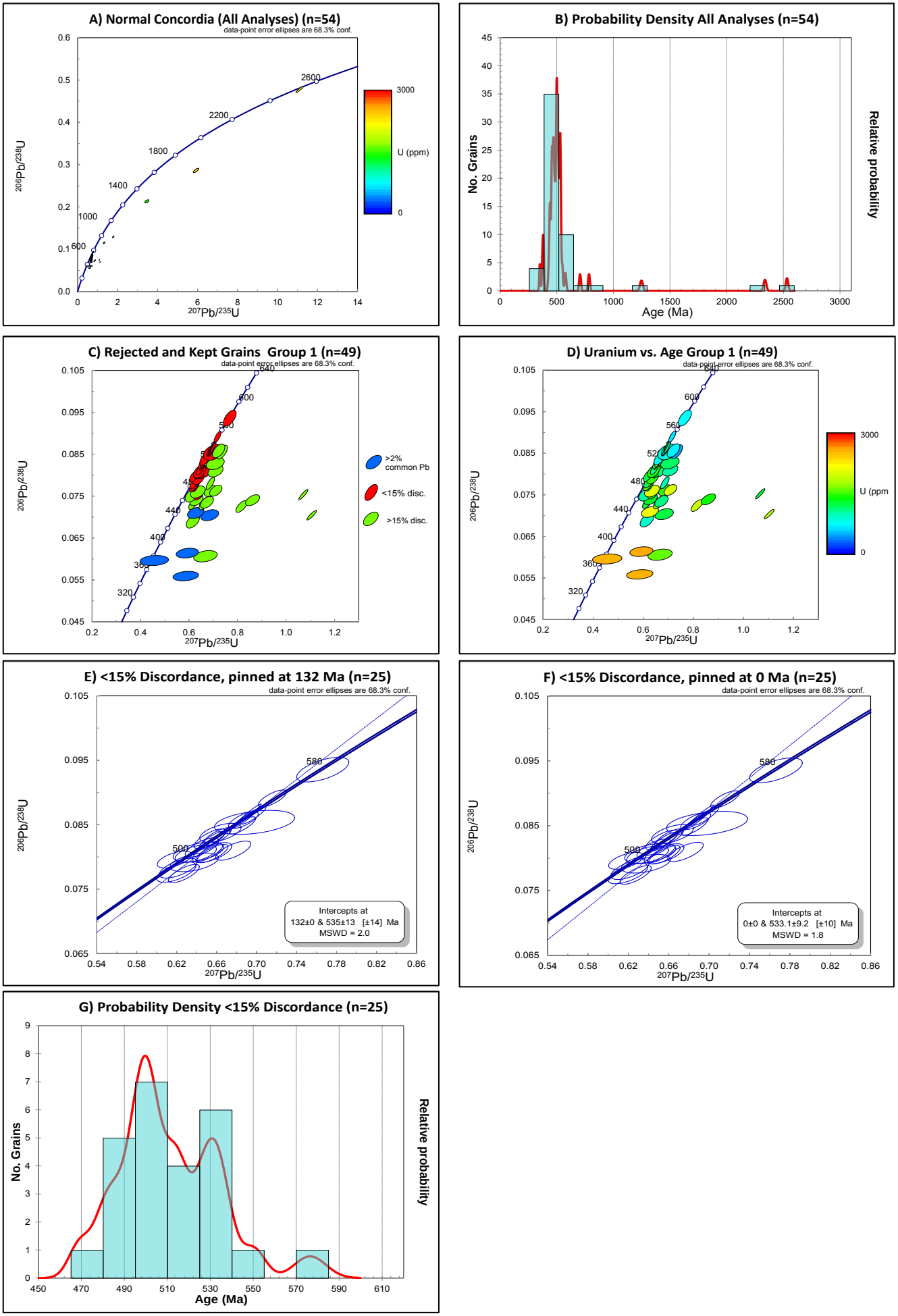

Fig. 7.3. Granite sample DR1-4

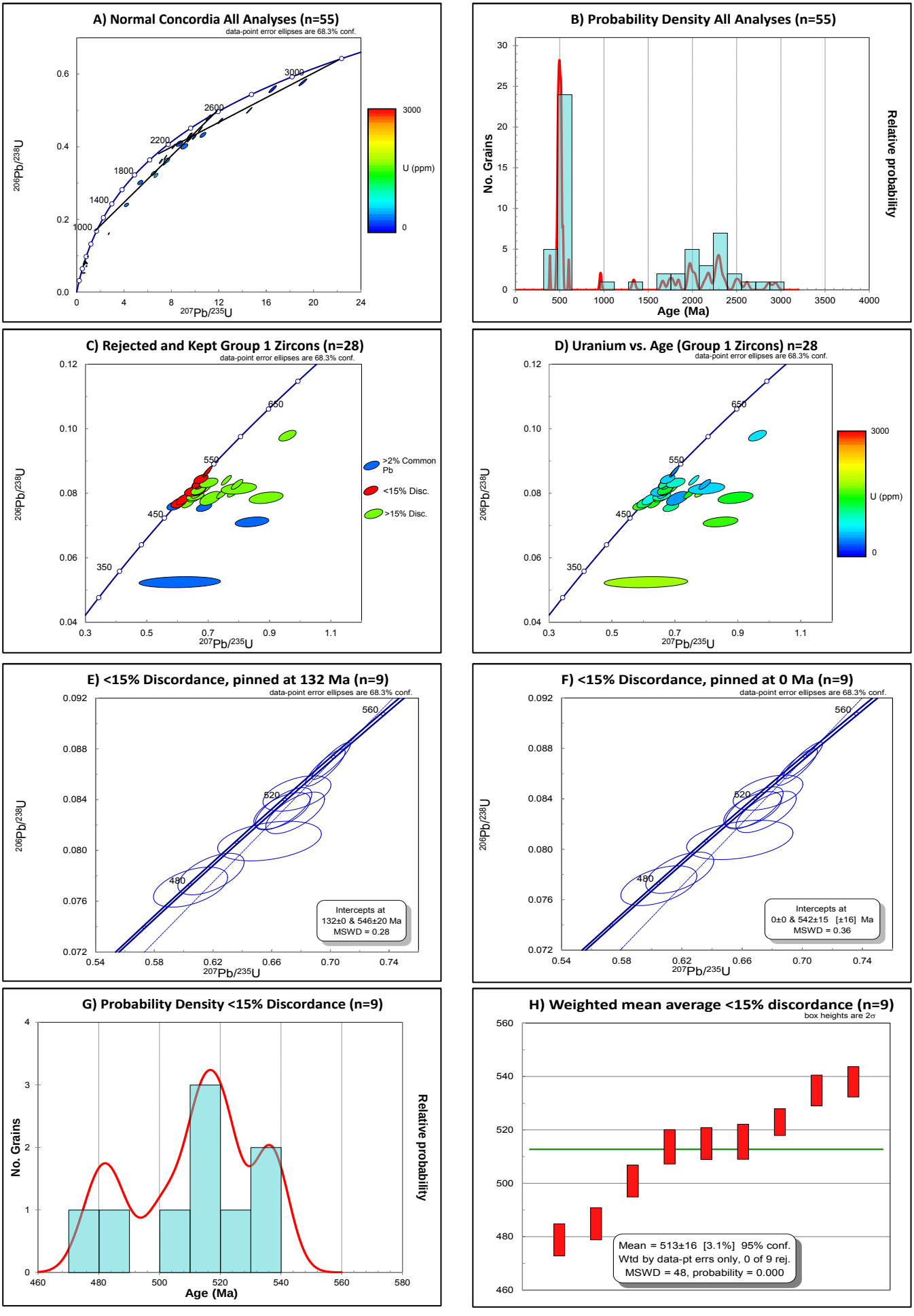

Fig. 7.4. Granite gneiss sample DR1-5

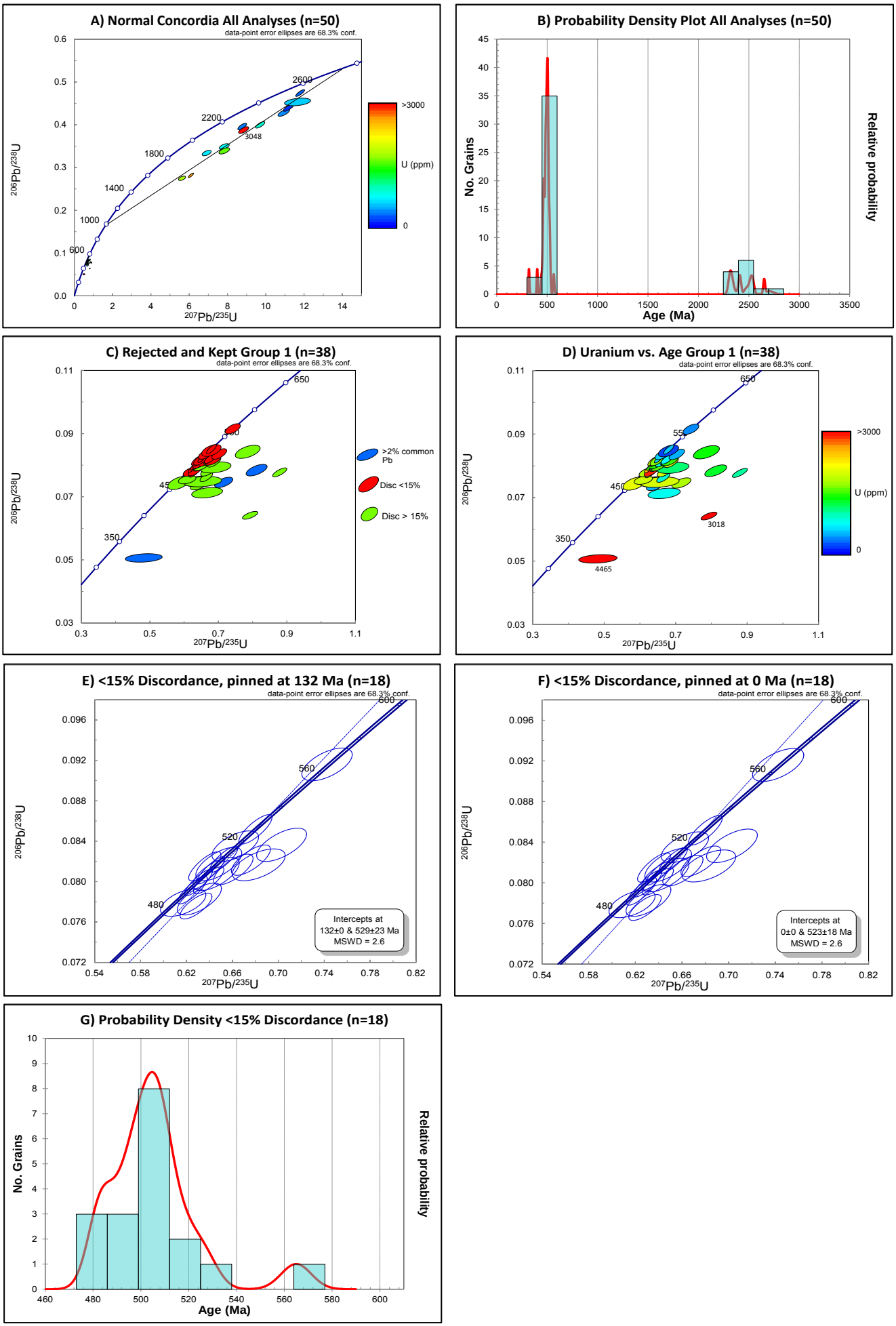

Fig. 7.5. Garnet granite gneiss sample DR1-38

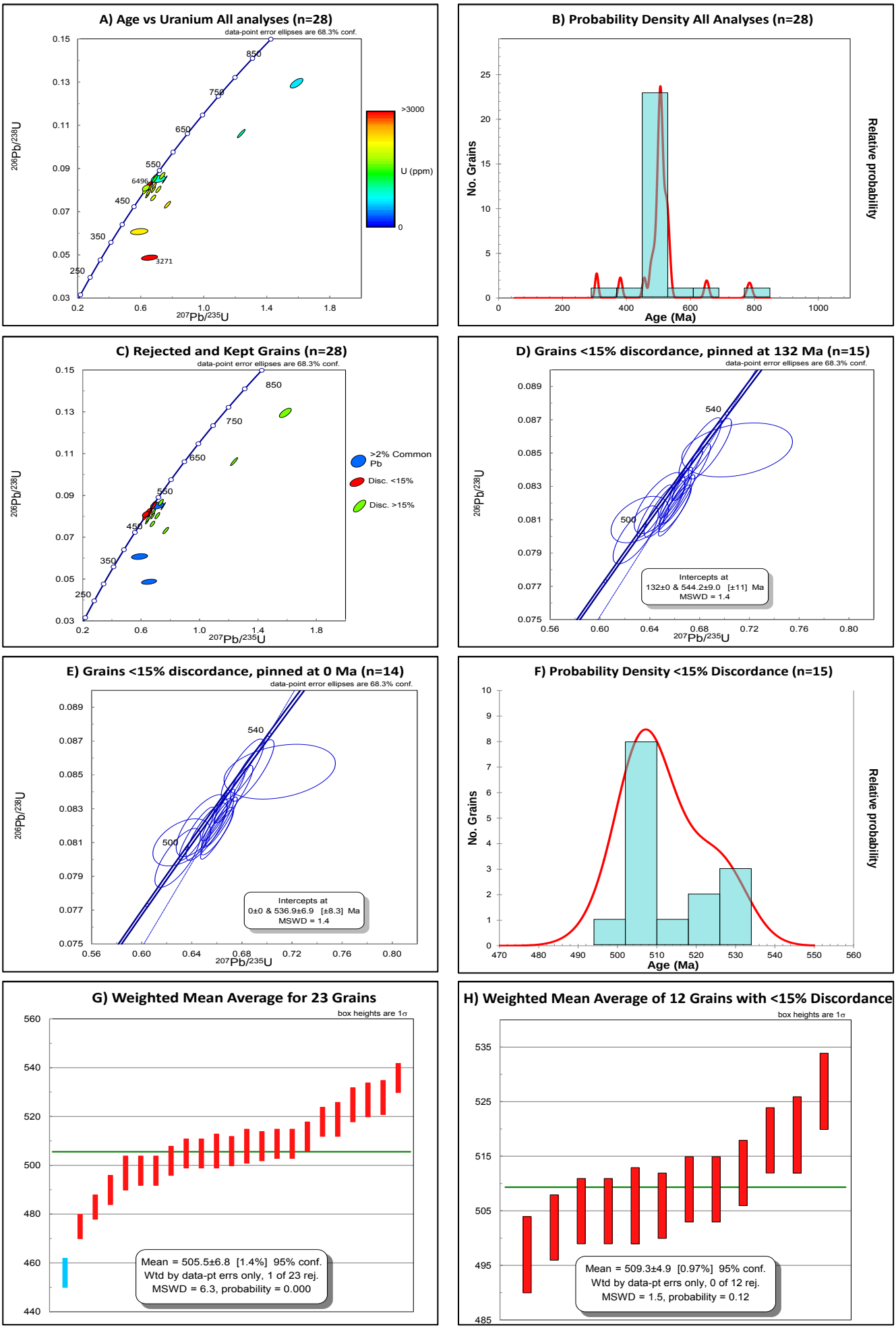

Fig. 7.6. Garnet granite gneiss sample DR1-40

Rejected grains – Group 1 zircons

Grains with common lead exceeding 2% from both groups of zircons were rejected; 27 grains from all 6 samples were rejected with between 3 and 7 grains rejected per sample (Table 7.1, Fig. 7.2a-7.6a). Grains with common lead exceeding 2% tend to have a high discordance.

Group 1 zircons

Five out of six samples (DR1-41 excluded) contain a group of zircons (group 1 zircons) that show a spread along the concordia starting at ca.550Ma and spreading to ca.480Ma. (Fig. 7.2-7.6, Table 7.1). The range of spreading for concordant grains (<15%) varies: 31 Myr (DR1-40), 59 Myr (DR1-5), 64 Myr (DR1-3), 81 Myr (DR1-38) and 95 Myr (DR1-4) (Fig. 7.2-7.6, Table 7.1).

Pinned lower intercepts at ages 500, 400, 300, 132 and 0 Ma were performed on five out of the six samples in an attempt to constrain the age of lead loss (see discussion) (Fig. 7.2 – 7.6). Grains with discordance less than 15% were used. As such, between 13 and 26 grains were rejected from each sample, and between 12 and 28 grains were used from each sample (Table 7.1). Intercept lines which are pinned at 500, 400, 300, 132 and 0 Ma run through the centre of the spread concordant grains in all samples (MSWD ranges from 3.5-1.04 across samples and pinned ages) (Table 7.1).

Weighted mean averages – group 1 zircons

Garnet granite gneiss group B sample DR1-40 group 1 zircons have the least spread of ages (31 Myr), and thus a weighted mean average was used for age determination. Twenty-eight grains were analysed, and fell into one age population (Fig. 7.6). The oldest two grains (651 and 785 Ma) are considered outliers and are excluded on the basis of inheritance. Three grains were rejected for having common Pb exceeding 2%. The remaining twenty-three grains gave a weighted mean $^{206}Pb/^{238}U$ age of 505.5±6.8 (MSWD=6.3 and probability =0.000) (Fig.7.6g). Non statistical scatter of data is evidenced through the low probability of equivalence. As such, grains with discordance greater than 15% were rejected (10 grains rejected). The remaining 13 grains gave a $^{206}Pb/^{238}U$ age of 510.5±5.3 (MSWD = 2.0, probability = 0.024). Non statistical scatter of data is evidenced through the low probability of equivalence. Looking at the weighted residuals of the grains identified, the oldest was identified as degrading the statistical coherence, and was thus rejected. The remaining 12 grains gave a $^{206}Pb/^{238}U$ age of 509.3±4.9 (MSWD = 1.5, probability = 0.12) (Fig. 7.6h).

This method was also applied to samples DR1-3 (spread of 64 Myr) and DR1-5 (spread of 59 Myr). In sample DR1-3, 7 grains were rejected due to common lead exceeding 2% and 12 grains rejected due to discordance greater than 15%. The remaining 28 grains gave a $^{206}Pb/^{238}U$ age of 510.1±7.2 (MSWD = 39, probability = 0.000) (Fig. 7.2g). Sample DR1-5 had 4 grains rejected due to common lead exceeding 2% and 15 rejected due to discordance greater than 15%. The remaining 9 grains gave a $^{206}Pb/^{238}U$ age of 513±16 (MSWD = 48, probability = 0.000) (Fig. 7.4h). Both samples have low probability of equivalence, showing non statistical scatter of data.

Group 2 zircons

Granite, granite gneiss and garnet granite gneiss group A samples DR1-4, DR1-5, DR1-38 and DR1-41 contain a second group of zircons with a similar discordance pattern off the normal concordia (Fig. 7.7). Both free and pinned intercepts through these grains give very high MSWD values and are not included here.

In granite gneiss sample DR1-5 two intercept chords can be hand drawn through group 2 zircons. Intercept chords in isoplot were not used due to the high MSWD values obtained. The higher chord has an upper and lower intercept at ca. 3250 Ma and ca. 2100 Ma while the lower chord has an upper intercept at ca. 2600 Ma and a lower intercept at ca. 1000 Ma (Fig. 7.4a). A hand drawn intercept in garnet granite gneiss DR1-38 has an upper and lower intercept of ca. 2750 Ma and ca. 1000 Ma (Fig. 7.5a). Once again, isoplot was not used for intercept chords due to the high MSWD values obtained. No hand drawn intercepts were made in granite sample DR1-4 as there were only five group 2 grains.

Granite and granite gneiss samples DR1-4 and DR1-5 have one concordant group 2 zircon, 2529.6 Ma and 2532.5 Ma respectively (Table 7.1).

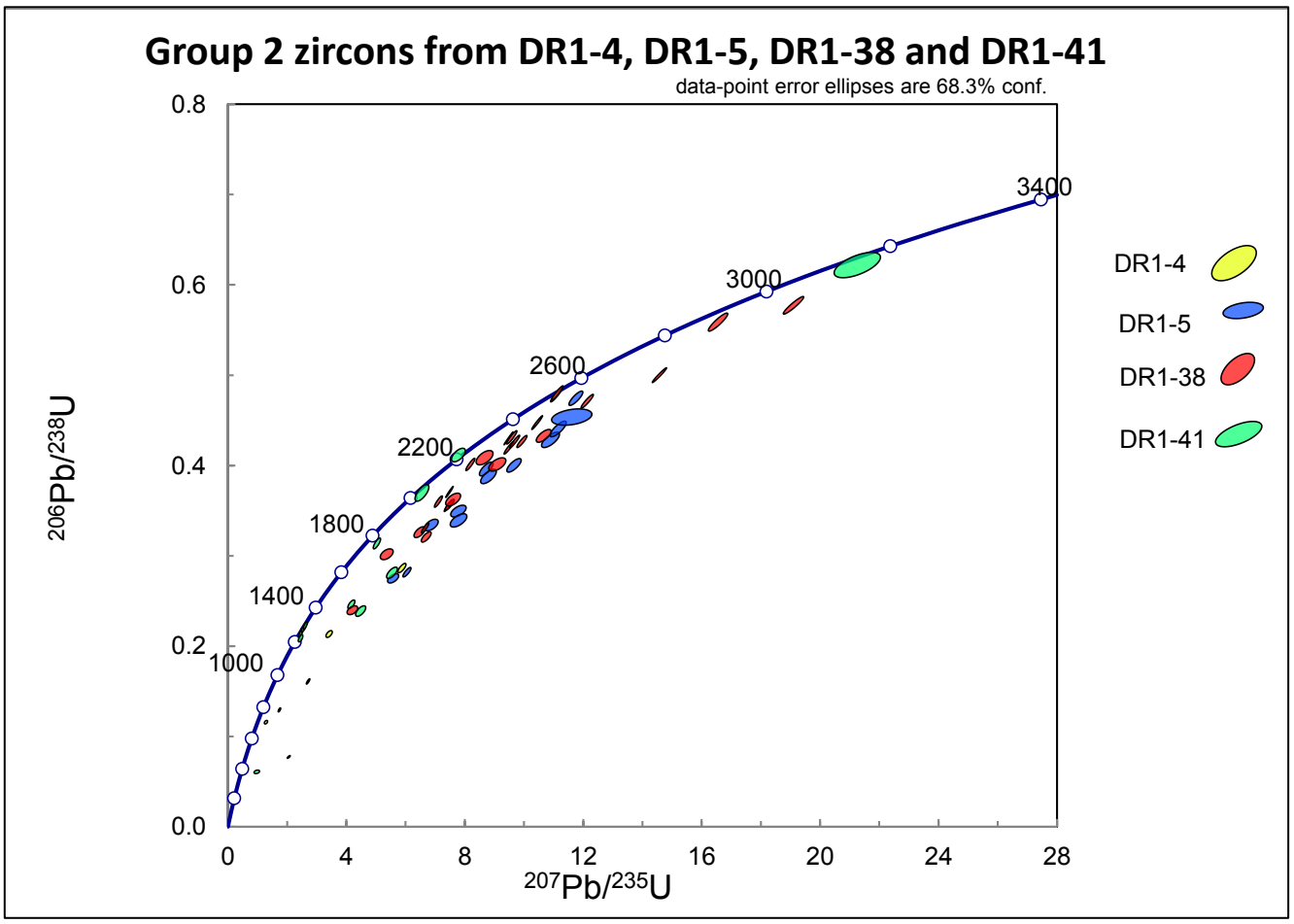

Fig. 7.7. Comparison of group 2 zircons from granite, granite gneiss and garnet granite gneiss samples.

Garnet granite gneiss group A DR1-41

Garnet granite gneiss sample DR1-41 has a spread of concordant and discordant grains along the Concordia from 3171 Ma to the 479 Ma (Fig. 7.8). There is a cluster of four concordant grains ranging from 1294 – 1338 Ma (discordance ranges from 2.7 – 3.9%). The grains older than this plot similarly to group 2 zircons from other samples (Fig. 7.8). There is a cluster of three grains in the high 500 Ma's, correlating to the upper ages of group 1 zircons from the other five samples (Fig. 7.8c).

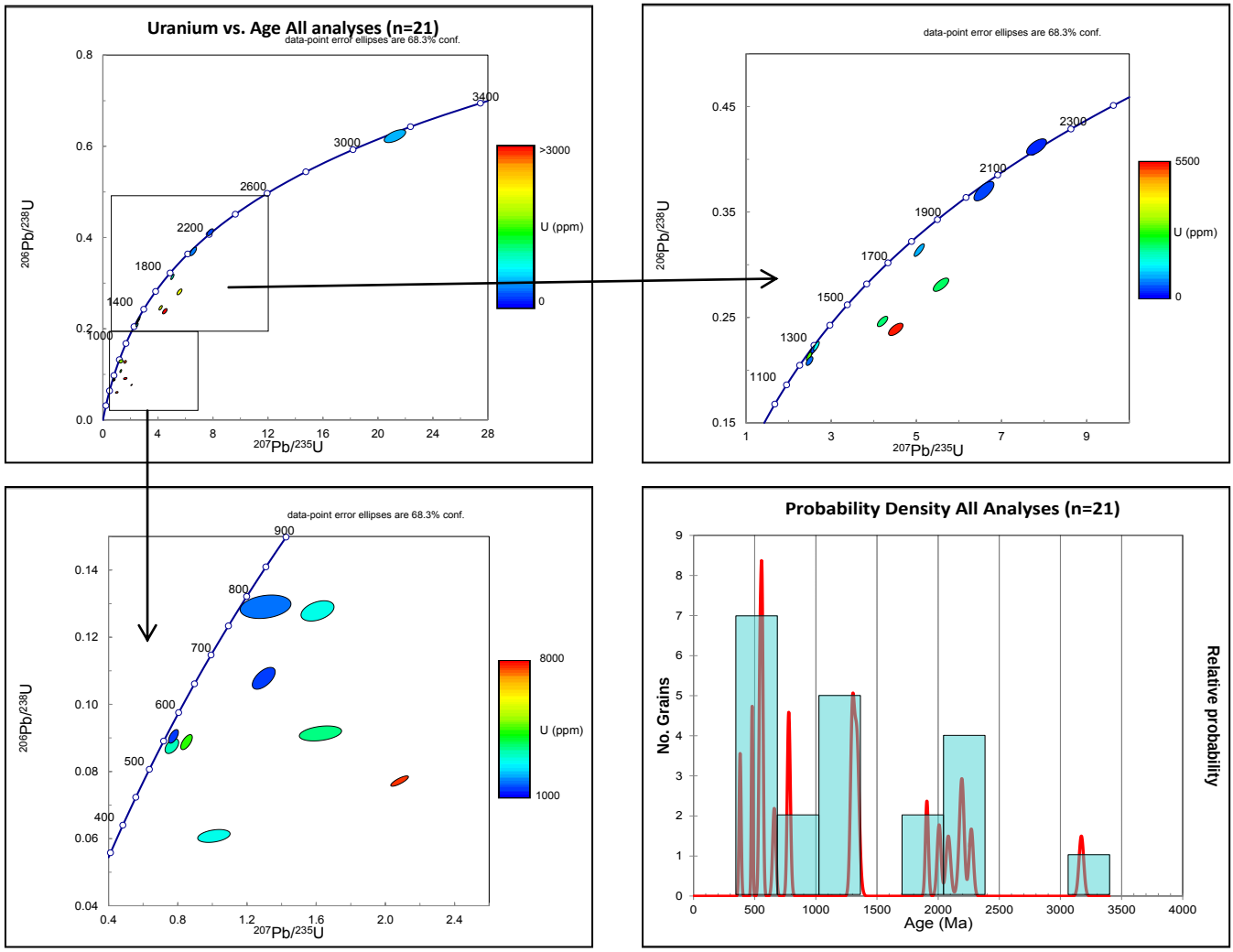

Fig 7.8. Garnet granite gneiss sample DR1-41

DR1-41 vs. DR1-38

A plot of group 2 zircons from garnet granite gneiss group A samples DR1-38 and DR1-41 (Fig. 7.9) shows DR1-41 zircons bracketing the group 2 DR1-38 grains, with DR1-41 grains being generally more concordant than DR1-38. A hand drawn intercept through these two samples has the lower intercept at ca. 1000 Ma and the upper intercept ca. 2800 Ma; neither of these intercepts correlate to the concordant DR1-41 grains bracketing sample DR1-38.

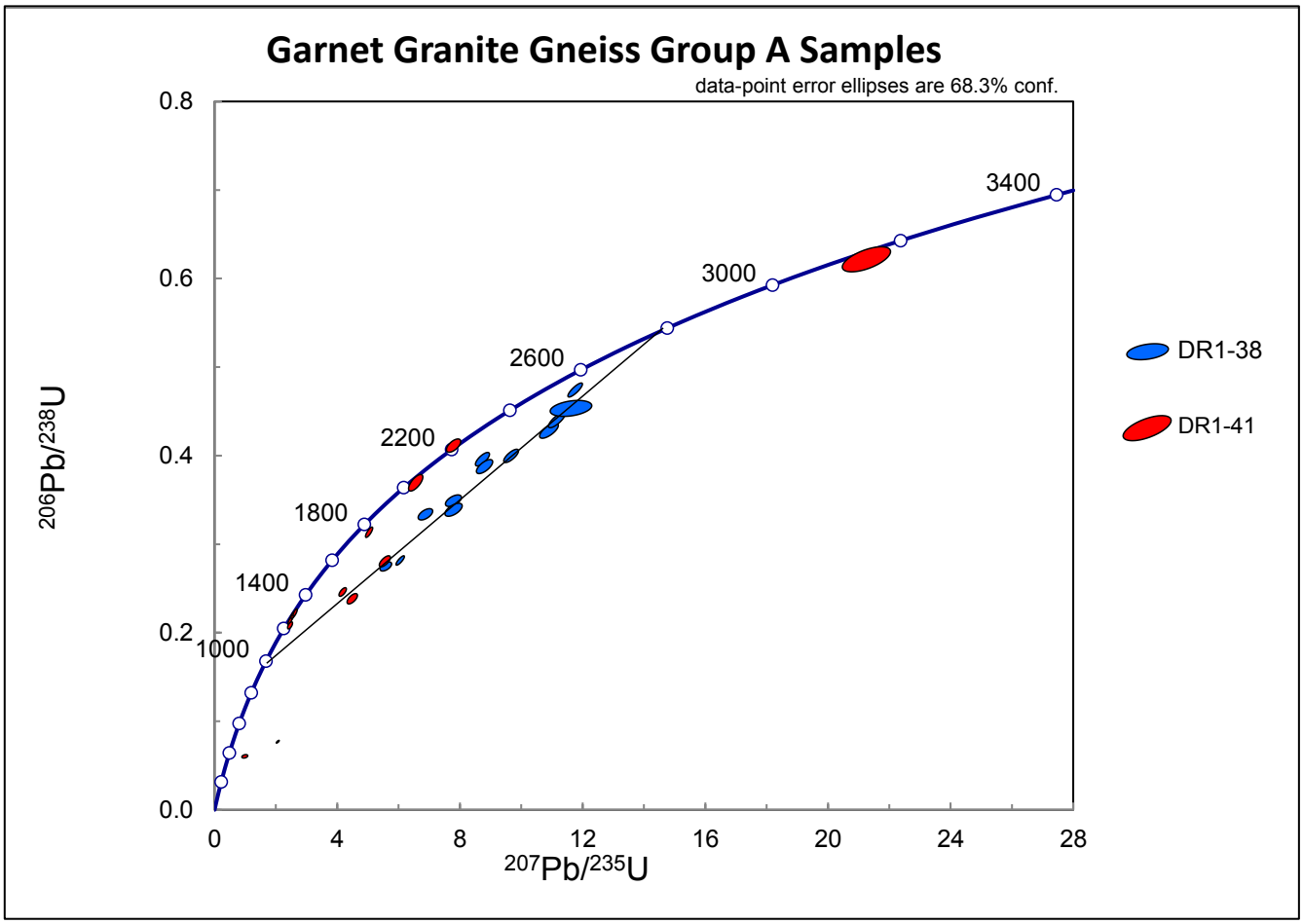

Fig. 7.9. Comparison of group 2 zircons from garnet granite gneiss samples DR1-38 and DR1-41.

Uranium and Thorium concentrations vs. age

Uranium concentration between grains varies greatly within and between samples (Table 7.1). A plot of Uranium vs. age on the concordia shows a vague trend of increasing uranium with decreasing age for group 1 and 2 zircons (Fig 7.2b-7.6b). The more discordant grains tend to have a higher Uranium concentration. However, a plot of Uranium vs. age on a bivariate plot (Fig. 7.10a, b) shows no correlation between age and uranium content. Similarly for Th vs. age, there is no correlation between age and Th content (Fig. 7.10c, d).

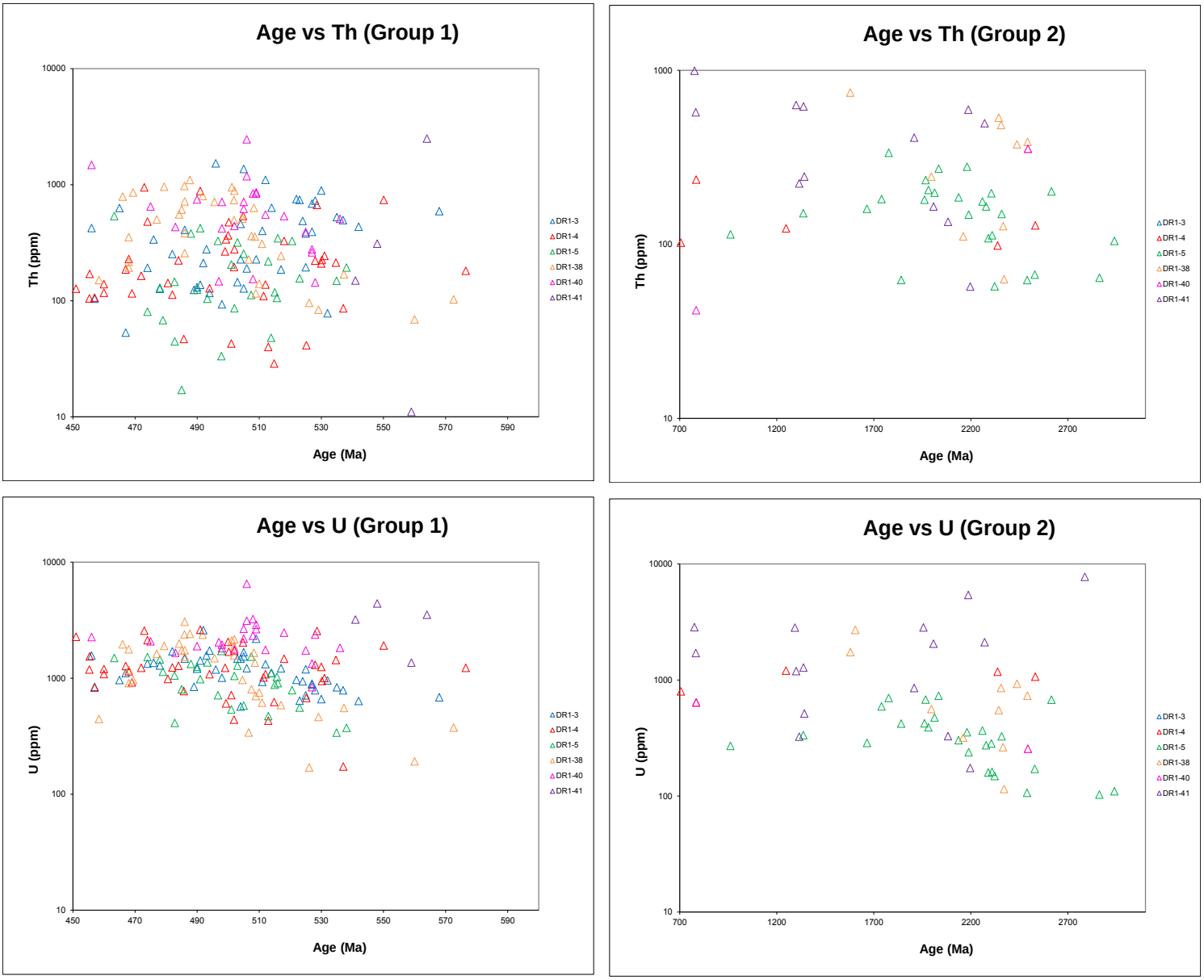

Fig. 7.10. Age vs. Th for **a)** group 1 and **b)** group 2 zircons and Age vs. U for **c)** group 1 and **d)** group 2 zircons.

Age and zircon type correlation

In granite gneiss and garnet granite gneiss samples DR1-5 and DR1-38, the two groups of zircons identified in zircon morphology above form the two age groups of zircons described here. In both samples, group A zircons, the zircons with no cores and rims form the younger group 1 zircons. Core analyses from group B comprise the older group 2 zircons while the rim analyses from group B plot with the group A zircons in the younger group 1 zircons.

7.2.3 Zircon Lu-Hf Isotope Signatures

Initial $^{176/177}$Hf isotopes

All samples (DR1-41 excluded) exhibit similar trends for initial $^{176/177}$ Hf isotopes vs. age for the group 1 zircons. As the age decreases, the $^{176/177}$Hf isotopes stay relatively stable (Fig. 7.11 a-e, Table 7.1). Granite sample DR1-3 has the third most radiogenic signature (Fig. 7.11a). Granite sample DR1-4 has the most radiogenic $^{176/177}$ Hf isotope signature (Fig. 7.11b). Granite gneiss sample DR1-5 shows scattering of data, with the second least radiogenic signature (Fig. 7.11c). Garnet granite gneiss sample DR1-38 has the least radiogenic isotope values (Fig. 7.11d). Garnet granite gneiss sample DR1-40 has the second most radiogenic isotope signature (Fig. 7.11e).

Lu-Hf isotopes for group 2 zircons were analysed from granite, granite gneiss and garnet granite gneiss samples DR1-4, DR1-5 and DR1-38 (Table 7.1, Fig. 7.12). Granite sample DR1-4 had four group 2 grains, three of which have age discordance greater than 15%. As such, these grains have been projected back to the DM model line, showing a similar range of spread as DR1-5 and DR1-38 (Fig. 7.12d). Granite gneiss sample DR1-5 group 2 zircons show a range of $^{176/177}$Hf initial isotope values. The ^{176}Lu/^{177}Hf ratio average continental crust model line of 0.015 fits through the average of group 1 zircons and roughly through the middle of the group 2 zircons, intersecting the DM model line at 3.4 Ga (Fig. 7.12b). One grain had an age discordance greater than 15% and was projected back to the DM model line (Fig. 7.12d). Garnet granite gneiss sample DR1-38 shows a scattering of group 2 zircon initial $^{176/177}$Hf isotope ratios similar to DR1-4 and DR1-5 (Fig. 7.12c). The same average continental crust model line fits well through the group 1 zircons and the two least radiogenic group 2 zircons, intersecting the depleted mantle model line at 3.68 Ga. The more radiogenic group 2 zircons have similar, but slightly lower $^{176/177}$Hf isotope values compared to the group 1 zircons. One grain had age discordance greater than 15% and was projected back to the DM line (Fig.7.12d). Overall group 2 zircons from these three samples have similar scattering of data (Fig. 7.12d).

An average and standard deviation of group 1 and group 2 zircons were calculated, and the average continental crust ^{176}Lu/^{177}Hf model line of 0.015 plotted through them (Fig. 7.12f). Based on 2sd for each average, the line intersects the DM model line ranging from 2.8 – 3.92 Ga. A line through the centre of each average intersects the DM line at 3.4 Ga.

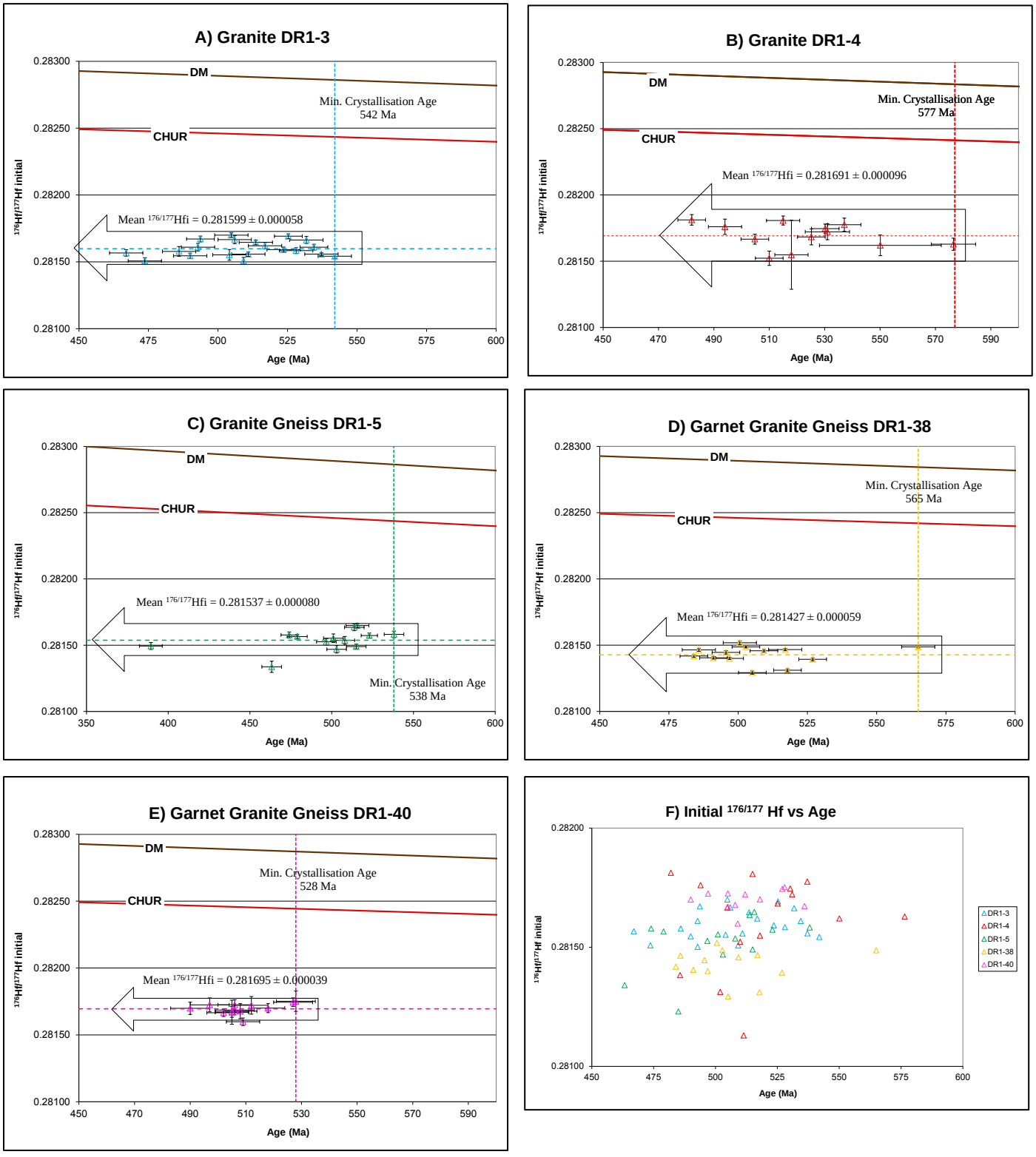

Fig. 7.11. Initial $^{176/177}$Hf isotope data for group 1 zircons from granite, granite gneiss and garnet granite gneiss samples a) DR1-3, b) DR1-4, c) DR1-5, d) DR1-38, e) DR1-40 and f) combined group 1 zircon data. Error bars are 2sd. Width of arrow represents 2sd from the average.

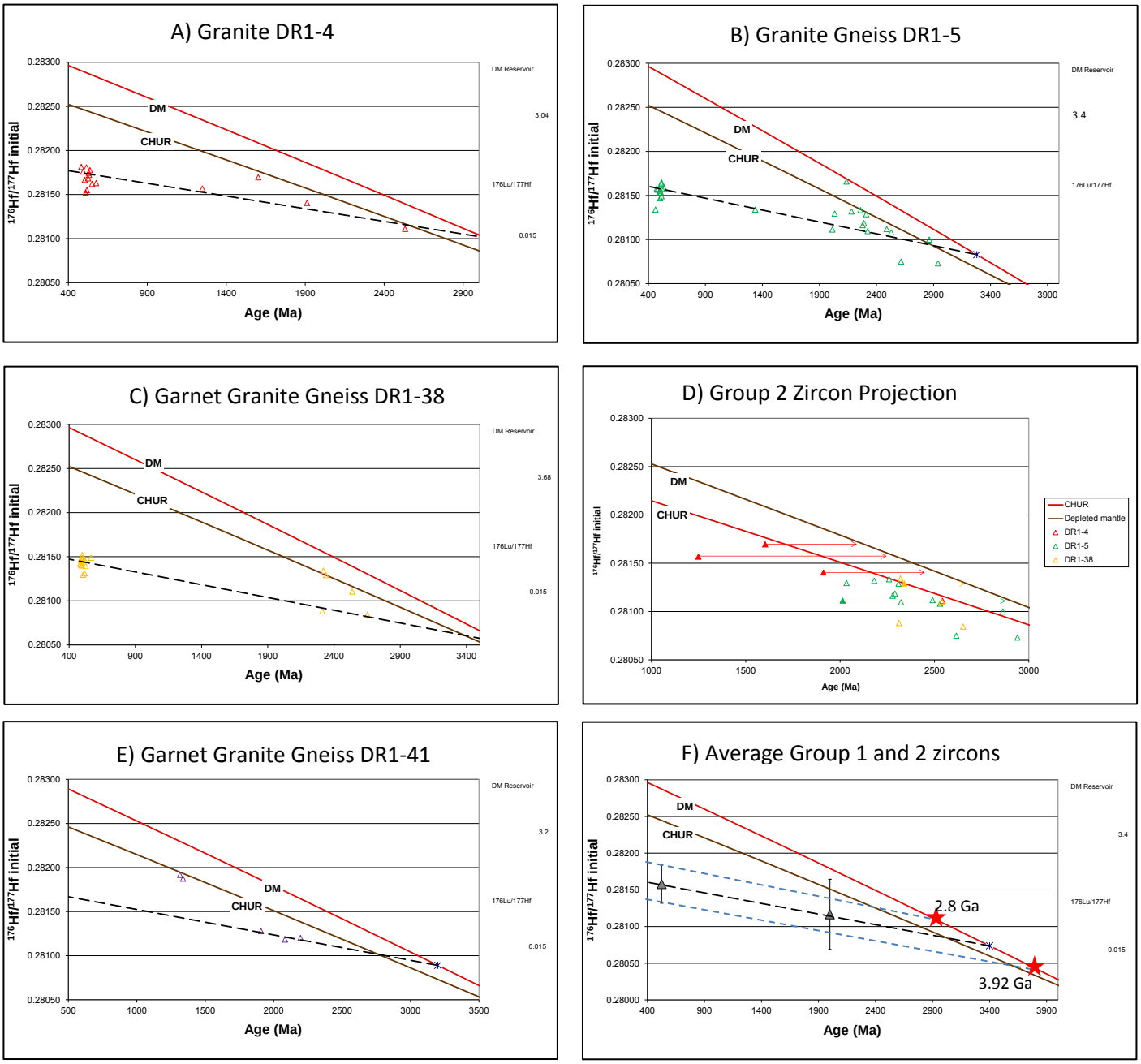

Fig. 7.12. All initial $^{176/177}$Hf isotope analyses for samples a) DR1-4, b) DR1-5, c) DR1-38, d) combined group 2 zircons with projections for analyses with age discordance >15%, e) DR1-41 and f) average initial $^{176/177}$Hf isotopes for group 1 an group 2 zircons.

Only five grains were analysed from garnet granite gneiss sample DR1-41. These show an increase in Hf isotope as the age decreases (Fig. 7.12e).

Epsilon vs. Age

A plot of Epsilon Hf vs. Age (Fig. 7.13) shows that the older group 2 zircons have more positive values than the group 1 zircons. The group 1 zircon Epsilon Hf (EHf) ranges between -22.41 and -46.85 for all five samples, and the group 2 EHf ranges from -12.25 to 5.22 (Table 7.1). Individual analyses with age discordance greater than 15% were not used in this figure.

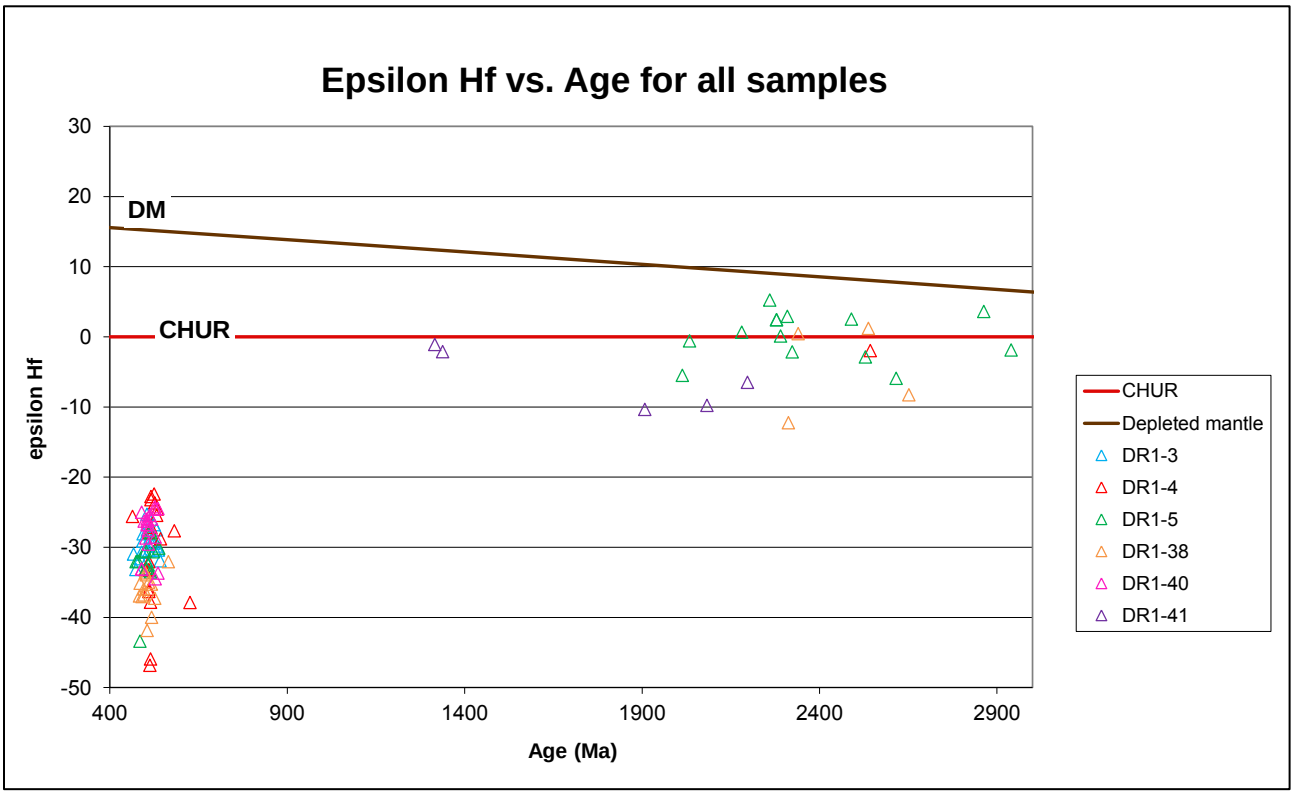

Fig. 7.13. Epsilon Hf vs. Age for all Lu-Hf analyses from all six samples. Individual analyses with age discordance greater than 15% were not included.

Y, $^{176}Lu/^{177}Hf$ and $^{176}Lu/^{177}Hf$ vs. Age

Yttrium vs. age was ploted on a bivariate plot for group 1 and 2 zircons (Fig. 7.14a,b). No correlations can be seen. Group 1 zircons generally show a greater spread of Y values than group 2. Age vs. $^{176}Yb/^{177}Hf$ bivariate plot shows no correlation between age and isotope ratio (Fig. 7.14c,d). Group 1 and 2 zircons show a similar range of scattering. Age vs. $^{176}Lu/^{177}Hf$ bivariate plot shows no correlation between age and isotope ratio (Fig. 7.14e,f). Group 1 and 2 zircons show a similar range of scattering.

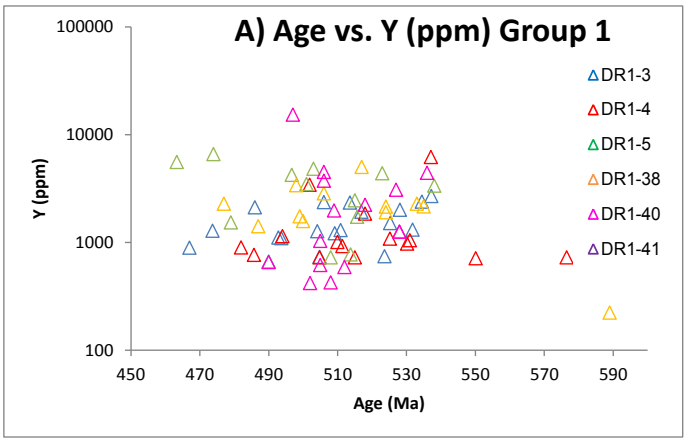

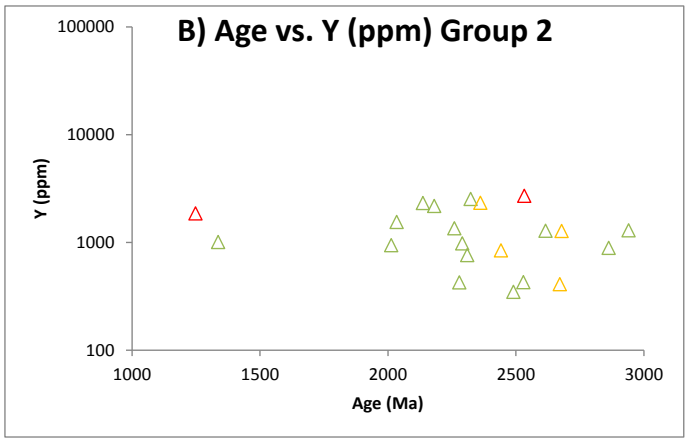

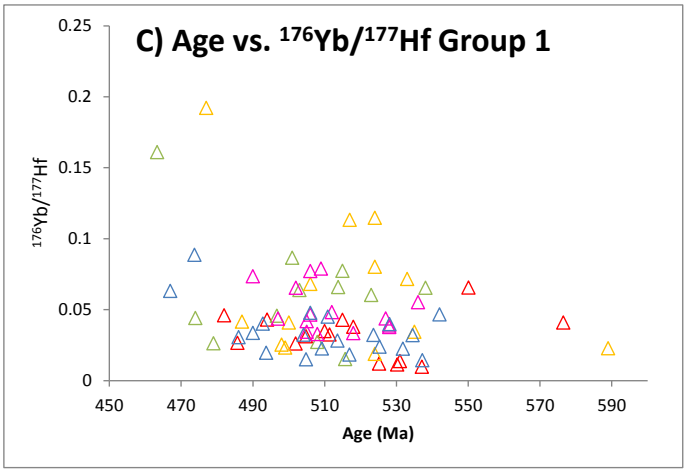

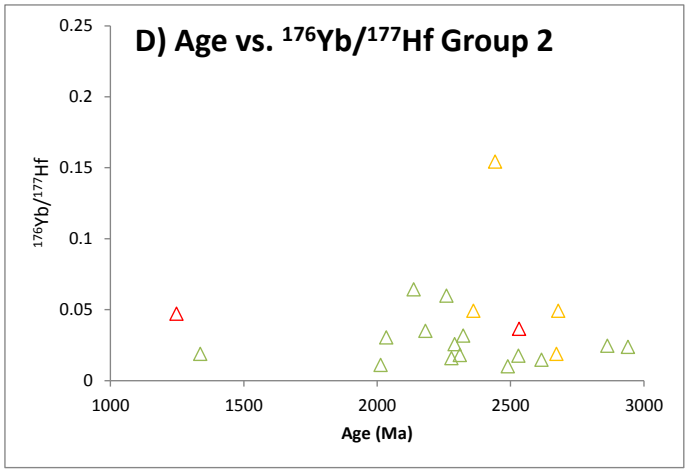

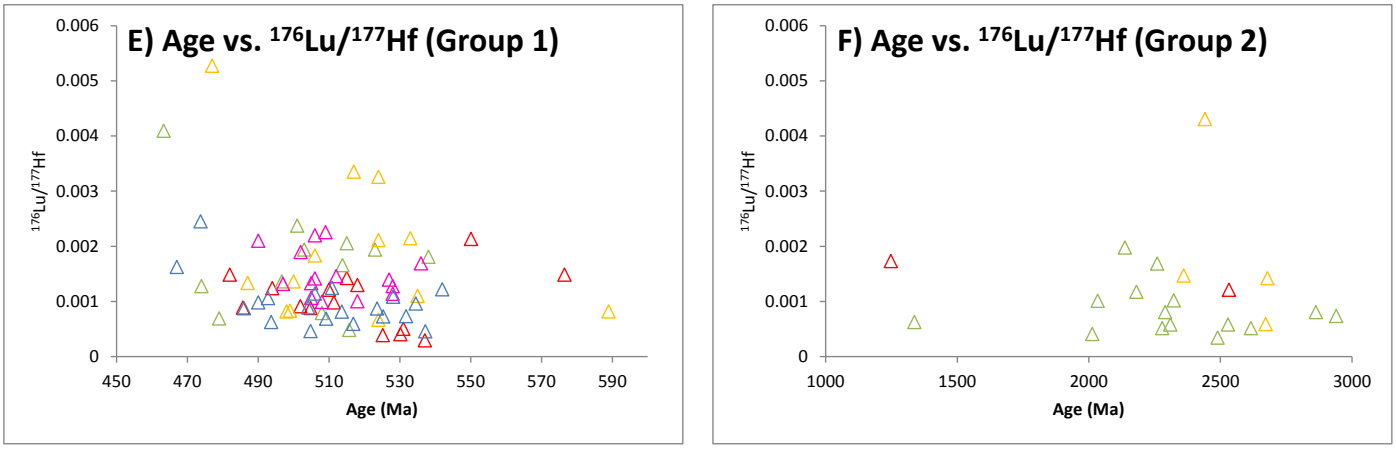

Fig. 7.14. Age vs. Y for **a)** Group 1 and **b)** Group 2 zircons. Age vs. $^{176}Yb/^{177}Hf$ for **c)** Group 1 and **d)** Group 2 zircons. Age vs. $^{176}Lu/^{177}Hf$ for **e)** Group 1 and **f)** Group 2 zircons. Key presented in a).

Chapter 8 - Discussion

The aim of this section is to explain the processes that have formed and subsequently affected the seven representative rock samples from Batavia Knoll. Additional insights from the relationships between individual samples have implications for linking Batavia Knoll with the Kuunga Orogeny. This provides a greater understanding of this poorly exposed geological orogeny, achieved through the combination of petrographical, geochemical and geochronological analytical techniques.

Granite, granite gneiss and vein processes and relationships

On the basis of similar petrographical textures and mineral assemblages, overlapping EMP mineral chemistry data and similar zircon U-Pb and Lu-Hf isotope data, granite, granite gneiss and the intermediate gneiss vein samples DR1-3, DR1-4, DR1-5 and DR1-34 are likely related.

Support for this is found in the mineral chemistry feldspar data. Feldspar data from all three samples overlaps; each with plagioclase (oligoclase → andesine), k-feldspar and albite. In all samples, albite occurs in the cores of K-feldspar grains. This observation in conjunction with the wispy K-feldspar texture documented in thin section is consistent with exsolution of albite from the primary K-feldspar.

Granite sample DR1-4 demonstrates and interaction between two rock units, through the three types of biotite which correspond to the schist (green biotite), granite (red/brown biotite) and schist-granite contact (highly chloritised biotite). The differing chemistry of the schist and granite biotite, with the contact biotite representing a mixture of these chemistries shows an interaction between the two layers and confirms that the schist is a different lithological unit.

Garnet granite gneiss group A processes and relationships

Based on the analytical methods of petrography, mineral assemblage, mineral EMP chemistry and U-Pb zircon data, garnet granite gneiss group A samples DR1-38 and DR1-41 demonstrate qualities which are consistent with dredge derivation from the same lithological unit.

The retrograde garnet break down texture which is synonymous between samples in thin section combined with the identical garnet zonation profiles in mineral chemistry supports these two samples originating from one lithological unit. Mineral chemistry shows garnet grains in both samples to have unzoned cores with narrow (up to 50 um) rims of variable composition. The unzoned cores represent element homogenisation at peak metamorphic conditions (Spear, 1993). The narrow rims have increased Mn content consistent with incorporation of the Mn released from

the decaying garnet rim back into the remaining garnet. Garnet grain rims also have decreased Fe and Mg content and increased XFe consistent with a retrograde process (Danis *et al.*, 2010). Ca content remains unchanged in the rims due to limited lattice diffusion and effective intergranular element migration of Fe and Mg (Hwang *et al.,* 2003). The positive linear correlation of XFe vs. Spessartine in Fig.5.6 further indicates diffusion during cooling from a metamorphic event (Spear, 1993). The high R^2 values of 0.918 and 0.9225 for XFe vs spessartine in DR1-38 and DR1-41 respectively shows the correlation is statistically valid and meaningful.

Mineral chemistry data from biotite and feldspar do not record the retrograde reaction indicating that these two minerals are in equilibrium. Two types of feldspar were documented in these samples: coarse matrix feldspar and fine coronal feldspar around garnet. The mineral chemistry of the two types overlap as andesine. Biotite chemistries do not show zonation outside of error.

In thin section, DR1-41 shows evidence for higher strain through the elongated quartz grains defining the foliation. The leucocratic layers in DR1-41 are much smaller than in DR1-38, consistent with hand sample analysis which shows DR1-41 to be much darker. It is recognised that this could be a result of sample size and location, due to the sample size of DR1-38 being thrice the size of DR1-41 and the unknown location of each sample along the dredge track. None-the-less, this finding is not inconsistent with the rocks being from a single lithology.

Using U-Pb isotope data provides for results which are inconclusive but continue to support the likelihood of a single lithology. Sample DR1-41 contains few group 1 and group 2 zircons which correlate to DR1-38. However, DR1-41 also contains a concordant population of zircon clustering at 1294 – 1338 Ma, which is absent in DR1-38. Due to the zircon poor nature of DR1-41, its age and relationship with DR1-38 is difficult to determine. However, it is likely that the cluster of 1294 – 1338 Ma zircons are inherited group 2 zircons and the three grains at ca. 550 Ma represent a common igneous age which lends support to a singular lithology hypothesis.

Garnet granite gneiss group B processes and relationships

On the basis of mineral chemistry data of feldspar (more sodic) and garnet (higher almandine content) compared with garnet granite gneiss group A samples and a lack of garnet breakdown textures in thin section, sample DR1-40 is a different rock unit to the group A garnet granite gneisses. There is no evidence for compositional zonation outside 1sd error across garnet grains, indicating one growth phase and elemental homogenisation at peak metamorphic conditions.

Intermediate gneiss processes and relationships

Mineral chemistry analysis has determined the composition of amphibole as hornblende, indicating that this rock equilibrated at amphibolite facies.

Shared history of alteration

The seven rock samples examined have a shared history of alteration, evidenced through petrographic, XRF and mineral chemistry data. Granite, granite gneiss and garnet granite gneiss samples DR1-3, DR1-4. DR1-5, DR1-40 and DR1-41 have low total alkali content determined by XRF, indicating alteration and thus precluding detailed geochemical whole rock analysis of these samples. The ASI values (> 1.1) for these five samples are not valid due to the highly mobile state of the alkali elements during alteration. The chloritisation of biotite grains documented through mineral chemistry in samples DR1-3, DR1-4, DR1-5, DR1-34 vein, DR1-40 and DR1-41 (through low K_2O weight percentage) in conjunction with chloritisation along biotite cleavage planes in thin section, is consistent with these samples experiencing alteration. The sericite alteration in feldspar grains further indicates alteration. Garnet granite gneiss and intermediate gneiss samples DR1-38 and DR1-34 have higher total alkali contents, and are less altered. This is seen through the lesser amounts of chloritised biotite and sericite alteration documented in these samples. Thus, the ASI (>1.1) of these two samples is considered to be valid, placing these rocks as periluminous. This is consistent with the high Al^{V1} of biotite in DR1-38 and the high modal percentage of biotite (40%) in DR1-34. The timing of alteration is unconstrained, and could have occurred at one or both of the major tectonothermal events; final amalgamation of Gondwana (ca. 500 Ma) or Cretaceous rifting of India and Australia (ca. 132 Ma). Furthermore, seafloor hydrothermal alteration post Gondwana break up could have contributed to alteration. None-the-less all 7 samples show some degree of alteration post emplacement.

Granitoid classification - S-type granitoids

The Al left over in the octahedral site of biotite (Al^{V1}) for the granitoids DR1-3, DR1-4, DR1-5, DR1-38, DR1-40 and DR1-41 is relatively high (0.18-0.40) evidencing the periluminous nature of these rocks. The high Al^{V1} for samples DR1-38, DR1-40 and DR1-41 is consistent with biotite growth in the presence of garnet (Flood, pers.comm. 2012). The ASI for the majority of these samples is invalid due to alteration. However, the ASI of sample DR1-38 is valid and >1.1, consistent with a periluminous rock. As such, these are S-type granitoids.

Intermediate gneiss sample DR1-34 has no Al^{V1} in biotite. The ASI of this rock is > 1.1. It is likely that this is not a function of weathering, due to the minimal alteration evidenced in thin section. The lack of Al^{V1} suggests that this rock is not Al rich, however, the high ASI could be a reflection of the high modal (40%) abundance of biotite.

Geochronology discussion

Group 1 zircons

U-Pb and Lu-Hf isotopes from zircon were utilised to determine the age of and relationships between Batavia Knoll granitoid samples, and subsequent relationships with the Kuunga Orogeny.

Long-term LA-ICP-MS analyses of the Mud tank standard zircon produce a Gaussian distribution of single zircon grain ages spread about the mean age of 731 ± 34 (1sd, n=73) Ma; the maximum difference between the youngest and oldest grains in this population is ca. 100 Myr (Jackson *et al.,* 2004). However, a weighted mean average provides for an age of 731 ±3.9 Ma. The external precision (2 RSD) of the method on single grains ranges from 2-4%, while the external precision (2 RSD) of a group of more than 15 grains from one population is less than 1% (Jackson *et al.,* 2004). Due to the robust nature of the weighted mean average on a single population of zircon, it is most likely that the ca. 100 Myr spread is a result of poor analyses (for example, over cracks and zoning domains or common lead) for the less abundant younger and older analyses.

As such, the spread along the concordia seen in Batavia Knoll granitoids is outside the expected external precision for the LA-ICP-MS method. However, due to the young age of Batavia Knoll granitoids (ca. 550 Ma), the spread in ages along the concordia for a single, undisturbed population will more likely be a maximum of ca. 70 Myr. Accordingly, the spread in samples DR1-40 (31 Myr), DR1-5 (59 Myr) and DR1-3 (64 Myr) could represent a single, undisturbed population. If one undisturbed population exists, a weighted mean average will provide for robust age determination. A weighted mean average for age determination was performed on sample DR1-40, and was valid due to the lower probability of equivalence and MSWD value, yielding an age of 510.5±5.3 Ma. However, 16 out of 28 grains (57%) were rejected to obtain such an age. It is likely, based on lead loss and the limited amount of grains used for the weighted mean average, that this sample has experienced isotopic disturbance, and that its calculated age is younger than its actual emplacement age. However, it still lies within the age boundaries of the Kuunga Orogeny. Granite and granite gneiss samples DR1-3 and DR1-5 do not provide robust weighted mean averages, observed through the large rejection of grains, low probability of equivalence and high MSWD values, indicating that

isotopic disturbance has caused the observed spread in ages. Similarly, the more extensive spread of age data outside that expected for a single undisturbed population in granite and garnet granite gneiss samples DR1-4 (95 Myr) and DR1-38 (81 Myr) suggests processes were at play resulting in discernable isotopic disturbance. There are two likely mechanisms. Firstly, the significant isotopic disturbance combined with the homogenous $^{176/177}$Hf isotope signatures is consistent with lead loss. Furthermore, one discordant grain from DR1-5 with an unreliable age of 389 Ma has a $^{176/177}$Hf isotope ratio within 2sd of the mean for group 1 zircons, implying that the apparently younger, discordant grains that were not analysed are most likely from the same population, consistent with lead loss. The second possible mechanism is slow cooling from an open system pluton (Bomparola, *et al.,* 2007). This would enable the Lu-Hf isotope budget to remain constant for the duration of zircon crystallisation, consistent with a homogenous $^{176/177}$Hf isotope budget with decreasing age.

Such isotopic disturbance invalidates the use of a weighted mean average for age determination, seen through the unreliable weighted mean averages obtained for the samples with the least amount of spread (DR1-3, DR1-5, DR1-40). The oldest, concordant grain (<15%) from group 1 thus indicates a minimum age of crystallisation for individual samples (Halpin *et al,* 2012). The age of these granitoids and the mechanism/s for isotopic disturbance is poorly constrained, but still lies within the Kuunga Orogeny.

Accuracy/precision/validity of pinned intercepts for group 1 zircon

Pinned intercepts through group 1 zircons gave statistically reasonable MSWD using a discordance cut-off of less than 15% (Table 7.1). Intercepts pinned at 500, 400, 300, 132 and 0 Ma gave very similar MSWD's, indicating the probability of these scenarios are similar. As such, pinned intercepts are not reliable and do not provide valid information in these samples. Accordingly, the timing of lead loss cannot be determined by this method. However, two significant tectonothermal events could be possible triggers for the lead loss. These include the formation of Gondwanaland which ended ca. 500 Ma (Veevers, 2012), and the rifting of India and the western coast of Australia which occurred ca. 132 Ma and coincided with the presence of the Kerguelen Hotspot (Inlge *et al.,* 2002). Based on MSWD values from pinned intercepts, one, or both of these events could have caused the lead loss. However, due to the localised isotopic disturbance as documented in Chapter 7, it is most likely that lead loss occurred shortly after emplacement at ca. 500 Ma.

Group 2 zircon – inherited?

There are several reasons which, when combined, point to an inherited origin for group 2 zircons. Firstly, the distinctly igneous nature of all group 1 zircons implies the older grains are inherited. Secondly, the inability to calculate a statistically meaningful intercept through any group 2 zircon grains indicates the grains are likely sourced from a range of rocks. Thirdly, the $^{176/177}$Hf initial isotope signatures of the group 2 zircons scatter, consistent with zircons originating from a mixture of sources. Finally, the presence of fragmented zircon grain cores overgrown by group 1 zircon rims implies inheritance.

Inherited zircons can be incorporated into melts from a variety of sources. The most common sources involve either accidental contamination from wall-rock during emplacement or, at a deeper level, mixing of crustal sources and assimilation causes contamination (Miller *et al.*, 2003). It is possible that inherited zircons in the Batavia Knoll samples are derived from one or both of these sources due to the poorly constrained location of Batavia Knoll dredge samples and the presence of Archean to Proterozoic source rocks in the Kuunga Orogeny. This is consistent with the rocks being derived from similar sources.

Similar source for group 1 zircon – similar suite?

Suites are typically defined by geochemical analysis, however due to the highly altered state of these granitoids, this method is not valid. The similar initial $^{176/177}$Hf initial isotope ratios for group 1 zircons combined with the similarity in U-Pb isotope ages indicate that these granitoids could have originated from the same suite. Furthermore, these rocks were dredged along a 1km transect, evincing spatial correlation. The fit of the average continental crust model line through the averages of group 1 and 2 zircons further indicates that these rocks could be from the same plutonic suite (Fig. 7.12f).

Projection back to the Depleted Mantle model line

The high age discordance of 3 out of 4 analyses from granite DR1-4 facilitates the projection of these analyses back to the DM model line (Fig. 7.12d). This projection places the younger group 2 DR1-4 samples within the same age range as the concordant (<15%) grains from DR1-4, DR1-5 and DR1-38. This shows that DR1-4 has the same degree of scattering as the other two samples (DR1-5 and DR1-38) for $^{176/177}$Hf isotopes. One analysis from both DR1-5 and DR1-38 was also projected back to the DM line, placing these analyses within the age and scattering range. The

similar scatter indicates that these samples were derived from a similar source. This scatter is also consistent with the S-type characterisation of these granitoids.

Coincidence of group 1 and 2 zircons

The averages for group 1 and 2 zircons fit well on the 0.015 $^{176}Lu/^{177}Hf$ ratio average continental crust model line (Fig. 7.12f). This fitting line indicates that the group 1 zircons are derived from magma that reworked older crust, which was initially derived from the mantle between ca. 2.8 – 3.92 Ga. This is consistent with a plot of EHf vs. Age which shows the younger grains with a more negative signal (indicating reworked source) than the inherited grains which have a more positive signal, indicating a more juvenile source. This data combined with the scattered $^{176/177}Hf$ isotope ratio of group 2 zircons suggests that these granitoids have either i) recycled old Archean crust in one phase with a $^{176/177}Hf$ isotope budget indicating mantle derivation at ca. 2.8 – 3.92 Ga, or ii) recycled crust in multiple phases that has retained a $^{176/177}Hf$ isotope budget of mantle derivation at ca. 2.8 – 3.92 Ga. This is again consistent with the rocks being derived from similar sources.

Correlation to past studies

The decoupling of U-Pb and Lu-Hf isotope data in this study is consistent with studies by Halpin *et al.,* 2012; Bomparola *et al.,* 2007; Kinny *et al.,* 1991; Kinny & Maas 2003; Patchett 1983, Gerdes & Zeh 2009; and Halpin *et al*., 2005. These studies show that while U-Pb isotopes in zircon can be altered during tectonothermal events, the Lu-Hf isotopes remain unchanged, as has been found in this study.

Relative ages of granitoids

Evidence for age relationship between samples is seen through U-Pb dating and metamorphic grade, as the comparative ages of the granitoid samples can be inferred. The minimum emplacement ages determined by U-Pb isotope data for the rock samples are very similar, at ca. 550 Ma. However, the metamorphic grade between samples differs. Garnet granite gneiss and intermediate gneiss samples exhibit the highest metamorphic grades of granulite and amphibolite, respectively. Granite and granite gneiss samples exhibit lower metamorphic grades due to the retainment of rectangular, igneous crystals and a lack of high metamorphic grade minerals. Due to the distinctly higher vs. lower metamorphic grades seen in these rocks, it is inferred that the former group: garnet granite gneisses and intermediate gneiss are older by a few tens of millions of years than the latter group of granite and granite gneisses.

Correlation of Batavia Knoll with Kuunga Orogeny

This study examined foliated and non-foliated granitoids from Batavia Knoll that record 600-500 Ma orogenesis. This, alongside current place tectonic reconstructions enables the correlation of Batavia Knoll with the Kuunga Orogeny. The orogeny in Africa (Kalahari and Congo collision) is well documented, showing orogenesis from ca. 590 – ca. 520 (Fig. 1.7 histogram of rocks affected by the Kuunga Orogeny in Africa). This 50-100 Myr orogenesis is also seen in the eastern Kuunga Ororgeny zone (Aus/Maw and India collision), albeit with less exposure. This indicates that the timing of the eastern Kuunga orogeny was coeval with that of the western Kuunga ororgeny. Batavia Knoll granitoids add to the poorly exposed eastern Kuunga orogeny, further advocating one prolonged collisional event for the final Ediacaran – Cambrian Southern Gondwana assembly.

Chapter 9 - Conclusion

This study is the first to sample Batavia Knoll, and has determined a continental crust affinity. Based on two dredges, the knoll is considered to consist predominantly of granites (n=27), schist (n=3), granite gneisses (n=6), intermediate gneisses (n=9) and sandstones (n=10). The granites, schists, granite gneisses and intermediate gneisses were the focus of this study; seven representative samples were chosen for detailed analysis.

The majority (n=6) of the seven studied granitoids have been zircon U-Pb dated as latest Neo-Proterozoic to Cambrian in age. The intermediate gneiss yielded no zircons and is thus difficult to interpret relative to the granitoids. All six samples show evidence for significant tectonothermal disturbance, seen through lead loss in zircon and age spread along the concordia. This event is also evidenced through the metamorphic grade of samples; granulite, amphibolite and low metamorphic grades.

All seven samples have a shared history of alteration, demonstrated through chloritisation of biotite, sericite alteration of feldspar and low total alkali's in bulk rock chemistry.

The six U-Pb zircon dated samples from this study record orogenesis within 600-500 Ma. This combined with their continental crust affinity and current plate tectonic reconstructions of Gondwana (Gibbons *et al.,* 2006) has established the correlation of Batavia Knoll with the Kuunga Orogeny.

Chapter 10 - Future Research Avenues

- SHRIMP dating of zircon rims on DR1-41 to determine if igneous crystallisation occurred ca. 550 Ma
- Monazite dating of all samples to constrain metamorphic history
- P-T estimates of garnet granite gneisses to constrain metamorphic history
- Detailed study of sandstones including detrital zircon geochronology and examination of fossils

Reference List

Anderson, T., 2002. Correction of common lead in U–Pb analyses that do not report 204Pb. *Chemical Geology*, **192**: 59–79.

Black, L.P. & Gulson, B.L. 1978. The age of the Mud Tank carbonatite, Strangways Range, Northern Territory. *BMR Journal of Australian Geology and Geophysics.* **3**: 227–232.

Blichert-Toft, J., Chauvel, C. & Albarede, F. 1997. Separation of Hf and Lu for high-precision isotope analysis of rock samples by magnetic sector multiple collector ICP-MS. *Contributions to Mineral Petrology.* **127**: 248-260.

Boger, S.D., Maas, R. & Fanning, C.M. 2008. Isotopicand geochemical constraints on the age and origin of granitoids from the central Mawson Escarpment, southern Prince Charles Mountains, East Antarctica. *Contributions to Mineral Petrology* **155**: 379-400.

Bomparola, R.M., Ghezzo, C., Belousova, E., Griffin, W.L. & O'Reilly, S.Y. 2007. Resetting of the U-Pb Zircon System in Camro-Ordovician Intrusives of the Deep Freeze Range, Northern Victoria Land, Antarctica. *Journal of Petrology,* **48(**2): 327-364.

Cawood, P.A. & Korsch, R.J. 2008. Assembling Australia: Proterozoic building of a continent. *Precambrian Research*. **166**: 1-38.

Collins, A.S. 2003. Structure and age of the northern Leeuwin Complex, Western Australia: constraints from field mapping and U-Pb isotopic analysis. *Australian Journal of Earth Sciences.* **50:** 585-599.

Collins, A.S. & Pisarevsky, A.S. 2005. Amalgamating eastern Gondwana: The evolution of the Circum-Indian Orogens. *Earth-Science Reviews,* **71:** 229-270.

Cox , K.G., Bell, J.D. & Pankhurst, R.J. 1979. *The interpretation of Igneous Rocks*. London: Allen & Unwin.

Danis, C.R., Daczko, N.R., Lackie, M.A. & Craven, S.J. 2010. Retrograde metamorphism of the Wongwibinda Complex, New England Fold Belt and the implications of 2.5D subsurface geophysical structure for the metamorphic history. *Australian Journal of Earth Sciences.* **57**: 357-375.

Deer, W. A. (William Alexander) & Howie, R. A. (Robert Andrew) & Zussman, J. 1997, Rock-forming minerals, 2nd ed, Geological Society, London.

Gerdes, A. & Zeh, A. 2009, Zircon formation versus zircon alteration— new insights from combined U-Pb and Lu-Hf in situ LA-ICP-MS analyses, and consequences for the interpretation of Archean zircon from the Central Zone of the Limpopo Belt. *Chemical Geology,* **261(**3–4):230–243

Gibbons, A., Barckhausen, U., van den Bogaard, P., Hoernle, K., Werner, R., Whittaker, J.M. & Muller, D.R. (2006), 'Constraining the Jurassic extent of Greater India: tectonic evolution of the West Australian margin', pers. comm. Simon Williams, 2012.

Grew, E.S., Carson, C.J., Christy, A.G., Maas, R., Yaxley, G.M, Boger, S.D. & Fannings, C.M. 2012. New constraints from U-Pb, Lu-Hf and Sm-Nd isotopic data on the timing of sedimentation and felsic magmatism in the Larsemann Hills, Prydz Bay, East Antarctica. *Precambrian Research,* **206-207:** 87-108.

Griffin, W.L., Belousova, E.A., Shee, S.r>, Pearson, N.J. & O'Reilly, S.Y. 2004. Archean crystal evolution in the northern Yilgarn Craton: U-Pb and Hf-isotope evidence from detrital zircons. *Precambrian Research,* **131:** 231-282.

Griffin, W.L., Pearson, N.J., Belousova, E., Jackson, S.E., van Achterbergh, E., O'Reilly, S.Y. & Shee, S.R. 2000. The Hf isotope composition of cratonic mantle"LAM-MC-ICPMS analysis of zircon megacrysts in kimberlites. *Geochmimica et Cosmochimica Acta,* **64**(1): 133-147.

Griffin, W.L., Pearson, N.J., Belousova, E.A. & Saeed, A. 2007. Reply to "Comment to short-communication 'comment: Hf-isotope heterogeneity in zircon 91500' by W.L. Griffin, N.J. Pearson, E.A. Belousova & A. Saeed (Cheical Gwology 233 (2006) 358-363)" by F. Corfu. *Chemical Geology*. **244**: 354-356.

Halpin, J.A., Crawford, A.J., Direen, N.G., Coffin, M.F. , Forbes, C.J. & Borissova, I. 2008. Naturaliste Plateau, offshore Western Australia: A submarine window into gondwana assembly and breakup. *Geological Society of America.* **36**(10): 807-810.

Halpin, J.A., Daczko, N.R., Milan, L.A. & Clarke, G.L. 2012. Decoding near-concordant U-Pb zircon ages spanning several hundred million years: recrystallization, metamictisation or diffusion?. *Contributions Mineral Petrology.* **163**: 67-85.

Halpin, J.A., Gerakiteys, C., Clarke, G.L., Belousova, E.A. & Griffin, W.L. 2005. In situ U-Pb geochronology and Hf isotope analyses of the Rayner Complex, east Antarctica. *Contributions to Mineral Petrology*, **148**:689–706.

Hollocher, K n.d., Geology Department Union Colledge Schenectady, NY, U.S.A., viewed 27 April 2012, <http://minerva.union.edu/hollochk/c_petrology/norms.htm>

Hwang, S. L., Shen, P., Yui, T. F. and Chu, H. T. 2003. On the mechanism of resorption zoning in metamorphic garnet. *Journal of Metamorphic Geology*. **21**: 761–769.

Ingle, S., Weis, D., Scoates, J.S. & Frey, F.A. 2002. Relationship between the early Kerguelen plume and continental flood basalts of the paleo-Eastern Gondwanan margins. *Earth and Planetary Science Letter.* **197**: 35-50.

Janssen, D.P., Collins, A.S. & Fitzimons, I.C.W. (2003), 'Structure and tectonics of the Leeuwin complex and Darling Fault zone, Southern Pinjarra Orogen Western Australia – a field guide', *Geological Survey of Western Australia.* From: Geological society of Australia Specialist group in tectonics and structural geology 12th field guide. Record 2003/15.

Kinny, P.D., Compston, W. & Williams, I.S. 1991. A reconnaissance ionprobe study of hafnium isotopes in zircons. *Geochim osmochim Acta* **55**:849–859

Kinny, P.D. & Maas, R. 2003. Lu-Hf and Sm-Nd isotope systems in zircon. *Rev Mineral Geochem,* **53**:327–341.

Ksienzyk, A.K., Jacobs, J., Boger, S.D., Kosler, J., Sircombe, K.N. & Whitehouse, M.J. 2012. U-Pb ages of metamorphic monazite and detrital zircon from the Northampton Complex: evidence of two orogenic cycles in Western Australia. *Precambrian Research,* **198-199**: 37-50.

Leake, B.E., Woolley, A.R., Birch, W.D., Burke, A.J., Ferraris, G., Grice, J.D., Hawthorne, F.C., Kisch, H.J., Krivovichev, V.G., Schumacher, J.C., Stephenson, N.C.N. & Whittaker, E.J.W. 2004. Nonenclature of amphiboles: additions and revisions to the International Mineralogical Association's amphibole nomenclature. *The Mineralogical Society.* **68**: 209-215.

Meert, J.G., van der Voo, R. & Ayub, S. 1995. Paleomagnetic investigation of the Neoproterozoic Gagwe lavas and Mbozi complex, Tanzania and the assembly of Gondwana. *Precambrian Research,* **74:** 225-244.

Meert, J.G. 2003. A synopsis of events related to the assembly of eastern Gondwana. *Tectonophysics.* **36:** 1-40.

Middlemost, E.A.K. 1994. Naming materials in the magma/igneous rock system. *Earth-Science Reviews,* **37**(3-4): 215-224.

Miller, C.F., Mc Dowell, S.M. & Mapes, R.W. 2003. Hot and cold granites? Implications of zircon saturation temperatures and preservation of inheritance. *Geological society of America,* **31**(6): 529-532.

Morimoto, N., Fabries, J., Ferguson, A.K., Ginzburg, I.V., Ross, M., Seifert, F.A., Zussman, J., Aoki, K. & Gottardi, G. 1988. Nomenclature of pyroxenes. *American Mineralogist,* **73:** 1123-1133.

Nicolaysen, K., Bowring, S., Frey, F., Weis, D., Ingle, S., Pringle, M.S. & Coffin, M.F. 2001. Provenance of Proterozoic garnet-biotite gneiss recovered from Elan Bank, Kerguelen Plateau, southern Indian Ocean. *Geological Society of America.* **29**(3): 235-238.

Patchett, P.J. 1983. Importance of the Lu-Hf isotopic system in studies of planetary chronology and chemical evolution. *Geochim Cosmochim Acta* **47**(1):81–91.

Pearce J.A., Harris, N.B.W. & Tindle, A.G. 1984. Trace Element Discrimination Diagrams for the Tectonic Interpretation of Granitic Rocks. *Journal of Petrology*, **25**(4): 956-983.

Rollinson, H.R. 1993. Using Geochemical Data: Evaluation, Presentation, Interpretation. Harlow, Pearson Education Limited.

Spear, F.S. 1993. *Metamorphic Phase Equilibria and Pressure-Temperature-Time Paths*, Mineralogical Society of America, Washington, D. C.

Veevers, J.J., Belousova, E.A., Saeed, A., Sircombe, K., Cooper, A.F & Read, S.E. 2006. Pan-Gondwananland detrital zircons from Australia analysed for Hf-isotopes and trace elements reflect an ice-covered Antarctic provenance of 700-500 Ma age, T_{DM} of 2.1-1.0 Ga, and alkaline affinity. *Earth-Science Reviews.* **7**: 135-174.

Veevers, J.J. & Saeed, A. 2011. Age and composition of Antarctic bedrock reflected by detrital zircons, erratics, and recycled microfossils in the Prydz Bay-Wilked Land- Ross Sea- Marie Byrd Land sector (70°-240°E). *Gondwana Research,* **20**:710-738.

Veevers, J.J. 2012. Reconstructions before rifting and drifting reveal the geological connections between Antarctica and its conjugates in Gondwanaland. *Earth-Science Reviews.* **111**: 249-318.

Weis, D., Ingle, S., Damasceno, D., Frey, F., Nicolaysen, K. & Barling, J. 2001. Origin of continental components in Indian Ocean basalts: Evidence from Elan Bank (Kerguelen Plateau, ODP Leg 183, Site 1137). *Geological Society of America.* **29(**2): 147-150.

Wiedenbeck, M., Alle, P., Corfu, F. et al., 1995. Three natural zircon standards for U–Th–Pb, Lu–Hf, trace element and REE analyses. *Geostandards Newsletter*. **19**: 1–23.

Woodhead, J.D. & Hergt, J.M. 2005. A Preliminary Appraisal of Seven Natural Zircon Referene Materials for *In Situ* Isotope Determination. *Geostandards and Geoanalytical Research,* **29**(2): 183-195.

Zhu, D.C., Chung, S.L., Mo, X.X., Zhao, Z.D., Niu, Y., Song, B. & Yang, Y.H. 2009. The 132 Ma Comei-Bunbury large igeous province: Remnants identified in present-day southeastern Tibet and southwestern Australia. *Geological Society of America.* **37**(7): 583-586.